UNIVERSIDAD EUROPEA DE MADRID

ESCUELA DE ARQUITECTURA, INGENIERÍA Y DISEÑO

DEGREE IN AEROSPACE ENGINEERING

FINAL YEAR PROJECT REPORT

AUTONOMOUS VTOL TAIL-SITTER FOR PRECISION CROP HEALTH MONITORING

MANUEL MARTÍNEZ LLUÍS

YEAR 2023/2024

TITLE: AUTONOMOUS VTOL TAIL-SITTER FOR PRECISION CROP HEALTH MONITORING

AUTHOR: MANUEL MARTÍNEZ LLUÍS

SUPERVISORS: VÍCTOR MANUEL PADRÓN NÁPOLES & JOSE OMAR MARTÍNEZ LUCCI

DEGREE: AEROSPACE ENGINEERING

DATE: 07/07/2024

ABSTRACT

Precision agriculture is undergoing a transformative shift towards maximizing crop yield while minimizing resource consumption. Traditional methods of crop monitoring often lack accuracy and are labour-intensive. The integration of UAVs equipped with multispectral cameras has revolutionized this field, offering a non-invasive, efficient means of surveying agricultural landscapes to perceive detailed plant health information.

The primary objective is to create a drone capable of autonomously executing flight missions from take-off to landing, with minimum interventions required from the operator. By harnessing the power of multispectral imagery, the drone facilitates precise monitoring of crop health parameters, enabling farmers to make informed decisions regarding irrigation, fertilization, and pest control strategies.

Methodologically, the project follows a systematic approach encompassing design, 3D printing, integration of electronics, and development of an autonomous flight system. Results demonstrate the successful creation of an autonomous VTOL tail-sitter drone capable of efficiently capturing multispectral data.

In conclusion, this project contributes to the advancement of precision agriculture by offering a robust and efficient tool for crop monitoring and management. The fully autonomous capabilities of the drone, coupled with its ability to provide actionable insights through multispectral imagery, hold great promise for enhancing agricultural productivity and sustainability.

Key words: Precision agriculture, 3D printing, Autonomous UAV, VTOL Tail-sitter, Multispectral imaging.

ACKNOWLEDGEMENTS

I extend my deepest appreciation to my supervisors Dr. Omar and Dr. Victor, for their expert guidance and solid support throughout this project. Dr. Omar's expertise in aerodynamics and drone design, coupled with Dr. Victor's proficiency in electronics and autonomous systems, has been pivotal in the successful development of the drone. Their mentorship and encouragement have been invaluable assets in navigating the complexities of this research.

Additionally, I am grateful to my parents for their constant encouragement and belief in my abilities. Their unwavering support has been a driving force behind my academic journey. Without the collaborative efforts of all involved, this achievement would not have been possible.

Content

Table of figures

Table of tables

Chapter 1. Introduction

The escalating global population, projected by the United Nations (UN) to reach 8.5 billion by 2030 and 9.7 billion by 2050, poses unique challenges for food production [1]. According to the Food and Agriculture Organization (FAO), this population rise requires a 70% increase in global agricultural output by 2050 [2]. However, meeting this demand must occur within the constraints of existing arable land, making efficient resource management vital.

Despite its status as an economic engine, agriculture struggles with complex challenges, including the decline of natural resources, intensified by factors such as salinization, water contamination, and climate change. Agriculture consumes 70% of the world's freshwater resources, demanding a shift towards more sustainable water management practices [3]. Furthermore, the sector faces demographic challenges, with an aging agricultural workforce and an absence of younger farmers due to rural-to-urban migration, potentially leading to the abandonment of farmland.

Conventional agricultural practices often overlook the inherent irregularity within fields, leading to inefficiencies in resource allocation and productivity. The advantage of precision agriculture, using technologies like remote sensing, offers a transformative solution. By enabling precise monitoring and management of agricultural resources, remote sensing holds the promise of optimizing productivity while minimizing environmental impact. However, widespread adoption of these technologies remains a challenge, underscoring the importance of accessibility and capacity-building initiatives.

Against this backdrop, this project seeks to address the vital need for innovative solutions in agriculture by developing a fully autonomous VTOL tail-sitter UAV equipped with multispectral imaging capabilities. This drone aims to revolutionize crop monitoring and management by providing farmers with actionable insights taken from high-resolution data. By employing advanced manufacturing techniques and autonomous flight capabilities, this project endeavours to contribute to the advancement of precision agriculture, paving the way towards a more sustainable and robust food system.

Chapter 2. Objectives

On the one hand, one of the objectives is to raise awareness of these new technologies, such as remote sensing, and new practices of precision agriculture in the agricultural, educational, and social environments.

On the other hand, the aim is to engage youth in agriculture. Given that young society tend to migrate to large cities, it is envisioned to highlight that agriculture can encompass and integrate diverse fields such as aerospace technologies, engineering, physics, cartography, computer science, and environmental studies. In essence, agriculture is also technology.

The objective of the study is to design and built a VTOL UAV, analyse it through FEA and CFD, integrate multispectral imaging capabilities and develop an autonomous flight control system.

The formulated hypothesis argues that with an UAV equipped with a multispectral camera, more than sufficient information can be obtained to optimize agricultural production, reduce water consumption, and detect plant diseases, drought, or other issues.

Chapter 3. UAVs in agriculture

In the precision agriculture sector, two major types of UAVs are employed: fixed-wing and multirotor, each offering distinct benefits for precision farming and crop monitoring.

- **Fixed-wing UAVs:**

Figure 1: Flying wing, a variant of the fixed-wing design [4].

Fixed-wing UAVs, characterized by their rigid, unchanging wing structure during flight, are highly valued in agriculture. They shine in surveying and monitoring expansive agricultural landscapes, effectively mapping large areas.

While their design allows for covering large areas rapidly by flying in straight lines, fixed-wing drones cannot hover, limiting their effectiveness in detailed crop inspections or collecting specific data within tight spaces. Additionally, they require space for landing, which can be a challenge due to the irregularities of the ground.

Operating fixed-wing UAVs requires specialized skills and considerable experience because of their intricate flight controls and the need for ongoing manual adjustments. Unlike multirotors, which can hover and maintain stability with minimal effort, fixed-wing UAVs necessitate constant joystick input to sustain a balanced flight. As a result, it is often recommended to use expert operators for crop mapping tasks with these drones.

Despite these limitations, fixed-wing drones are notably efficient for inspecting vast plantation areas, such as oil palm and olive groves plantations, offering extended flight times and stability in the air.

- **Multi-rotor UAVs:**

Figure 2: Hexarotor UAV for mapping.

Known commonly as multi-copters, multi-rotor drones feature several rotors (usually four) and are frequently used in agriculture for tasks like fertilizing, seeding, pest and disease detection.

These aerial vehicles are more apt for targeted applications such as spraying rather than large-scale mapping due to their lower efficiency and limited range. Also, the operational noise of these drones can be problematic, particularly around livestock, as it may cause stress and disturbance.

However, the ease of learning to operate them compared to fixed-wing drones is a significant advantage. Moreover, these versatile aircraft can effortlessly accommodate various payloads, including liquid pesticides and granular seeds, without compromising their structural integrity or flight capabilities.

- **VTOL – (Subtype of fixed-wing UAV):**

Seeing the Achilles' heel of each design, the VTOL (Vertical Take-Off and Landing) aircraft concept emerges as the optimal solution. It combines the vertical take-off and landing capabilities of multi-rotors with the efficient long-distance flight characteristics of fixed-wing aircraft. VTOL design eliminates the need for a runway, enabling safe landings in diverse field conditions while maintaining excellent range. Additionally, VTOLs provide longer flight times and higher cruising speeds than multi-rotors, enhancing efficiency in field mapping.

Figure 3: Hybrid VTOL, a variant of the fixed-wing design [5].

3.1. VTOL classification

VTOL aircraft encompass various configurations, each tailored to specific operational requirements. Among these configurations, the tail-sitter type stands out for its unique ability to vertically orient itself during take-off and landing relying on only two motors situated in each wing and a vertical stabilizer for directional stability.

Contrarywise, other VTOL designs opt for a quadcopter configuration (Figure 3), featuring four motors positioned vertically and one horizontally to facilitate both vertical and horizontal flight. Additionally, other aircraft use a mechanism to tilt the rotors 90º allowing them to transition between vertical and horizontal flight modes. While this design offers enhanced versatility, it also introduces complexity due to the presence of multiple moving parts.

To minimize weight and mechanical complexity, the tail-sitter configuration emerges as the optimal choice for the agricultural field mapping mission. With its two motors, this configuration provides sufficient power for vertical hovering and horizontal flight, maximizing efficiency. In contrast to other VTOL configurations, the tail-sitter design eliminates the need for additional motors which will be useless in horizontal flight.

Additionally, it eliminates the necessity for complex mechanisms to orient the motors in the desired direction, enhancing overall reliability and ease of use.

3.2. Components of a VTOL tail-sitter

3.2.1. Frame

The frame serves as the structural foundation, housing all other components and defining the UAV's size and characteristics, while also influencing factors such as flight agility, stability, and payload capacity.

Figure 4: Various carbon fibre quadcopter frames [6].

UAV frames can be made from a variety of materials, each offering distinct advantages and considerations. Common materials include carbon fibre, aluminium alloys, and thermoplastics like PLA. Carbon fibre is valued for its high strength-to-weight ratio, making it ideal for lightweight yet durable frames. Aluminium alloys offer a balance of strength and affordability, providing robustness while remaining relatively lightweight. Thermoplastics are popular for their ease of manufacturing and versatility, allowing for complex shapes and designs while being cost-effective.

3.2.2. FC (Flight controller)

The flight controller board acts as the central computing unit, collecting data from various sensors including the gyroscope, accelerometer, barometer, compass, GPS, etc. Then, these inputs are processed and transmitted to the corresponding outputs such as control surfaces or power systems. Additionally, modern flight controllers often feature advanced capabilities such as autonomous flight modes, waypoint navigation, and obstacle avoidance.

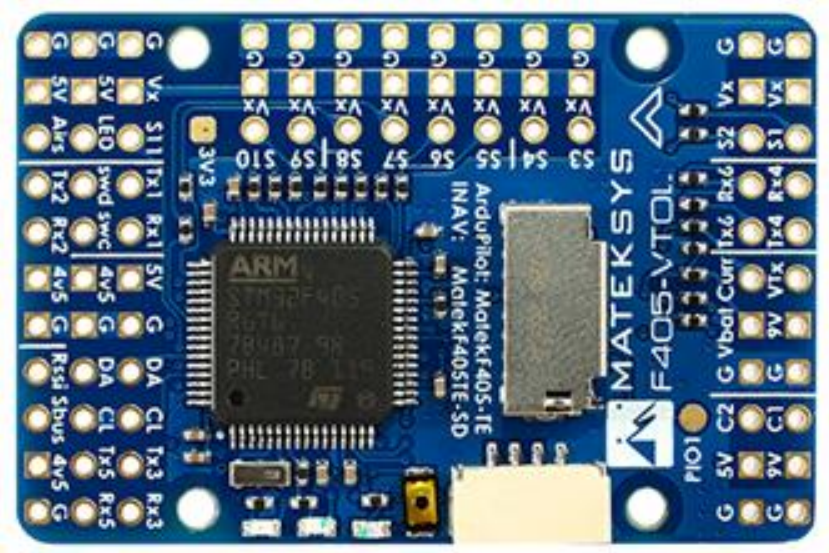

Figure 5: Mateksys F405 VTOL flight controller [7].

The central component of every FC is the microcontroller (MCU), which enables efficient execution of control algorithms and management of sensor data. Equipped with a wide range of peripherals including timers, communication interfaces, and analog-to-digital converters, MCU chips facilitate uniform integration with sensors and actuators essential for drone operation.

Flight controllers often utilize STM32 microcontrollers with F4 and F7 chips, distinguished by their processing power and features. The F4 chips offer a balance between performance and cost, making them the most popular choice. Meanwhile, the F7 chips provide greater computational capabilities, supporting more complex algorithms and precise control. With advanced peripherals and higher clock speeds, F7 chips are particularly suited for demanding applications requiring fast response times and intricate control algorithms [8].

3.2.3. Brushless motors

A brushless motor (BLDC) comprises two primary components: a stator and a rotor. In a typical setup, the rotor features a set of permanent magnets with two poles, while the stator consists of coils arranged as showed in Figure 6 (Left). Brushless motors can come in different diameters and heights, allowing for various torque and speed characteristics. Additionally, they can have varying numbers of magnet pairs, which influence the motor's performance and efficiency. This versatility in design enables brushless motors to be tailored to specific applications and requirements.

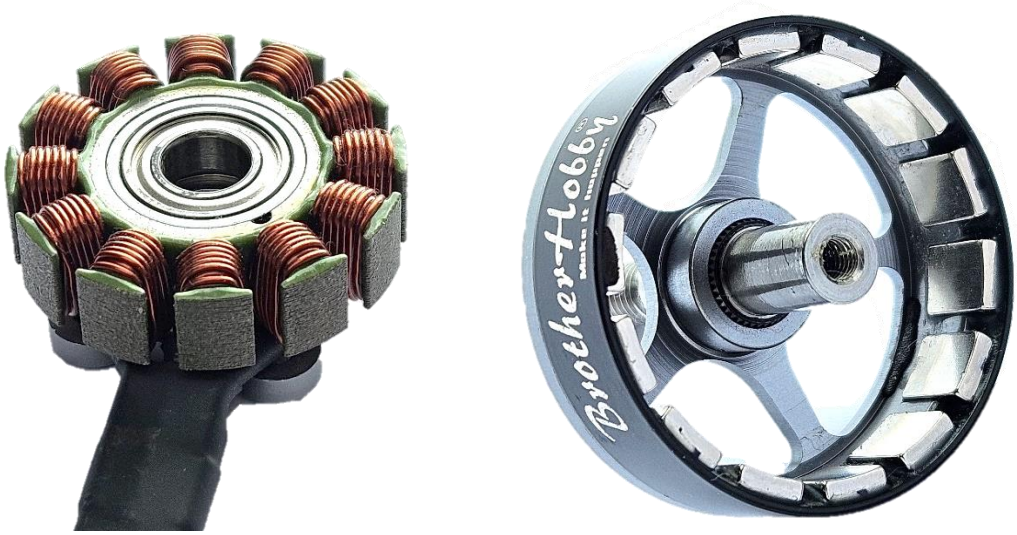

Figure 6: Dissembled brushless motor; Stator (Left); Rotor (Right).

When current flows through a coil, it generates a magnetic field, and the direction of the magnetic field lines or poles depends on the current's direction [9]. By applying the appropriate current, the coil produces a magnetic field that attracts the rotor's permanent magnets. Sequentially activating each coil causes the rotor to rotate due to the interaction between the magnets and the electromagnet.

3.2.4. ESC (Electronic Speed Controller)

The ESC controls the movement or speed of brushless motors by activating the proper MOSFETs to initiate the motor rotation. The motor's speed is directly influenced by the frequency at which the ESC cycles through the different intervals, with higher frequencies resulting in increased motor speed.

Figure 7: HOBBYWING Skywalker 40Amps V2-UBEC ESC.

The proper choice of an ESC depends on the motor selected. The most critical parameter for an ESC is its maximum amperage rating, which dictates the amount of current it can handle. This selection process involves considering the propeller size and the motor's maximum current consumption in amperes, usually provided by the motor manufacturer.

3.2.5. Propellers

Propellers are essential components that efficiently convert the rotational energy produced by the motors into forward thrust, enabling the aircraft to move through the air. To maximize energy efficiency, two-bladed propellers are typically used. Research indicates that two-bladed propellers consume less energy compared to their three-bladed counterparts, making them the preferred choice for endurance missions. This reduced energy consumption translates into longer flight times and improved overall performance, particularly crucial for extended operations [10].

Figure 8:Pair of 8 x 6 propellers.

Within the realm of two-bladed propellers, various sizes and pitching angles are available, each influencing the drone's performance characteristics. The numbers associated with propellers, such as in Figure 8, denote their dimensions and pitch. In this example, "8" represents the diameter of the propeller in inches, while "6" indicates the pitch, which is the distance the propeller would move forward in one full rotation if it was moving through a solid medium.

A higher pitch number typically indicates a steeper angle of attack, resulting in greater forward thrust but potentially requiring more power from the motor. Conversely, a lower pitch number implies a shallower angle, which may offer smoother operation and lower power consumption.

3.2.6. Battery

UAV batteries play a crucial role in powering UAVs, providing the necessary energy for propulsion and onboard electronics. The two main types of batteries used in UAVs are lithium polymer (Li-Po) and lithium-ion (Li-ion).

Figure 9: BRUTEPOWER 4s1p 3000 mAh Li-Po battery.

Li-Po batteries are known for their high energy density, making them lightweight and ideal for applications where weight is a critical factor, such as racing quadcopters. On the other hand, Li-ion batteries offer a longer lifespan and better stability but tend to be heavier and have a lower energy density compared to Li-Po batteries [11].

One of the key differences between Li-Po and Li-ion batteries lies in their internal chemistry and construction. Li-Po batteries typically use a polymer electrolyte, allowing for flexible packaging and higher discharge rates. Li-ion batteries, on the other hand, use a liquid electrolyte, and they are typically manufactured in cylindrical cells, similar to AA batteries [11].

Both Li-Po and Li-ion batteries consist of multiple cells connected in series or parallel to achieve the desired voltage and capacity. The nominal voltage of a single cell is typically around 3.7 volts for both Li-Po and Li-ion batteries. Therefore, a Li-Po battery with a nominal voltage of 14.8 volts, as in Figure 9, would consist of four cells connected in series (4s). In the other way, if two cells are connected in parallel, the capacity (mAh) doubles while the voltage remains the same.

3.2.7. Servos

A servo is a small motor system used for precise control of angular or linear position, velocity, and acceleration. It typically consists of a motor, a position potentiometer, and a microcontroller [12].

In UAVs, servos are the responsible for moving the control surfaces through metal rods or linkages, transmitting the desired movements generated by the flight controller. They typically have three connections: VCC, GND (ground), and signal (control input). The signal determines the position of the servo arm, which dictates the angle of the control surface.

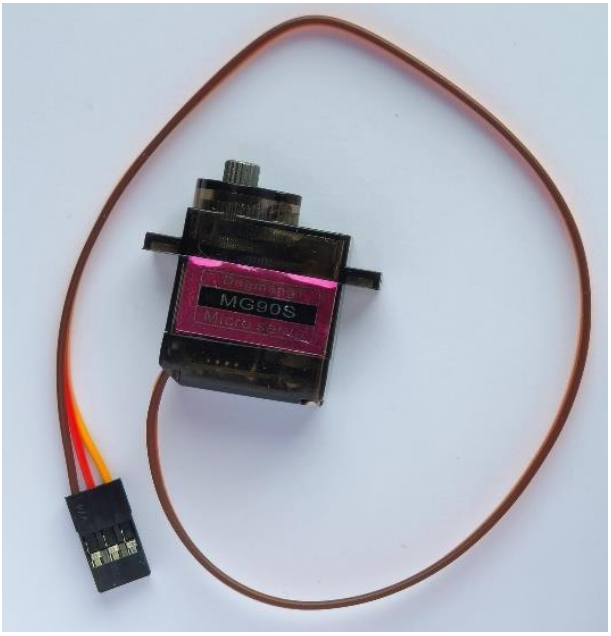

Figure 10: MG90s micro servo with metal gears.

Servos commonly come with either plastic or metallic gears. Metallic gears offer greater durability and resistance to wear, making them ideal for applications where reliability is crucial.

3.2.8. Transmitter and receiver

The receiver (RX) and transmitter (TX) are essential components of radio control systems used to remotely pilot UAVs. The TX, operated by the pilot, sends control signals wirelessly to the RX onboard the aircraft, where the FC interprets these signals and translates them into commands.

Transmitters typically resemble console controllers, featuring two joysticks, various buttons, and potentiometers. They are equipped with a sophisticated transmission system and an antenna that operate between 868 MHz and 915 MHz [13]. These signals are received by the receiver, which consists of an antenna and a microcontroller directly connected to the FC. This setup ensures precise control of the UAV's movements and functions, allowing operators to manoeuvre the vehicle with accuracy and responsiveness. Additionally, modern transmitters often include programmable settings, telemetry feedback, and ergonomic designs to enhance user experience and control efficiency.

Figure 11: (Left) FrSky X9D+ transmitter, (Right) TBS nano RX receiver.

3.2.9. GPS

A GPS system is an essential component for UAVs, enabling precise location and velocity tracking. Using signals from a network of satellites, the GPS system determines the UAV's exact position and movement. This functionality is crucial for executing waypoint missions, where the UAV follows predefined routes. In addition, a georeferenced system enables the Return-to-Home (RTH) function, which automatically guides the UAV back to the take-off point in case of an emergency or loss of connection.

Figure 12: Mateksys GNSS and compass M10-5883 GPS module [14].

3.2.10. Payload

The payload for UAVs varies depending on the mission requirements and capabilities. In precision agriculture, the payload typically includes multispectral or hyperspectral cameras that capture detailed information about plant health. These specialized cameras are equipped with different lenses that capture various wavelengths of the light spectrum, providing valuable data for assessing crop conditions.

Figure 13: Parrot Sequoia + multispectral sensor [15].

Chapter 4. VTOL design

The design process for the VTOL, as summarized in Figure 14, encompasses several methodical steps to ensure an efficient approach. The process begins with defining the mission requirements, which establish the primary objectives and constraints for the UAV's intended operation. Following this, a thorough analysis of similar systems is conducted to gather insights and benchmarks from existing platforms. An iterative weight estimation process then takes place, refining the weight predictions based on evolving design considerations.

Next, the focus shifts to the sizing and layout phase, where the overall dimensions and configuration of the UAV are determined. Critical design parameters are calculated to ensure all necessary factors are considered for optimal performance. The aerodynamic characteristics of the UAV are analysed to understand how it will behave in different flight conditions. Performance calculations follow, assessing the UAV's capabilities in terms of speed, endurance, and manoeuvrability.

Finally, a sizing matrix and optimization process is applied, which integrates all the gathered data and analysis to fine-tune the design. This step ensures that the UAV meets all mission requirements efficiently and effectively. This structured approach allows for a detailed and iterative development process, ultimately leading to a well-optimized VTOL UAV design.

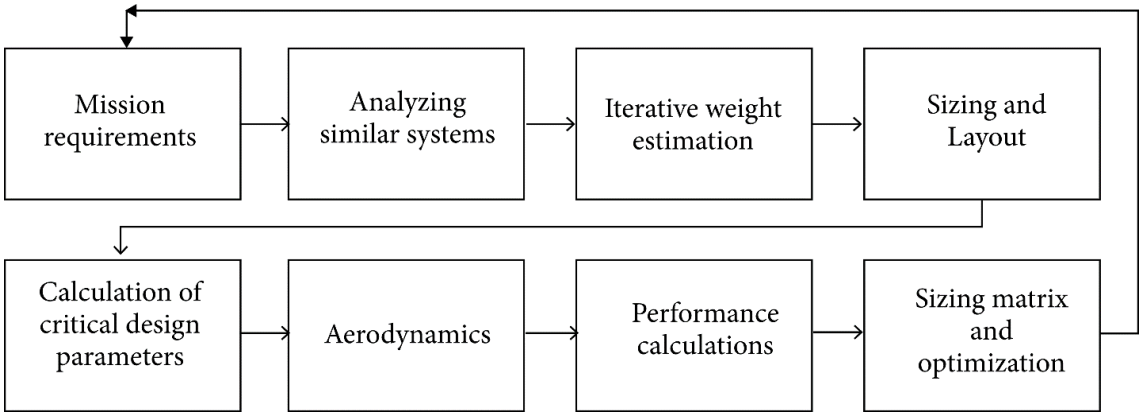

Figure 14: Summary of the UAV design process.

4.1. Mission requirements

The mission requirements for the UAV are pivotal as they define the objectives and constraints that will shape the entire design process. For this particular UAV, the primary mission is to conduct precision agriculture tasks, such as monitoring and surveying expansive agricultural landscapes. This requires a UAV that can achieve extended flight times and cover large areas efficiently. The UAV must be equipped with

high-resolution multispectral cameras to capture detailed images of plant health. Given the need for precision in detecting unhealthy areas, the UAV should maintain a resolution that allows for clear differentiation of plant features from the ground. Additionally, regulatory restrictions, such as the maximum allowable flight altitude must be adhered to.

Moreover, the UAV must be designed to operate at an optimal cruise speed, balancing the need for detailed image capture with efficient area coverage. A cruise speed range of 13-20 m/s is targeted to maximize efficiency and minimize flight time while maintaining image quality (more information in Chapter 4.3.). The UAV's design should also account for multiple battery options to extend flight duration if necessary, enabling operations at lower altitudes for better resolution without significantly affecting overall mission time. These requirements emphasize the importance of stability, low drag, and reliability in the UAV's design, ensuring it can perform effectively in the field and provide accurate, actionable data for agricultural management.

4.2. Weight estimation

The first and foremost step in designing a UAV is the weight estimation. Accurately predicting the weight of the drone before it is even designed is crucial for several reasons.

- Primarily, the weight of the UAV directly influences its performance, stability, and endurance. An accurate estimation helps in determining the appropriate propulsion system, battery size, and structural integrity required to meet mission objectives.

- Secondly, understanding the weight constraints early in the design process allows for more accurate decisions regarding material selection, aerodynamic design, and payload capacity, ensuring that the final design meets the operational requirements without unnecessary overdesign.

To predict the weight of the VTOL, similar UAVs in the sector are compared to obtain reference values. By examining the main properties of existing UAVs with comparable missions, a baseline can be established for the VTOL design. The table below lists reference aircraft, including their wingspan, length, maximum take-off weight (MTOW), empty weight, payload weight, battery weight, and cruise speed. These parameters serve as a foundation for estimating the mass of the new UAV, enabling a more accurate and efficient design process.

Reference aircraft / Specifications	Quantix Mapper [16]	Wingtra One [17]	Marlyn [18]
Wingspan	1.00 m	1.25 m	1.60 m
MTOW	2.3 Kg	4.50 Kg	6.70 Kg
Empty Weight (with battery)	~1.9 Kg	3.70 Kg	5.70 Kg
Payload Weight	~0.40 Kg	0.80 Kg	1.00 Kg
Battery Weight	~0.50 Kg	1.20 Kg (2 batt.)	1.34 Kg (2 batt.)
Cruise Speed	16.6 m/s	16 m/s	20 m/s

Table 1: Main specifications of similar VTOL aircrafts.

Since most of the components to be used for the VTOL are not subjected to changes during the design and manufacturing process due to their compatibility, their mass can be known. These components are the FC + PDB, RX + antenna, GPS, servos and, payload. The battery, motors, ESCs and propellers could change depending on the final parameters of the design, but an estimate could be obtained using common equipment used in aircrafts from Table 1.

Component name	Mass [grams]
Structure group	
Main body (3D printed)	~450.00
Wings (3D printed)	~680.00
Vertical tailplane (3D printed)	~150.00
Propulsion group	
Motors	~180.00
Propellers	~15.00
ESCs	~73.00
Electronic group	
FC + PDB	30.00
GPS	21.00
RTX + antenna	15.40
Servos + connection rods	30.00
Battery	~1,000.00
Payload group	
Multispectral camera	274.00
Approx. Total Mass	**~2,918.40**

Table 2: Mass estimation breakdown of VTOL components.

The estimated mass of the new VTOL is competitive when compared to Table 1 samples. The total mass is within a reasonable range, indicating that the design should be feasible and efficient. Additionally, the lower overall weight could potentially offer advantages in terms of manoeuvrability. However, further refinement and validation of these estimates are necessary to ensure the design meets all operational requirements and constraints.

4.3. Cruise speed determination

The cruise speed for the VTOL is subjected to its mission objective which is crop health monitoring through the Sequoia multispectral camera. This camera has 4 different monochrome sensors and one RGB. Monochrome and RGB lenses have different ground resolution depending on the altitude of flight. The following table can be extracted from the camera's manual [19].

	Ground resolution [cm/px]	
Altitude [m]	Monochrome	RGB
30	3.7	0.8
40	4.9	1.1
50	6.2	1.4
60	7.4	1.6
70	8.6	1.9
80	9.9	2.2
90	11.1	2.4
100	12.4	2.7
110	13.6	2.9
120	14.8	3.3

Table 3: Ground resolution of monochrome and RGB sensor depending on flight altitude [19].

The manufacturer specifies altitudes up to 150 m, but flights above 120 m are disregarded due to Spain's regulations. In Europe, the maximum height for UAV flights is restricted to 120 m for safety reasons. This limitation is based on the minimum operating altitude for helicopters, set at 150 m, ensuring a safety margin of 30 m [20].

As it can be seen in Table 4, the RGB resolution is much better since it is a 16 MP sensor, while the monochrome sensors are only 1.2 MP. Examining the resolutions suggests that lower flight altitudes yield better data quality. However, this also significantly increases flight time as the camera captures a smaller area per image.

Additionally, the sensor's capture rate is crucial for determining the cruise speed. The RGB sensor can capture one image per second, while the monochrome sensor one every 0.5 seconds. Since the primary objective is to monitor the health of the plantation, the

monochrome sensor is essential, allowing the RGB sensor to be turned off during missions.

Considering these factors, the manufacturer provides a table detailing different speeds and flight altitudes.

	Time between shots			
Height [m]	5 m/s	10 m/s	13 m/s	20 m/s
30	1.1	0.5	0.4	0.3
40	1.4	0.7	0.5	0.4
50	1.8	0.9	0.7	0.5
60	2.2	1.1	0.8	0.6
70	2.6	1.3	1.0	0.7
80	2.9	1.4	1.1	0.74
90	3.3	1.6	1.2	0.8
100	3.7	1.8	1.4	0.9
110	4.1	2.1	1.6	1.0
120	4.4	2.2	1.7	1.1

Table 4: Time intervals depending on flight speed and altitude [19].

In red: the monochrome and RGB sensors cannot be activated.

In blue: the RGB sensor cannot be activated.

In green: all the sensors can be activated.

As seen in Table 5, the UAV could operate in the blue range where the RGB sensor cannot be activated but the monochrome sensors can. Lower altitudes provide better resolution but require more time to map a terrain, whereas higher altitudes allow faster speeds, reducing the flight time.

To achieve fast mapping with maximum resolution, altitudes should range between 50 to 90 meters, with cruise speeds approximately between 13 to 20 m/s. To better understand the resolution at each altitude, some 3D parts are printed for each resolution. For instance, at 50 meters, the monochrome sensors resolution is 6.2 cm per pixel, meaning a 6.2 x 6.2 cm area on the terrain will correspond to one pixel in the final image.

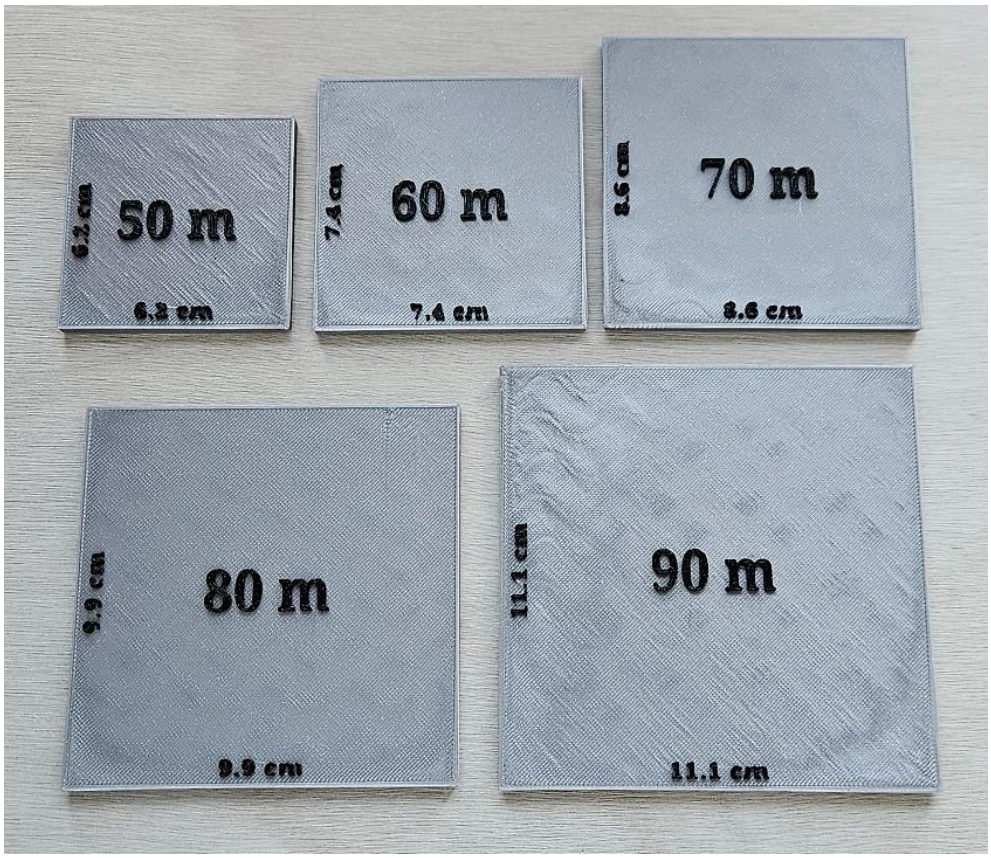

Figure 15: 3D printed squares representing resolution depending on flight altitude.

The impact of changing flight altitudes on data resolution is evident thanks to these 3D samples. Altitude selection directly correlates with the size of the terrain under study: higher altitudes reduce flight time for larger areas, while lower altitudes enhance resolution for smaller areas without significant time penalties. Optimal altitude choice hinges on mission-specific needs and available resources. For instance, the possession of multiple batteries would eliminate the time constraint, enabling lower altitudes for better resolution.

Flying at 30 or 40 meters is judged unnecessary as it yields nearly identical results to 50 meters, yet increases the number of images exponentially, leading to prolonged processing and flight durations. Conversely, flying too high reduces resolution, potentially obscuring details crucial for identifying unhealthy areas. Resolutions exceeding 12x12 cm per pixel begin to incorporate ground features alongside vegetation. For instance, at 120 meters altitude, a plant measuring 9 x 9 cm would correspond to a pixel resolution of 14.8 x 14.8 cm, with around 63% ground data per pixel, potentially corrupting plant health indicators.

To get consistent results, overlapping is used in every field where mapping is involved. Overlapping ensures complete coverage, as there could be blurry images due to a wind gust or excessive control input from the FC. Additionally, overlapping images provide common reference points that are essential for accurately “stitching” images together into a unified mosaic. This process, known as image mosaicking, relies on having multiple images with shared features to align and merge them correctly [21].

	Distance between shots [m]			
Height [m]	70%	75%	80%	85%
30	8.4	7.0	5.6	4.2
40	11.2	9.3	7.5	5.6
50	14.0	11.7	9.3	7.0
60	16.8	14.0	11.2	8.4
70	19.6	16.4	13.1	9.8
80	22.4	18.7	15.0	11.2
90	25.2	21.0	16.8	12.6
100	28.0	23.4	18.7	14.0
110	30.8	25.7	20.6	15.4
120	33.7	28.0	22.4	16.8

Table 5: Distance between shots depending on altitude and % of overlapping.

In Table 7, it is evident that the distance between camera shots varies based on the percentage of overlap and flight altitude. As the overlap between images increases, the camera must take pictures more frequently, reducing the distance between shots.

For example, consider a flight velocity of 16 m/s with an 85% overlap at a 50-meter altitude. Under these conditions, the Sequoia camera needs to capture an image every 7 meters to achieve the necessary overlap. However, at a flight speed of 16 meters per second, the UAV travels too quickly for the camera to take the necessary images. Given that the minimum interval between photos for the monochrome sensor is 0.5 seconds, at a velocity of 16 m/s, photographs would be taken every 8 meters, not the required 7 meters. To ensure adequate image capture, the UAV would need to reduce its speed to at least 14 m/s, allowing the camera to take a photo every 7 meters.

From all the above parameters, the most suitable altitudes for capturing high-resolution images range between 50 and 90 meters, depending on limitations and the area to be mapped. Table 5 shows that operating at 20 m/s barely allows sufficient time for the camera to take photos every 0.5 seconds at 50 meters altitude. An optimal cruise speed would be between 13 m/s and 20 m/s to complete the mission efficiently. To provide a margin of error and avoid operating too close to the 0.5-second limit, an initial guess for cruise speed will be around 16 m/s.

4.4. Airfoil selection

Given the absence of a horizontal stabilizer on the UAV, the selection of a reflex cambered airfoil becomes crucial. A reflexed camber airfoil is characterized by a camber line that curves upward near the trailing edge (see Figure 17). This design feature is particularly advantageous in tailless aircraft configurations as it allows for the moment about the aerodynamic centre of the airfoil to approach zero or be slightly positive. In simpler terms, this means that the airfoil tends to produce minimal pitch moments, contributing to aerodynamic stability [22].

To delve deeper into the concept, it's essential to understand the significance of aerodynamic stability in aircraft, both conventional and unconventional like flying wings. Aerodynamic stability refers to the aircraft's ability to maintain a steady and predictable flight path without unnecessary oscillations or deviations. In conventional aircraft with horizontal stabilizers and elevators, stability is achieved through careful design to ensure that the aerodynamic forces acting on the aircraft naturally tend to restore it to its original position after disturbances [23].

Flying wings, on the other hand, lack horizontal stabilizers, relying instead on the airfoil's inherent stability characteristics. Here, the reflex cambered airfoil plays a critical role. Understanding how it contributes to longitudinal stability involves two key factors:

- **Total Force and Moment at the c/4 Point:** The pressure forces acting on each wing section can be combined into a single total force and a moment, both acting at the quarter-chord point of the airfoil. When the angle of attack changes, the moment remains relatively constant, but the total force fluctuates. An increase in angle of attack results in a higher force [23].

- **Centre of Gravity:** Translations and rotations of free-floating bodies occur relative to their centre of gravity. As the angle of attack changes, the aircraft pitches around its centre of gravity (c.g.) [23].

In observing a trimmed flight condition where all forces and moments are balanced, a comparison is made between a conventional, cambered airfoil and one with a reflexed camber line. In this equilibrium state, denoted by an asterisk (*), the forces include the weight (m) multiplied by gravity acceleration (g) and aerodynamic lift (L), which cancel each other out in the vertical direction. Neglecting drag forces, the sum of moments around the c.g. must also be zero, accounting for the airfoil moment (M) and lift force (L) acting at a distance from the c.g [23].

Equilibrium state

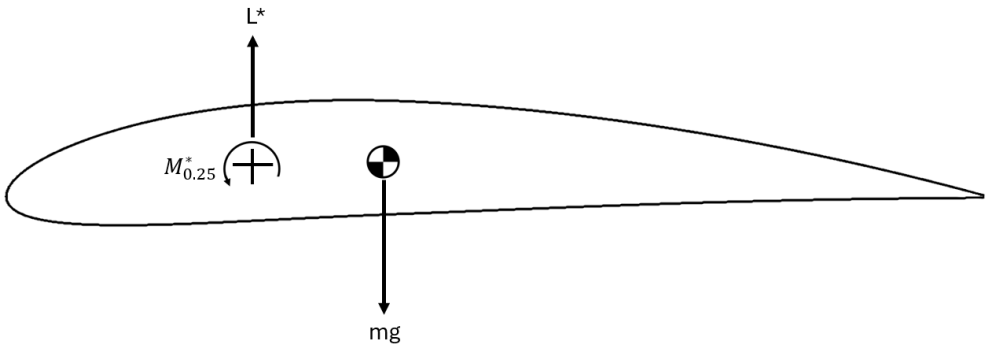

Figure 16: Conventional airfoil with camber at equilibrium.

This airfoil exhibits a nose-heavy moment. As previously mentioned, the centre of gravity also serves as the centre of rotation for the wing. When it is positioned behind the c/4 point, the air force L* in front of the c.g. counterbalances the nose-heavy moment M* to establish equilibrium. The distance between the c.g. and the c/4 point depends on the magnitude of M*. A symmetrical airfoil, with M*=0, necessitates placing the c.g. precisely at the c/4 point.

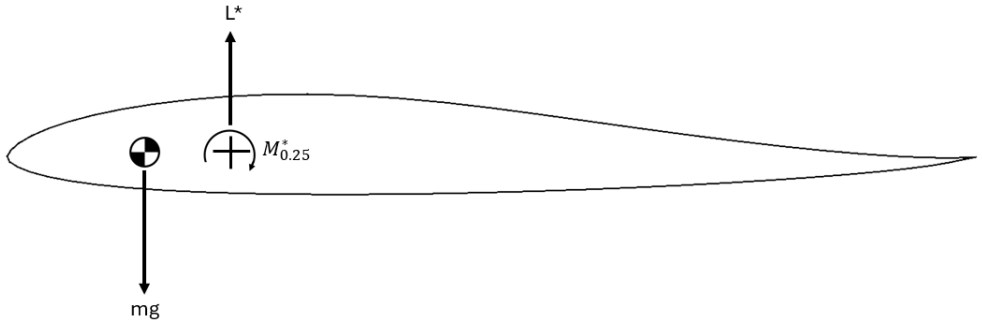

Figure 17: Reflexed airfoil at equilibrium.

The reflexed camber line results in a positive moment coefficient, indicating that the moment around the c/4-point acts in the tail-heavy direction. Consequently, the centre of gravity must be situated ahead of the c/4 point to offset the moment M* with the lift force L*. The magnitude of the moment of the airfoil directly influences the distance between the c/4 point and the c.g. required for equilibrium, with larger moment coefficients necessitating a greater distance between them.

Disturbed state

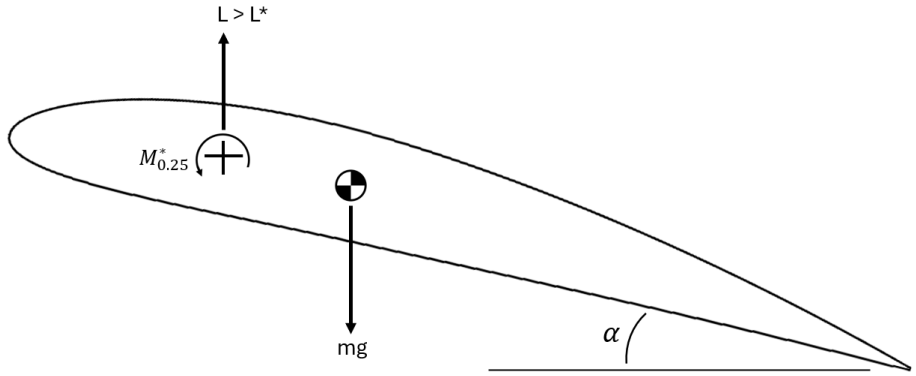

Figure 18: Conventional airfoil with camber disturbed.

As the angle of attack rises (e.g., due to a gust), the lift force L also increases, surpassing L*. Consequently, the tail-heavy moment induced by the lift becomes greater than the moment around the c/4 point, which remains M=M*. As a result, the wing pitches up, further amplifying the angle of attack. This instability necessitates the use of a tailplane to stabilize the system.

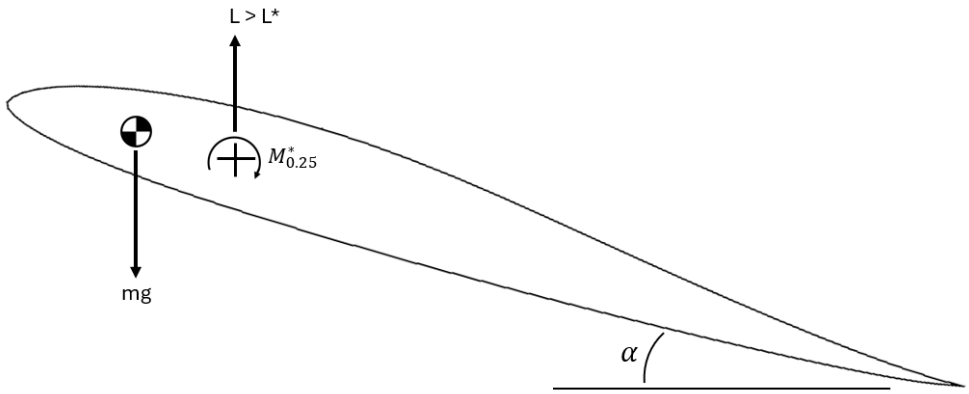

Figure 19: Reflexed airfoil disturbed.

In this scenario, the air force acts behind the centre of gravity, introducing an extra nose-heavy moment when the lift escalates. As L exceeds L*, the wing pitches downward, diminishing the angle of attack until equilibrium is restored. This stability ensures the system remains balanced.

With this understanding, the selection of appropriate airfoils for the UAV becomes paramount. The airfoils identified for study include the EH3.0/12, NACA 24112, NACA 23112, EPPLER 636, EPPLER 333, CLARK YS, US45M, and CLARK Z. These airfoils will undergo an analysis to evaluate their aerodynamic characteristics, stability, and suitability for the UAV's operational requirements. Through careful examination and testing, the most optimal airfoil will be selected to ensure the UAV's safe and stable flight performance.

Airfoil	CLi	$C_{L,max}$	$C_{D,min}$	C_{m0}	α_{stall} [°]	α_0 [°]	(L/D) max	Cl_α [1/rad]	Stall Quality
EH 3.0/12	0.25	1.50	0.006	0.020	13.0	-2.0	84.6	7.45	Moderate
NACA 24112	0.02	1.40	0.008	0.010	14.0	-1.0	85.7	6.88	Moderate
NACA 23112	0.01	1.40	0.007	0.008	14.5	-1.0	82.0	7.11	Moderate
EPPLER 636	0.10	1.38	0.009	0.019	12.5	-1.0	100	8.60	Sharp
EPPLER 333	0.19	1.40	0.008	-0.010	12.5	-2.5	100	6.88	Moderate
CLARK YS	0.01	1.25	0.007	0.027	11.5	-1.0	80.8	7.26	Sharp
USA 45M	0.39	1.28	0.008	-0.039	12.0	-2.5	89.2	6.17	Docile
CLARK Z	0.50	1.60	0.006	-0.088	15.0	-4.0	100	5.96	Moderate

Table 6: Comparison table between different airfoils.

Design Objectives	C_{Dmin}	C_{m0}	α_{stall}	$(C_L/C_D)_{max}$	$C_{L\alpha}$ [1/rad]	C_{Lmax}	C_{Li}	SUM
Design Values	0.006	0.030	15.0	100	6.50	1.50	0.57	
Weight	10	20	15	10	10	20	15	**100**
EH 3.0/12	10	13.3	13.0	8.46	8.54	20	6.58	**79.9**
NACA 24112	6.66	6.67	14.0	8.57	9.42	18.7	0.53	**64.6**
NACA 23112	8.33	5.33	14.5	8.20	9.06	18.7	0.26	**64.4**
EPPLER 636	5	12.7	12.5	10.0	8.53	18.4	2.63	**73.3**
EPPLER 333	6.66	-6.67	12.5	10.0	9.42	18.7	5.00	**55.6**
CLARK YS	8.33	18	11.5	8.08	8.83	16.7	0.26	**71.7**
USA 45M	6.66	-26	12.0	8.92	9.49	17.1	10.3	**38.5**
CLARK Z	10	-58.7	15.0	10.0	9.17	18.7	13.2	**17.4**

Table 7: Weighted table for selecting best airfoil.

Table 8 shows a weighted table for selecting the best airfoil providing a comparative analysis of various airfoils based on multiple design objectives. Each design objective is assigned a specific weight to reflect its importance in the overall design. The table includes several airfoils, such as EH 3.0/12, NACA 24112, and Eppler 636, with their respective performance values for each design objective. By summing the weighted values, the table provides an overall score for each airfoil, allowing for a clear comparison and selection of the most suitable airfoil for the design requirements. For

instance, the EH 3.0/12 airfoil, with a sum of 79.9, indicates its high suitability compared to others like CLARK Z, which scores significantly lower.

Having these values, it is evident that the most interesting airfoils are the EPPLER 636 (Figure 20) and the EH 3.0/12 (Figure 21). The E-636 airfoil is selected since it meets all the requirements, including maximum lift coefficient, moment coefficient, and maximum lift-to-drag ratio, exceptionally well. The EH3012 also meets all the requirements and features, sticking out in maximum lift coefficient. To further analyse these two airfoils, the Reynolds number at which they will operate will be calculated first.

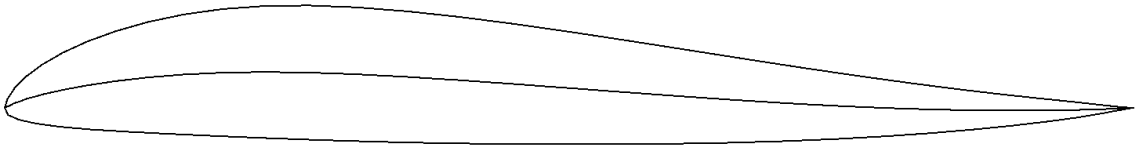

Figure 20: E-636 Airfoil with Camber Line.

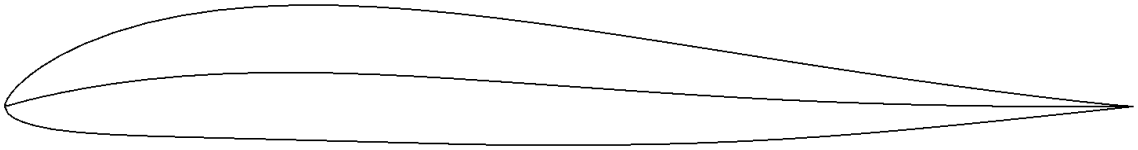

Figure 21: EH 3.0/12 airfoil.

The design lift coefficient is calculated to select the most suitable airfoil for the aircraft mission. The design lift coefficient is calculated using the aircraft cruise speed, using the following formula:

$$L = W = \frac{1}{2}\rho V^2 S C_L$$

Where;

$W = 2.92\ \text{Kg} \cdot 9.81 \frac{\text{m}}{\text{s}^2} = 28.65\ N$

$S = 0{,}370\ m^2$ (a rough estimate using UAVs shown in Table 1)

$V_{cruise} = 16\ \text{m}/s$

$\rho = 1.2\ \text{Kg}/m^3$

To simplify calculations, it is assumed that the aircraft's lift coefficient is equal to the airfoil lift coefficient. With that in mind, the following equation is used:

$$C_L = \frac{2W}{\rho V^2 S} = \frac{2 \cdot 28.65}{1.2 \cdot 16^2 \cdot 0.370} = 0.504$$

Based on the analysis of similar VTOL aircraft, it is observed that most have a thickness-to-chord ratio (t/c) ranging between 12% and 14%. Given that a t/c ratio of 14% might be excessive for airfoils such as the EH 3.0/12 and EPPLER 636, an initial estimation of 12% will be considered more appropriate. Starting with a 12% t/c ratio provides a balanced approach, ensuring both structural integrity and aerodynamic efficiency. This initial guess serves as a baseline for further refinement through detailed design iterations and performance analysis, allowing adjustments to be made as more data becomes available and specific design requirements are clarified.

$$\frac{t}{c} \approx 0.12 = 12\%$$

At this thickness-to-chord ratio of 12%, using Raymer's historical trend data, the following maximum lift coefficient is estimated for the design.

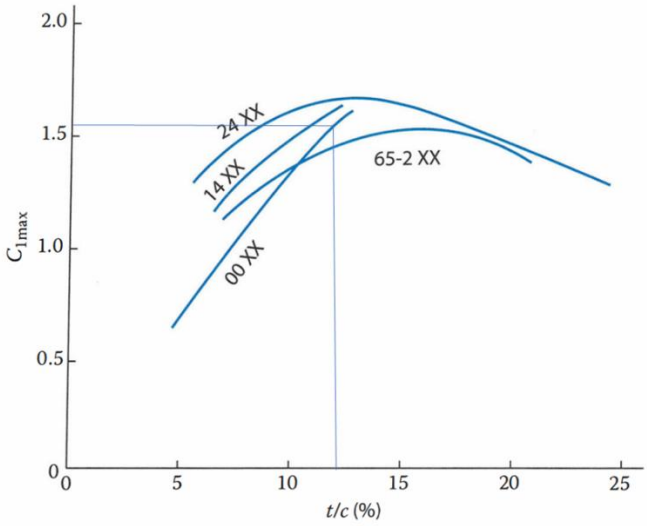

Figure 22: Thickness ratio vs. lift coefficient trend [24].

$$\boldsymbol{C_{L_{max}} = 1.5}$$

Maximum lift coefficient for the entire aircraft will be,

$$C_{L_{MAX}} = 0.99 \times C_{l_{max}} \times cos\Delta_{0.25c} = 1.36 \sim 1.4\ (Initial\ guess)$$

So, the stall speed can now be calculated as;

$$V_{stall} = \sqrt{\frac{2W}{\rho S C_{l_{max}}}} = \sqrt{\frac{2 \cdot 28.65}{1.2 \cdot 0.370 \cdot 1.4}} = 9.60 \text{ m}/s$$

Reynolds number calculation:

Given that the UAV will primarily operate in Madrid, Spain, it is essential to calculate the Reynolds number based on the atmospheric conditions specific to this region. Madrid sits at an elevation of approximately 657 meters above mean sea level. Considering that the UAV will fly at an altitude ranging from approximately 50 to 80 meters above the ground, the estimated operational altitude is 737 meters. Due to variations in terrain elevation across Madrid, this value will be rounded to 750 meters as the average elevation during flight.

With the elevation set at 750 meters, the kinematic viscosity of the air will be extrapolated using International Standard Atmosphere (ISA) data from 500 meters and 1000 meters.

Elevation -z- [m]	Kinematic viscosity -v- $\cdot 10^{-5}$ [m^2/s]
500	1.520
1000	1.581

Table 8: Kinematic viscosity at different elevations.

$$v(z) = v_1 + \frac{z - z_1}{z_2 - z_1} \cdot (v_2 - v_1)$$

Given that:

$Z = 750\, m$

$Z1 = 500\, m$

$Z2 = 1000\, m$

$v_1 = 1.520 \cdot 10^{-5}\, m^2/s$

$v_2 = 1.581 \cdot 10^{-5}\, m^2/s$

Substituting yields:

$$v(750\, m) = 1.520 \cdot 10^{-5} + \frac{750 - 500}{1000 - 500} \cdot (1.581 - 1.520) \cdot 10^{-5}$$
$$= 1.5505 \cdot 10^{-5} \frac{m^2}{s}$$

Following this, the design Reynolds number is calculated using the following equation.

$$Re = \frac{V \cdot \bar{c}}{\nu}$$

Where $\bar{c}$ is the mean aerodynamic chord of the aircraft. Mean aerodynamic chord is given by the following formula:

$$\bar{c} = MAC = \frac{2C_r(1 + \lambda + \lambda^2)}{3(1 + \lambda)}$$

Where;

$$\lambda = taper\ ratio = \frac{C_{tip}}{C_{root}} = \frac{C_t}{C_r}$$

Using averaged values of root and tip chords from the reference aircraft in Table 1, the taper ratio is calculated as follows:

$$\lambda = \frac{C_t}{C_r} = \frac{0.30}{0.38} = 0.789$$

$$\bar{c} = MAC = \frac{2 \times (0.38)(1 + 0.789 + 0.789^2)}{3(1 + 0.789)}$$

$$\bar{c} = 0.341 \text{ m}$$

Given the cruise speed at 16 m/s and the kinematic viscosity, the Reynolds number can now be calculated.

$$Re = \frac{V \cdot \bar{c}}{\nu} = \frac{16 \cdot 0.341}{1.5505 \cdot 10^{-5}} = 352{,}388 \cong 350{,}000\ Re$$

Using the software XFLR5, both airfoils will be analysed at a 350,00 Re across different angles of attack to compare their performance. XFLR5 employs panel methods and vortex lattice algorithms to simulate and analyse the aerodynamic properties of airfoils, wings, and planes, providing insights into their lift, drag, and moment characteristics [25]. For the purpose of this initial comparison, XFLR5 will be an ideal tool.

Below are the most important graphs comparing the EH 3.0/12 (blue line) and Eppler 636 (red line) airfoils. As shown, the performance characteristics of both airfoils are quite similar. The Eppler 636 performs slightly better in terms of lift coefficient and lift-to-drag ratio. The moment coefficients for both airfoils are very close, with minimal differences observed.

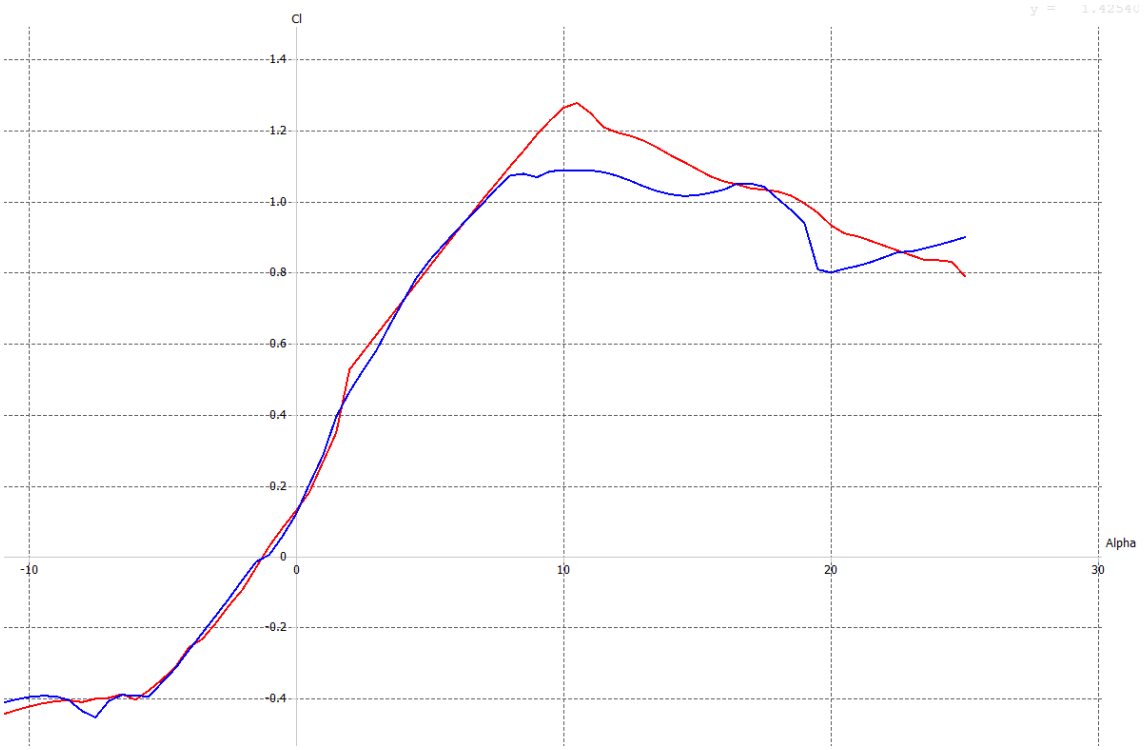

Figure 23: Lift coefficient vs. angle of attack (Cl vs. AoA).

The graph of lift coefficient versus angle of attack reveals that the EH 3.0/12 airfoil and the Eppler 636 airfoil have similar performance characteristics up to approximately 8 degrees AoA. Beyond this point, the Eppler 636 airfoil shows a higher maximum lift coefficient, peaking slightly higher than the EH 3.0/12. This indicates that while both airfoils perform similarly at moderate AoA, the Eppler 636 can generate more lift at higher AoA, which is beneficial for achieving higher lift during critical phases of flight.

In Figure 24 the drag coefficient versus AoA shows that both airfoils exhibit similar drag characteristics across all range. However, the Eppler 636 airfoil consistently maintains a slightly lower drag coefficient at between 8º and 15º. As the AoA increases, the performance switches several times between both airfoils, but since at this point the airfoil is already stalled, the results are not very reliable.

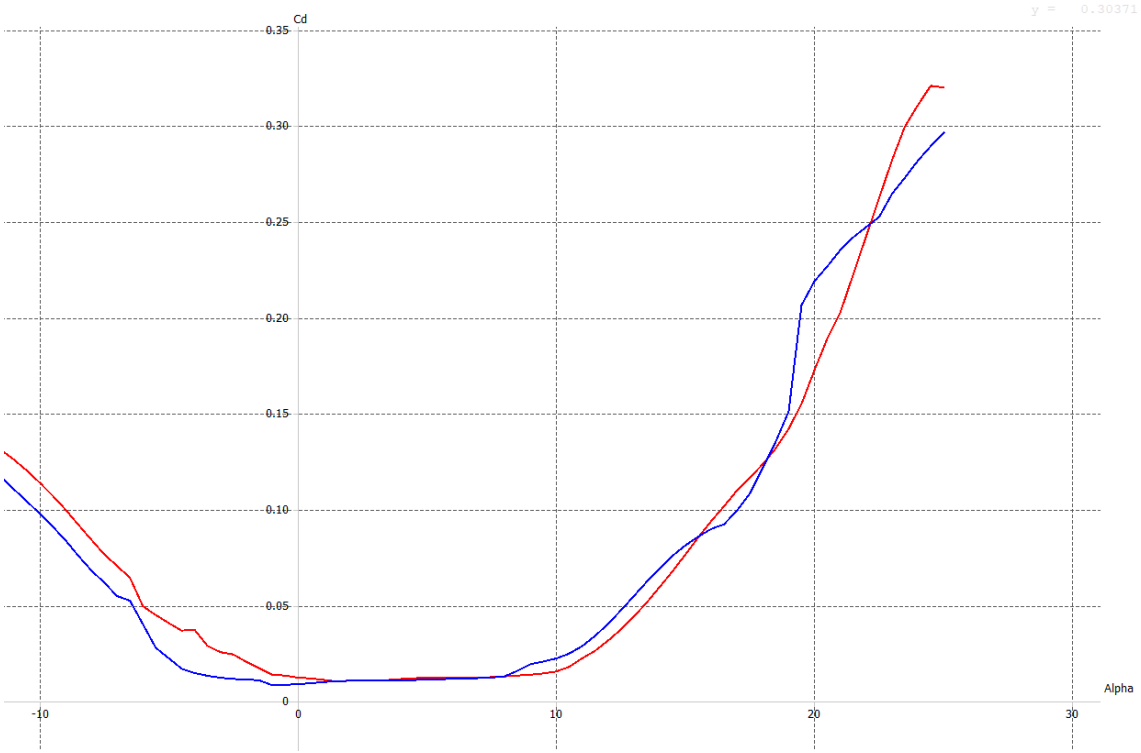

Figure 24:Drag coefficient vs. angle of attack (Cd vs. AoA).

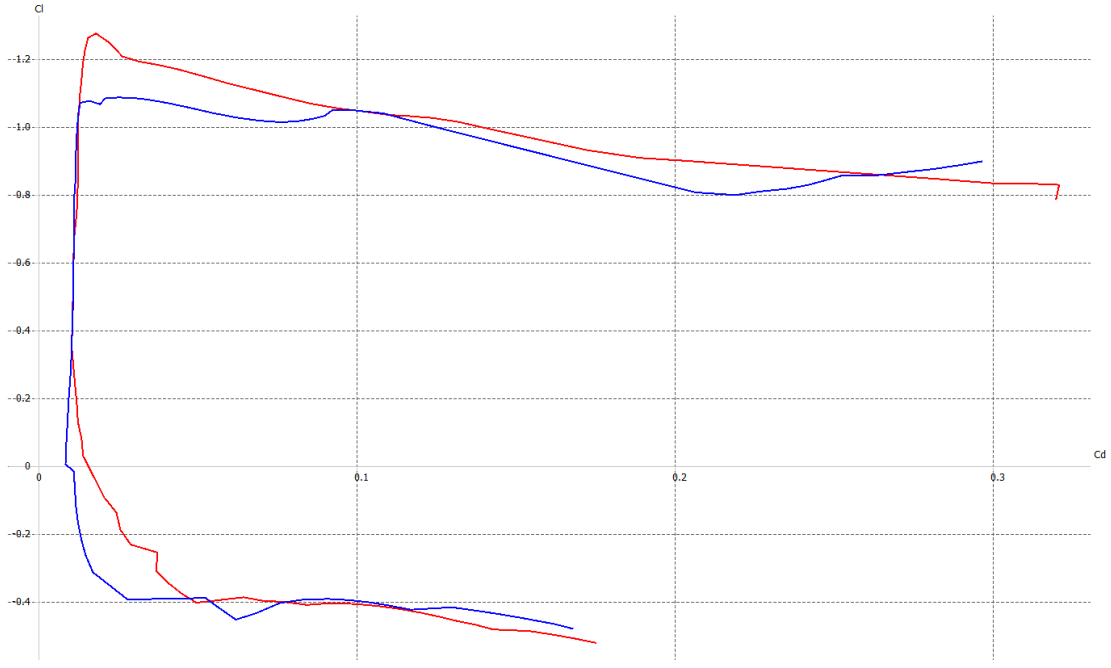

Figure 25:Drag polar (Cl vs. Cd).

The drag polar plot, depicting Cl against Cd, shows that the EH3.0/12 airfoil generally performs better in lower Cl values. As Cl values increase, the performance of both airfoils becomes more similar.

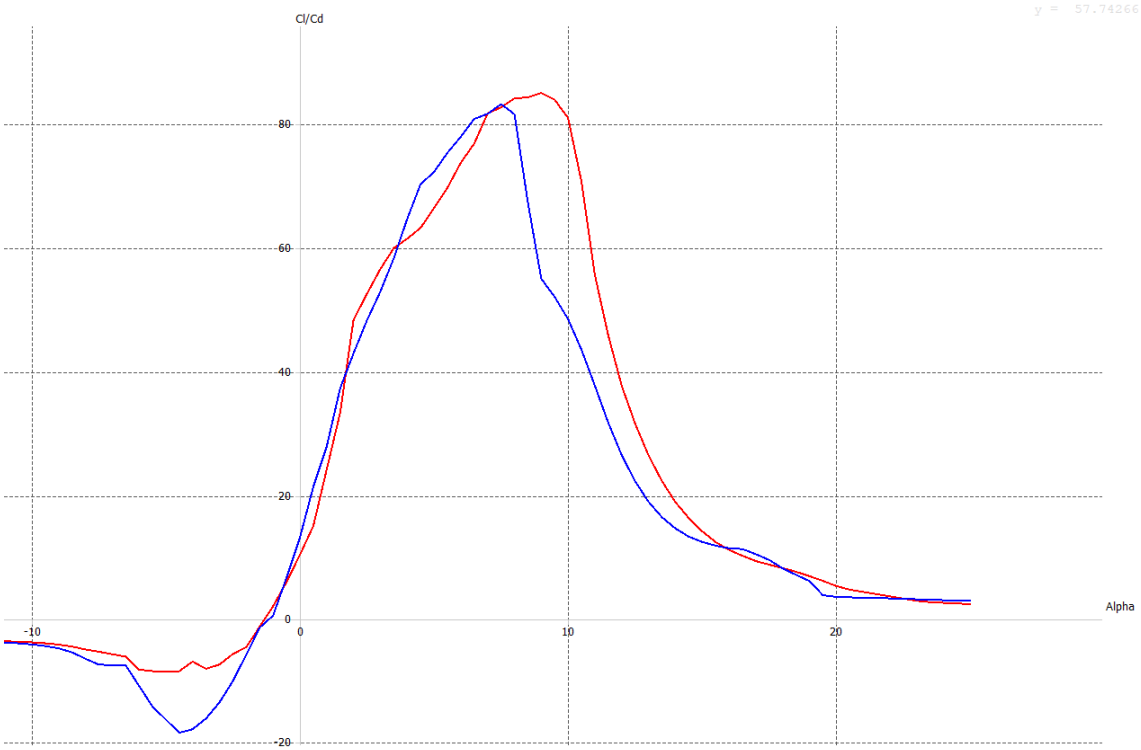

Figure 26: Lift-to-Drag ratio vs. angle of attack (Cl/Cd vs. AoA).

The lift-to-drag ratio versus AoA plot further reinforces the superior efficiency of the Eppler 636 airfoil. This airfoil consistently achieves a higher Cl/Cd ratio compared to the EH 3.0/12 airfoil, particularly near 10º AoA. This higher efficiency translates to better performance in terms of energy utilization, making the Eppler 636 more suitable for sustained flights.

For the last plot (Figure 27), the moment coefficient versus AoA indicates that both airfoils have similar moment characteristics. The EH 3.0/12 airfoil exhibits slightly more positive moment behaviour near 0º, while the Eppler 636 airfoil shows a more negative moment. As explained above, the moment coefficient is a crucial factor since the UAV will not have an HTP. The selected airfoil must have a natural tendency to restore stability, in other words, a positive moment.

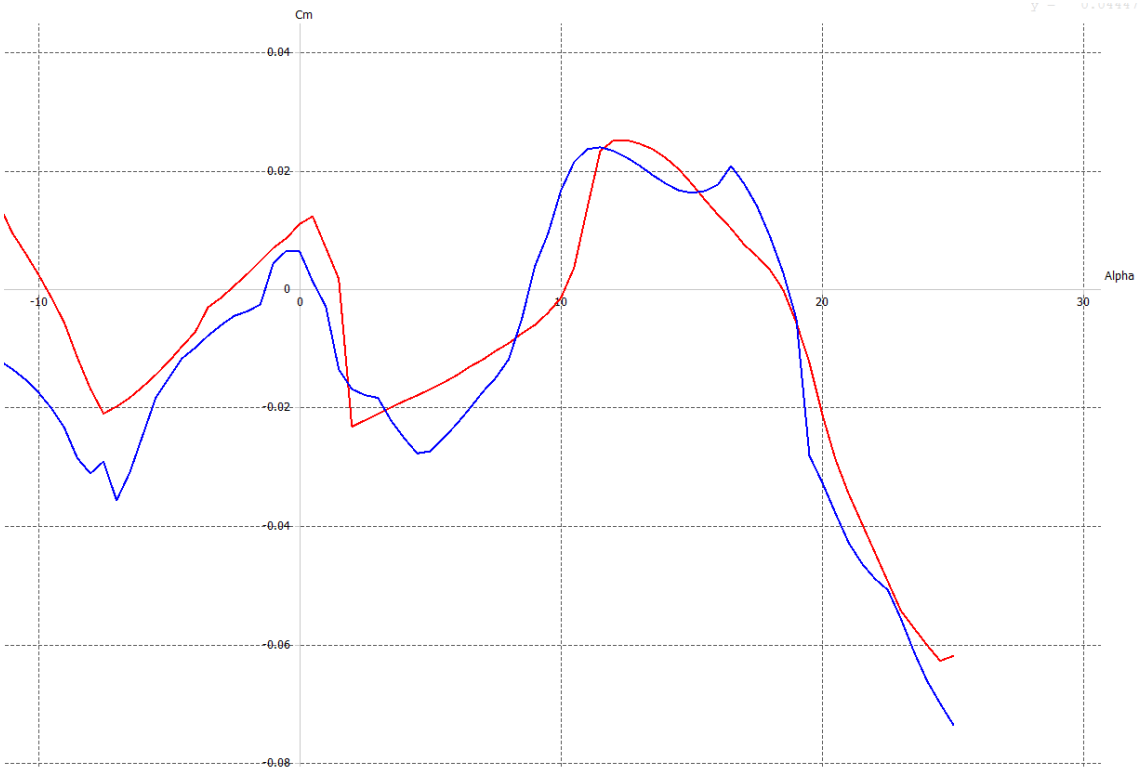

Figure 27: Moment coefficient vs. angle of attack (Cm vs. AoA).

After thorough analysis of the two candidates, the EH 3.0/12 and the Eppler 636, several factors were considered, including lift coefficient, drag coefficient, and moment coefficient. The EH 3.0/12 airfoil demonstrated favourable characteristics in terms of stall behaviour and stability. However, the Eppler 636 consistently outperformed the EH 3.0/12 in critical areas such as lift-to-drag ratio and moment coefficient. This superior performance, particularly in the desired operational range, makes the Eppler 636 the more suitable choice for the VTOL aircraft design.

4.5. Geometry Sizing

The geometric sizing phase represents the next crucial step in the UAV design journey, building upon the airfoil selection groundwork. During this phase, the elaborate details shaping the physical form and performance of the VTOL UAV are addressed. This comprehensive process encompasses several interlinked components and systems, each meticulously designed to meet the project's objectives.

4.5.1. Sizing and Constraint Plot

Using a straightforward AAA code and incorporating various constraints derived from initial parameters, the following plot can be generated:

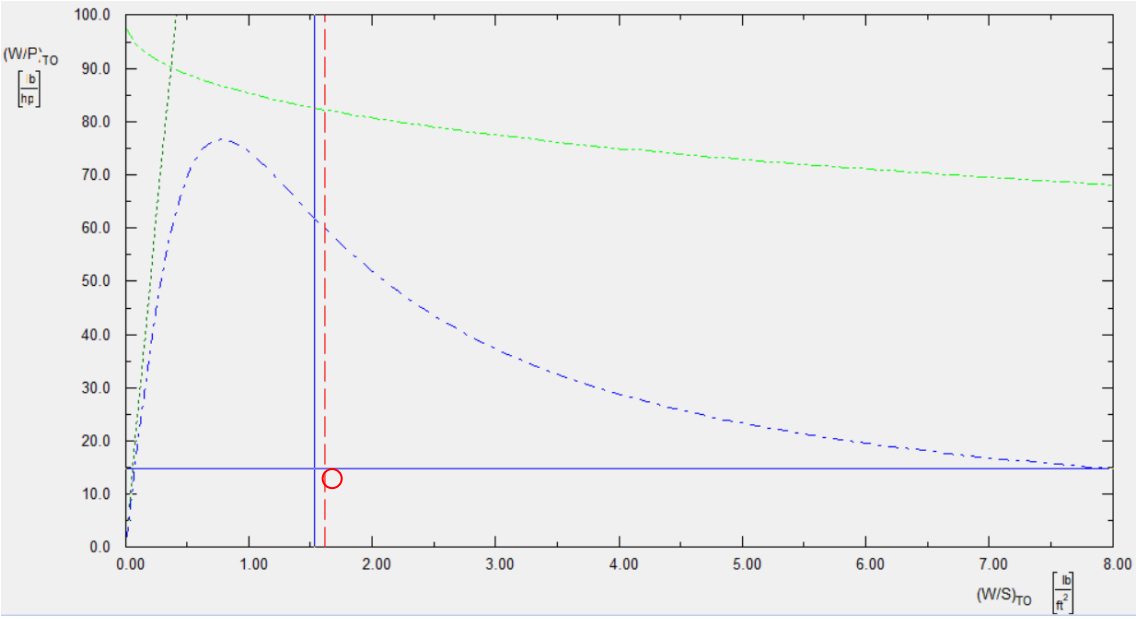

Figure 28: Performance sizing constraint plot.

In Figure 28, the red circle indicates the position of the designed aircraft within all the constraints. This design point represents a trade-off between power loading, wing loading, wing area, and power required. Reducing the power loading further would significantly increase the power required, necessitating much heavier motors to meet this demand. This would, in turn, lead to an unreasonable increase in overall weight. Therefore, this trade-off design point was selected to balance all these limitations. At this design point, the following values are achieved:

Parameter	Value
Maximum Take-off Weight	2.92 Kg
Wing Loading (Vertical blue line)	7.48 Kg/m^2
Power Loading (Horizontal blue line)	87.67 N/kW
Wing Area	0.37 m^2

Table 9: Wing loading & power loading.

As an initial value for the wingspan, a value similar to the aircrafts in Table 1 will be used. Thus, the wingspan will be approximately 1.5 meters, giving an aspect ratio of;

$$AR = \frac{b^2}{S} = \frac{1.5^2}{0.37} = 6.08$$

4.5.2. Wing Sizing

The wings of the UAV are pivotal aerodynamic elements that shape its flight characteristics. In this phase, the wings are carefully sized and designed to optimize lift, minimize drag, and ensure stability. Key parameters such as wingtips, taper ratio, root and tip chord length, and aerodynamic chord length are considered to achieve the desired performance across a spectrum of flight regimes.

- **Wingtip**

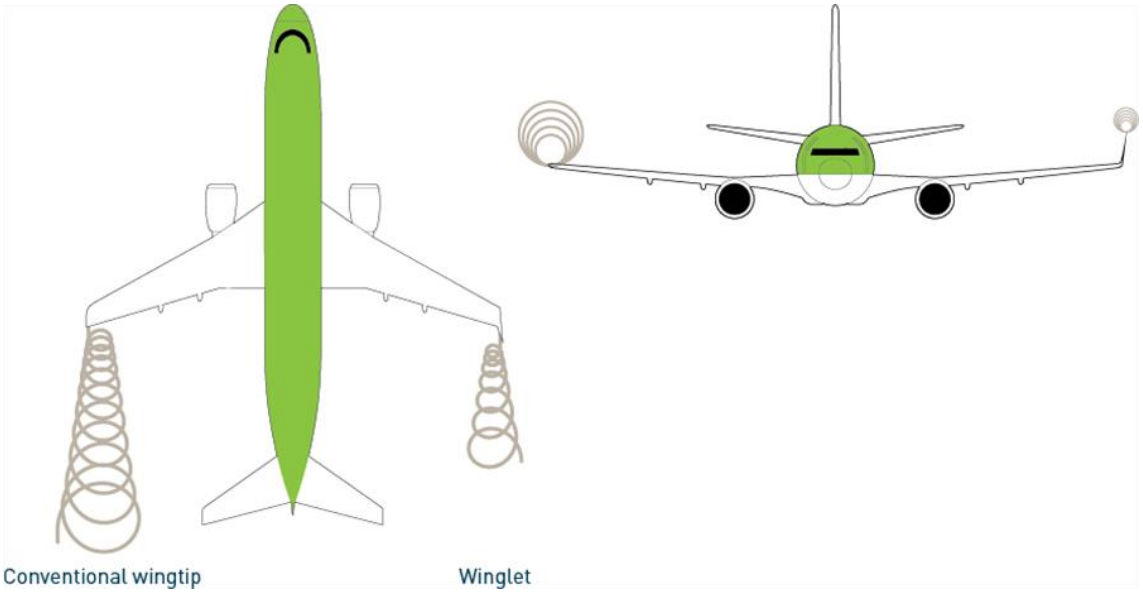

Figure 29: Wingtip vortices size comparison between a conventional wingtip and a winglet.

Induced drag is caused by the creation of wingtip vortices, which are spirals of air generated at the tips of the wings as high-pressure air from beneath the wing flows to the low-pressure area above the wing. Wingtips help to minimize these vortices, thereby reducing induced drag. By reducing drag, wingtips improve the overall lift-to-drag ratio, making the aircraft more efficient.

For the VTOL, wingtips provide several specific advantages. Firstly, by reducing drag, wingtips can significantly improve the efficiency of the UAV, allowing to fly longer distances on the same amount of battery power. This enhanced aerodynamic efficiency translates to an extended operational range, enabling the UAV to cover larger areas.

Moreover, minimizing wingtip vortices not only reduces drag but also reduces aerodynamic noise, making the VTOL quieter during operation, which is beneficial for not disturbing livestock and wildlife. Effective wingtip designs can also distribute aerodynamic loads more evenly, reducing stress on the wings and potentially increasing the lifespan [26].

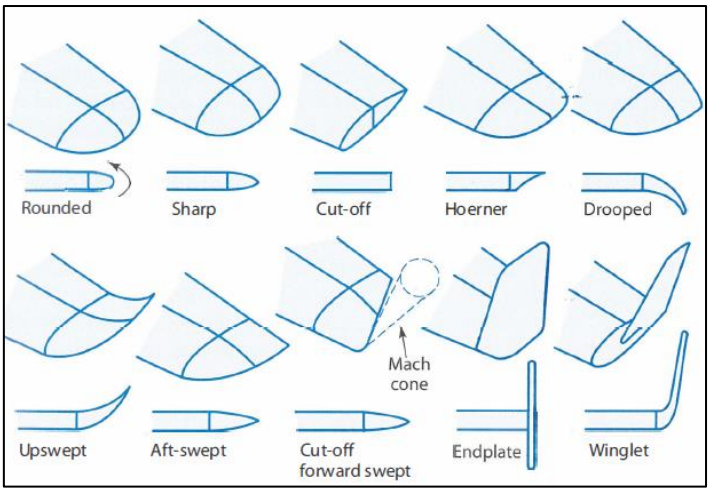

Figure 30: Selection of most common wing tips.

In Figure 30, various wingtip devices used in aviation are depicted, each offering distinct advantages and purposes. Among the most common are winglets and upswept tips. For the VTOL's initial design, winglets have been chosen due to their ability to reduce drag through low vortex generation.

- **Taper Ratio**

For the reflexed airfoil, a smaller taper ratio (closer to 1) and leading-edge sweep are required, as it functions similarly to a tail section, providing a positive moment. Therefore, for the Eppler 636 airfoil, the following taper ratio and leading-edge sweep angle will be employed:

$$Taper\ Ratio = \lambda_{\text{Eppler 636}} = 0.85$$

A sweep angle of zero is initially chosen to simplify the analysis.

- **Root Chord**

For Eppler 636:

$$\mathrm{C}r_{\text{Eppler 636}} = \frac{2 \cdot \mathrm{S}}{\mathrm{b} \cdot (1 + \lambda)} = \frac{2 \cdot 0.37}{1.50 \cdot (1 + 0.85)} = 0.27\ m$$

- **Tip Chord**

Using the formula for taper ratio;

$$\lambda = \frac{C_t}{C_r}$$

$$C_{t_{\text{Eppler 636}}} = \lambda_{\text{Eppler 636}} \times C_{r_{\text{Eppler 636}}} = 0.85 \cdot 0.27 = 0.23 \text{ m}$$

- **Mean aerodynamic chord**

$$\overline{c_{\text{Eppler 636}}} = \frac{2}{3} C_r \left(\frac{1 + \lambda + \lambda^2}{1 + \lambda} \right) = \frac{2}{3} \cdot 0.27 \cdot \left(\frac{1 + 0.85 + 0.85^2}{1 + 0.85} \right) = 0.25\, m$$

- **Location of mean aerodynamic chord**

$$\overline{y_{\text{Eppler 636}}} = \frac{b \cdot (1 + 2\lambda)}{6 \cdot (1 + \lambda)} = \frac{1.5 \cdot (1 + 2(0.85))}{6(1 + 0.85)} = 0.36\, m$$

4.5.3. Fuselage geometry

The fuselage acts as the structural foundation of the UAV, housing critical components and the payload. Careful sizing is undertaken to accommodate the necessary equipment while preserving aerodynamic efficiency.

- **Fuselage length**

An initial guess for the fuselage length can be determined from historical data extracted from Raymer's book [24].

Length = aW_0^C [m]	a	C
Sailplane-unpowered	0.383	0.48
Sailplane-powered	0.316	0.48
Homebuilt metal/wood	1.35	0.23
Homebuilt composite	1.28	0.23
General aviation - single engine	1.6	0.23
General aviation - twin engine	0.366	0.42
Agricultural aircraft	1.48	0.23
Twin turboprop	0.169	0.51
Flying boat	0.439	0.40

Table 10: Fuselage length vs Wo [Kg].

$$L_f = \text{Length} = aW_o^C$$

- $a = 0.316$
- $C = 0.48$
- $W_o = 2.92\ \text{Kg}$

$$L_f = 0.316 \cdot 2.92^{0.48} = 0.53\ m$$

- **Maximum Diameter**

The maximum diameter can be found using the fineness ratio;

$$\text{Fineness Ratio} = \frac{\text{Fuselage length}}{\text{Maximum diameter}}$$

Typical values of fineness ratio for low subsonic aircraft ranges between 4 to 6 [24]. As an initial guess a value of 5 will be chosen.

$$\text{Max. Diameter} = \frac{0.53}{5} = 0.11\ m$$

4.5.4. Tail Geometry

The tail assembly assumes a critical function in controlling and stabilizing the UAV. The design process for the tail encompasses factors like tail volume coefficient, tail area, span, and the positioning of mean aerodynamic chord, root, and tip chords. The sizing of the vertical tail follows a methodology similar to that used for wing sizing.

- **Tail Volume Coefficient**

Tail volume coefficients are given by;

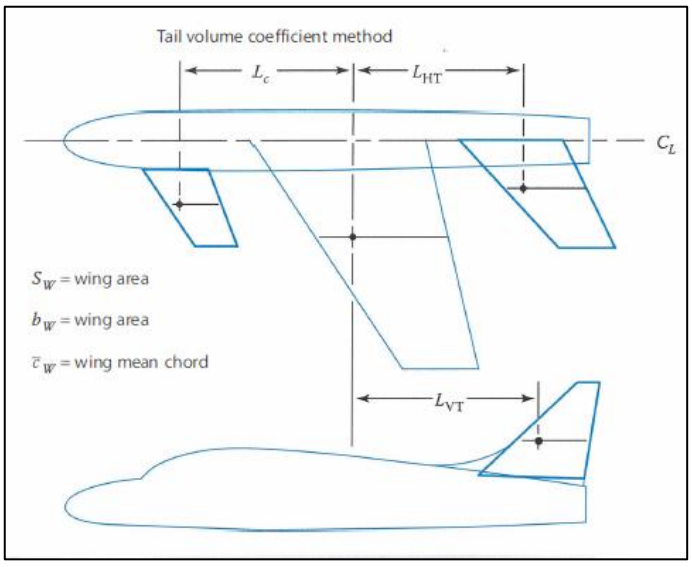

Figure 31: Initial tail sizing [24].

$$C_{HT} = \frac{L_{HT} \cdot S_{HT}}{C_w \cdot S_w}$$

$$C_{VT} = \frac{L_{VT} \cdot S_{VT}}{b_w \cdot S_w}$$

Given the tail sitter configuration of the aircraft, there is no horizontal tail section involved in the UAV design. Accordingly, calculations are focused solely on the vertical tail. The value of the vertical tail volume coefficient is determined based on historical trends outlined by Raymer [24].

	Typical values	
	Horizontal C_{HT}	Vertical C_{VT}
Sailplane	0.50	0.02
Homebuilt	0.50	0.04
General aviation- single engine	0.70	0.04
General aviation – twin engine	0.80	0.07
Agricultural	0.50	0.04
Twin turboprop	0.90	0.08
Jet trainer	0.70	0.06

Table 11: Tail volume coefficient.

$$C_{VT} = 0.02$$

- **Tail Area**

The formula provided below allows for the calculation of the vertical tail area (S_{VT}), which is determined by [24];

$$S_{VT} = \frac{(C_{VT} b_w S_w)}{L_{VT}}$$

Where;

C_{VT}: vertical tail volume coefficient

b_w: wingspan

S_w: wing area

L_{VT}: tail arm length

The tail arm length varies depending on the engine configuration of the aircraft. For a front-mounted propeller engine, the tail arm typically accounts for approximately 60% of the fuselage length. In contrast, for aircraft with wing-mounted engines, this percentage ranges from 50% to 55%, while for those with aft-mounted engines, it falls between 45% and 50% [24].

Hence, $L_{VT} = 0.55\ L_f$,

$$S_{VT} = \left(\frac{0.02 \times 1.50 \times 0.37}{0.55 \times 0.53}\right) = 0.038\ m^2$$

- **Tail span**

Similarly, for the VTP, the aspect ratio selected is 1.7, extracted from Raymer's historical trend (Table 13) [24].

	Horizontal Tail		Vertical Tail	
	AR	λ	AR	λ
Fighter	3 - 4	0.2 - 0.4	0.6 - 1.4	0.2 - 0.4
Sailplane	6 - 10	0.3 - 0.5	1.5 - 2.0	0.4 - 0.6
Others	3 - 5	0.3 - 0.6	1.3 - 2.0	0.3 - 0.6
T-tail	-	-	0.7 - 1.2	0.6 - 1.0

Table 12: Tail aspect ratio.

$$b_{VT} = \sqrt{AR_{VT} \times S_{VT}} = \sqrt{1.7 \times 0.038} = 0.25\ m$$

- **Tail root chord**

As for the taper ratio of the VTP a value of 0.4 is taken [24].

$$C_{r_{VT}} = \frac{2 \cdot S_{VT}}{b_{VT}(1 + \lambda_{VT})} = \frac{2 \cdot 0.038}{0.25(1 + 0.4)} = 0.22\ m$$

- **Tail tip chord**

$$C_{t_{VT}} = \lambda_{VT} \times C_{r_{VT}} = 0.4 \cdot 0.22 = 0.088\ m$$

- **Tail mean aerodynamic chord**

$$\overline{C_{VT}} = \frac{2}{3} C_{r_{VT}} \frac{1 + \lambda_{VT} + \lambda_{VT}^2}{1 + \lambda_{VT}} = \frac{2}{3} 0.22 \left(\frac{1 + 0.4 + 0.4^2}{1 + 0.4}\right) = 0.16\ m$$

- **Location of mean aerodynamic chord**

$$\overline{y_{VT}} = \frac{b_{VT}(1 + 2\lambda_{VT})}{6(1 + \lambda_{VT})} = \frac{0.25(1 + 2 \cdot 0.4)}{6(1 + 0.4)} = 0.054\ m$$

4.5.5. Control surfaces geometry

The primary control surfaces in an aircraft are the ailerons (roll), elevator (pitch), and rudder (yaw). Final sizing of these surfaces is based on a dynamic analysis of control effectiveness, including structural bending and control-system effects. For initial design, Raymer's historical data is used [24].

In this design, there will be only elevons, which combines the functions of both aileron and elevator. Since the elevons will be mounted on the wing the aileron sizing technique is applied.

Elevons typically extend from about 50% to about 90% of the wingspan. Control surfaces are usually tapered in chord by the same ratio as the wing or tail surface so that the control surface maintains a constant percent chord. This design allows spars to be straight tapered rather than curved. Ailerons/elevons and flaps are typically about 15-25% of the wing chord [24]. For this design, 25% is assumed.

$$\text{Elevons chord} = 0.25 \cdot \overline{C_{\text{Eppler 636}}} = 0.25 \cdot 0.25 = 0.063\ \text{m}$$

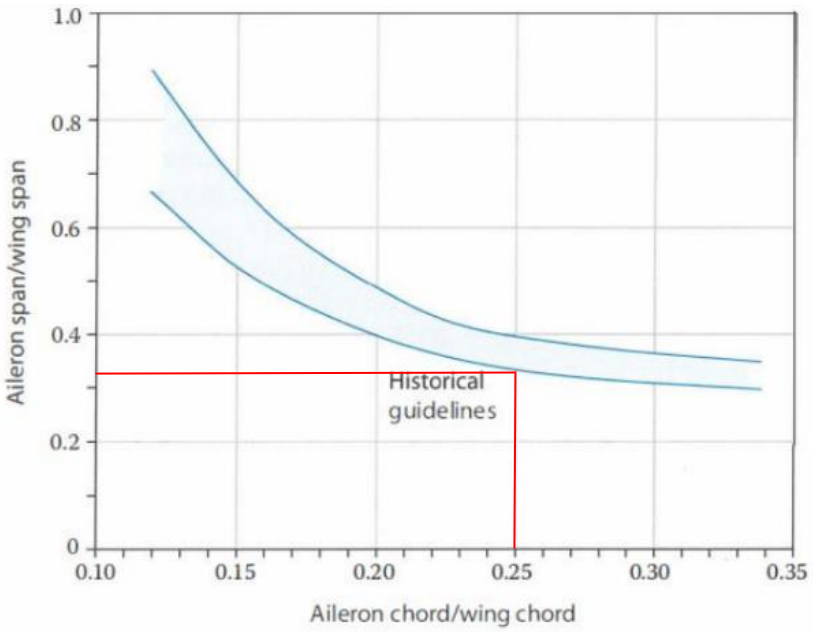

Figure 32:Statistical data for ailerons [24].

At 0.25, the ratio of elevon span/wingspan is around;

$$\frac{\text{Elevons span}}{\text{Wing span}} = 0.33$$

$$\text{Elevons span} = 0.33 \cdot \text{Wingspan} = 0.33 \cdot 1.50 \approx 0.50 \text{ m}$$

4.5.6. Geometry sizing summary

Wing and fuselage parameters	Value
Airfoil	Eppler 636
Wingspan	1.50 m
Wing reference area	0.37 m^2
Root chord	0.27 m
Tip chord	0.23 m
Wing LE Sweep	0º
Dihedral	0º
Taper ratio	0.85
Aspect ratio	6.08
Mean aerodynamic chord	0.25 m
Location of MAC	0.36 m
Fuselage length	0.53 m
Max diameter	0.11 m

Table 13: Wing and fuselage sizing parameters.

Tail Parameters	Value
Tail area	0.038 m^2
Tail AR	1.7
Tail span	0.25 m
Root chord	0.22 m
Tip Chord	0.088 m
Mean aerodynamic chord	0.16 m
Location of MAC	0.054 m
Elevon chord	0.063 m
Elevon span	0.50 m

Table 14: Tail and control surface geometry parameters.

4.6. Wing design

In this chapter, the analysis for the final wing design is performed using XFLR5 software. To further enhance the robustness of the assessment and ensure that design choices are not overly dependent on a single Reynolds number (350,000), a batch analysis is being undertaken. This batch analysis involves evaluating the airfoil across a range of Reynolds numbers, spanning from 200,000 to 500,000. This wide spectrum of Reynolds numbers encompasses various operating conditions, from low speed to high-speed flight regimes.

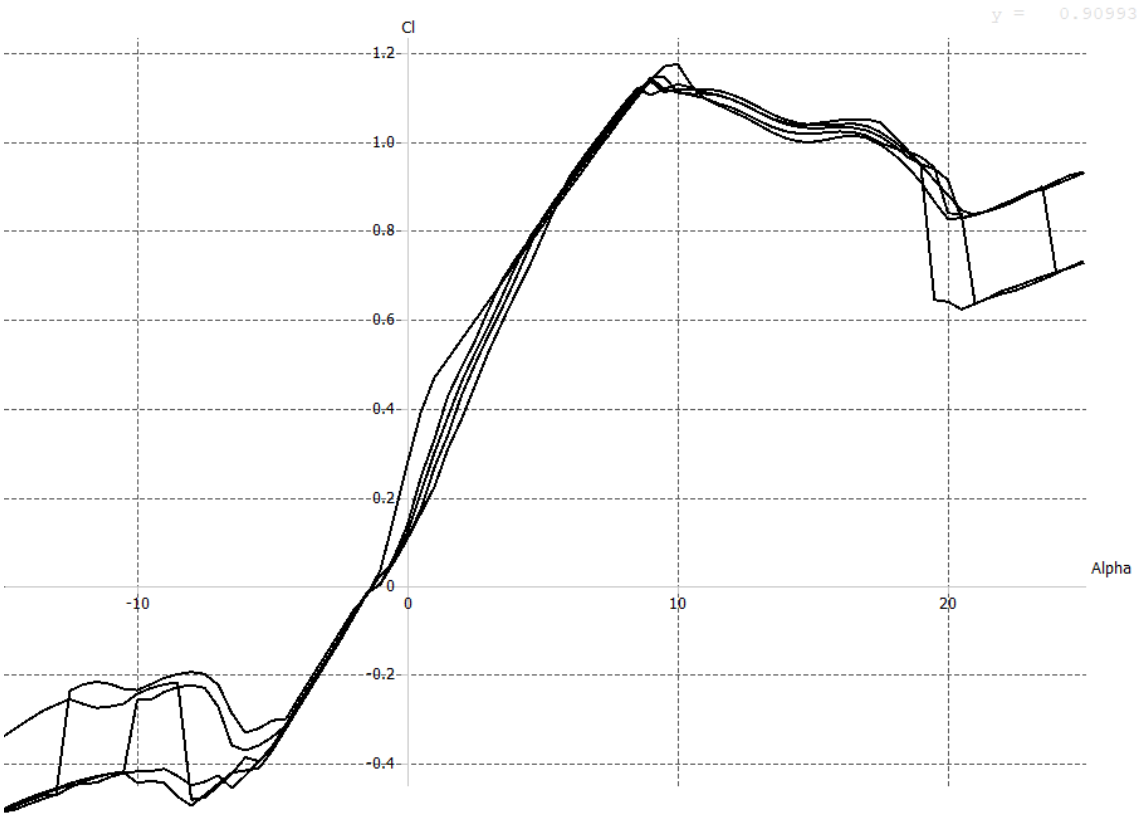

Figure 33: Lift coefficient vs. AoA of Eppler 636 airfoil between 200,000 Re and 500,000 Re.

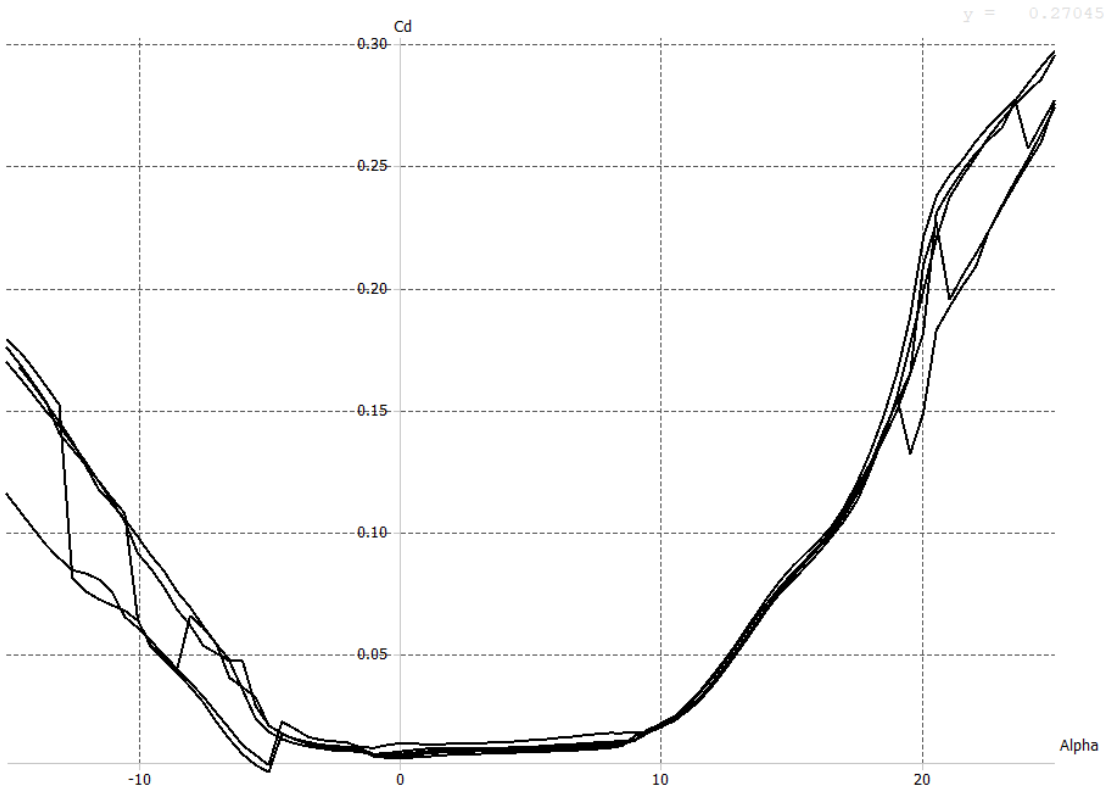

Figure 34: Drag coefficient vs. AoA of Eppler 636 airfoil between 200,000 Re and 500,000 Re.

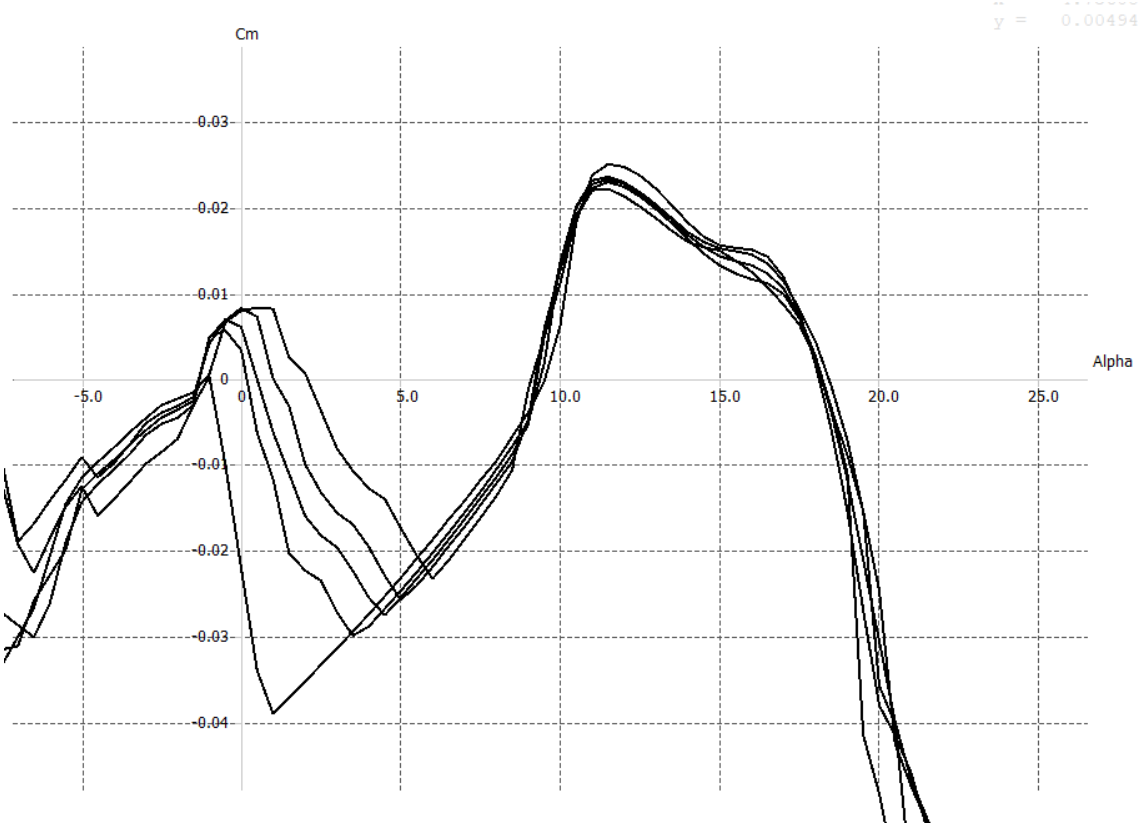

Figure 35: Moment coefficient vs. AoA of Eppler 636 airfoil between 200,000 Re and 500,000 Re.:

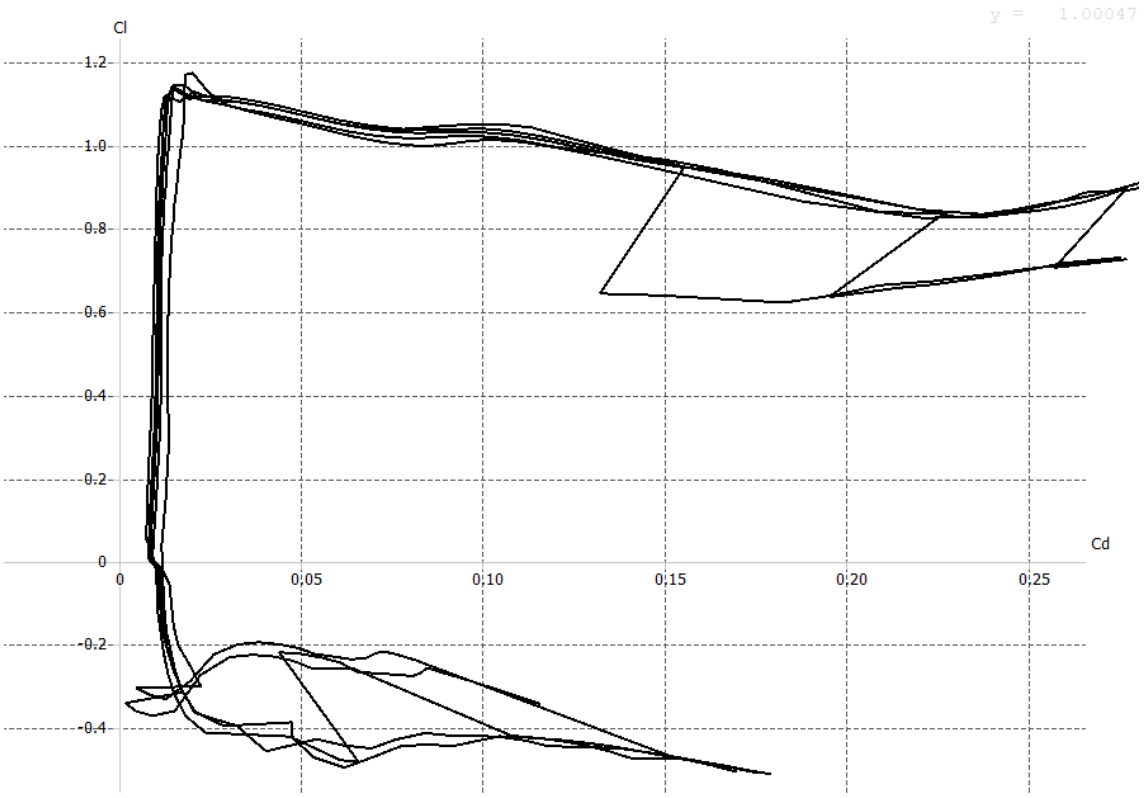

Figure 36: Lift coefficient vs. drag coefficient of Eppler 636 airfoil between 200,000 Re and 500,000 Re.

The foundation behind this batch analysis is dual. Firstly, it enables examination of how the airfoil perform across a broader range of Reynolds numbers, providing a comprehensive understanding of the aerodynamic behaviour under diverse flight conditions.

Secondly, it helps identify any significant variations in performance metrics, such as lift, drag, and moment coefficients, as the Reynolds number changes. This general approach ensures that the choice of airfoil remains robust and flexible to a wider array of operational scenarios, ultimately enhancing the overall performance and versatility of the aircraft design. Results have been converged for angles of attack between -5° to 20°.

As observed, the results are consistent through all the regimes, confirming that the airfoil's behaviour aligns with anticipated trends as the Reynolds number increases. However, a notable difference is observed in Figure 35, where the moment coefficient tends to increase between 0º and 5º, resulting in a more positive moment. This occurs because at these angles of attack, the airflow dynamics around the airfoil change, leading to variations in the pressure distribution and subsequently affecting the pitching moment.

As an initial step, a 1.5-meter wingspan wing will be created without winglets. The parameters for this wing will match those described in Table 14.

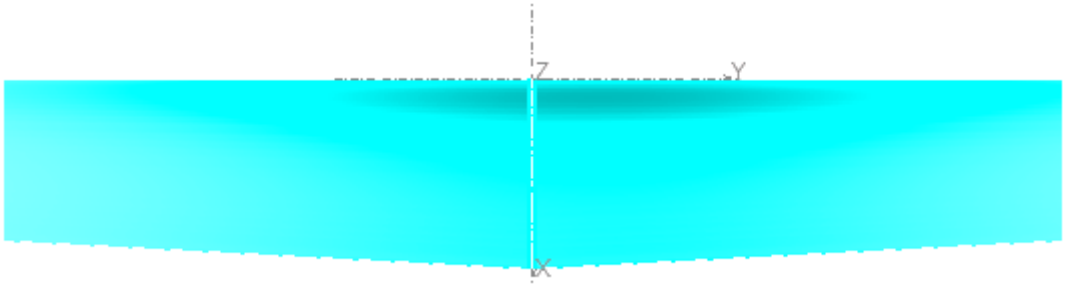

Figure 37: 1.5-meter wing in XFLR5 software.

Now, key aerodynamic parameters such as lift, drag, and moment coefficients will be evaluated. This detailed wing analysis is crucial for assessing how it interacts with the specific cruise speed of 16 m/s, providing vital insights into its aerodynamic efficiency and behaviour.

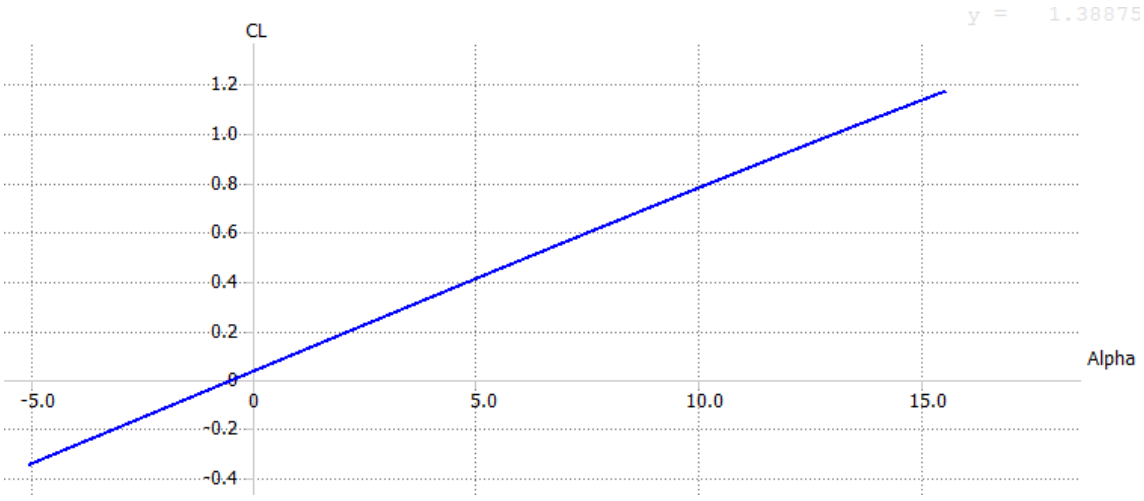

Figure 38: Lift coefficient CL vs. AoA.

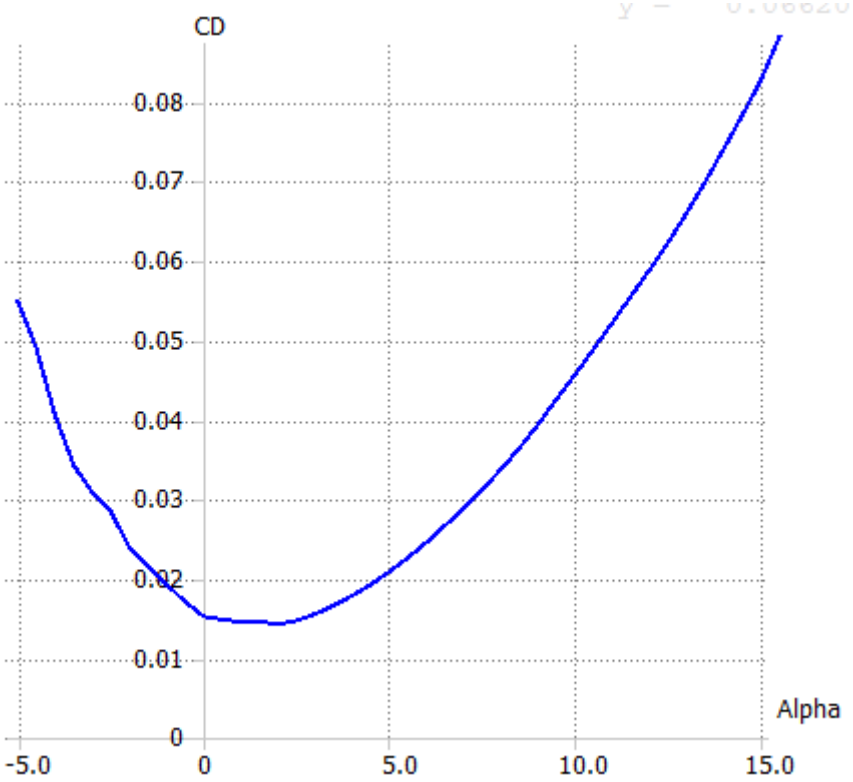

Figure 39: Drag coefficient CD vs. AoA.

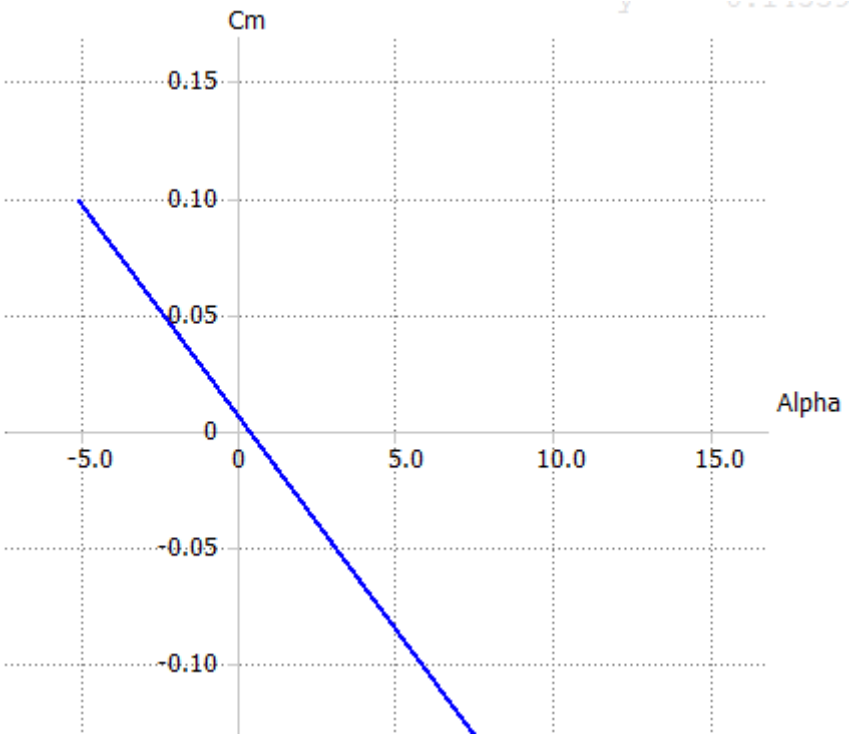

Figure 40: Moment coefficient Cm vs. AoA.

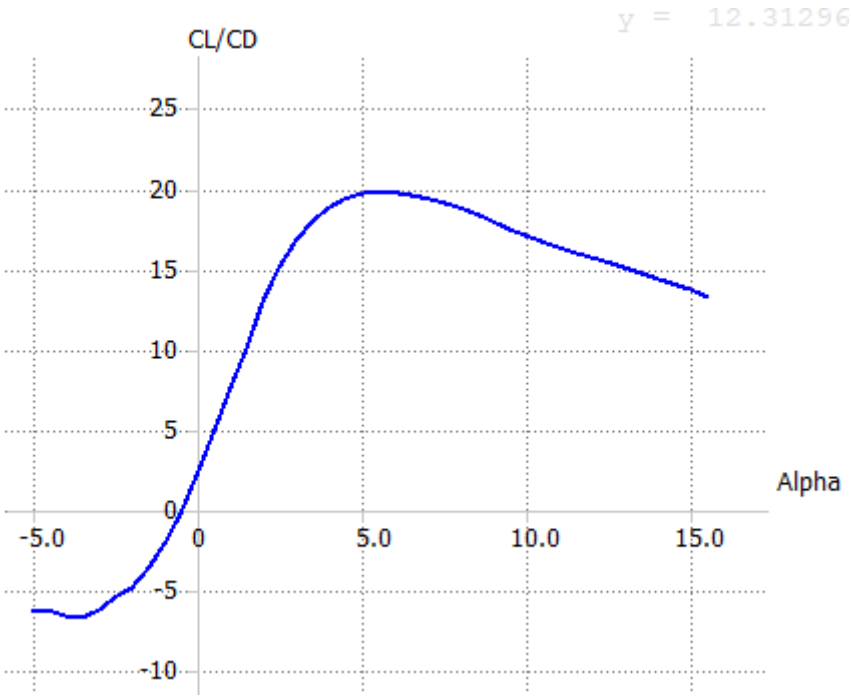

Figure 41: CL/CD vs. AoA.

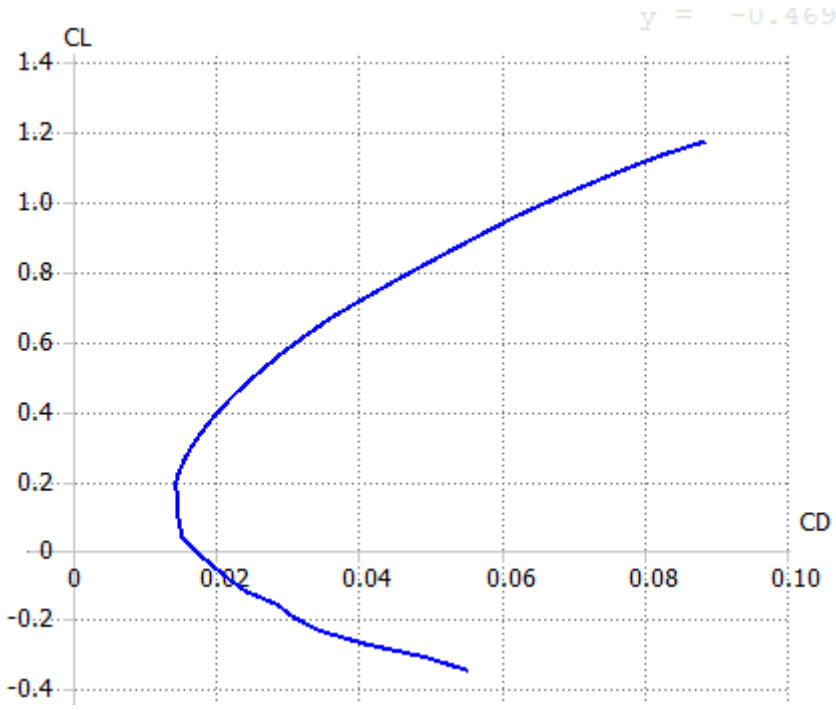

Figure 42: CL vs. CD.

- **Benefits of Reflexed Trailing-Edge**

The Eppler 636 reflexed trailing edge yields several noteworthy benefits. Firstly, it contributes to delaying flow separation at high angles of attack, reinforcing the airfoil's excellent stall behaviour and enhancing overall stability. This design feature aids in maintaining control during critical flight phases. Moreover, the reflexed trailing edge complements the positive C_{mo} characteristics, further improving the aircraft's stability and responsiveness to FC input.

4.6.1. Improvements in pitching moment characteristics

In order to improve the pitching moment of the wing, the neutral point must be determined. The neutral point, also known as the aerodynamic centre, is the point where the pitching moment is independent of the angle of attack. When the centre of gravity (C.G) is located at this point, the aircraft is neutrally stable.

Illustrated in a Cmα (pitching moment coefficient vs. AoA) plot, the neutral point is crucial for aircraft design, performance, and safety. Its position relative to the centre of gravity dictates the aircraft’s longitudinal stability: if the neutral point is ahead of the CG, the aircraft tends to be stable; if behind, it may become unstable (Chapter 4.4.).

To identify the neutral point, a point mass of 2.9 Kg is placed at a random location. By varying the C.G. values along the X-longitudinal direction, the neutral point is found to be 70 mm from the wing leading edge. This process involved starting with an Xcog of 0 mm and then adjusting towards the MAC (260 mm) through a hit-and-trial method, resulting in the neutral point value as shown below.

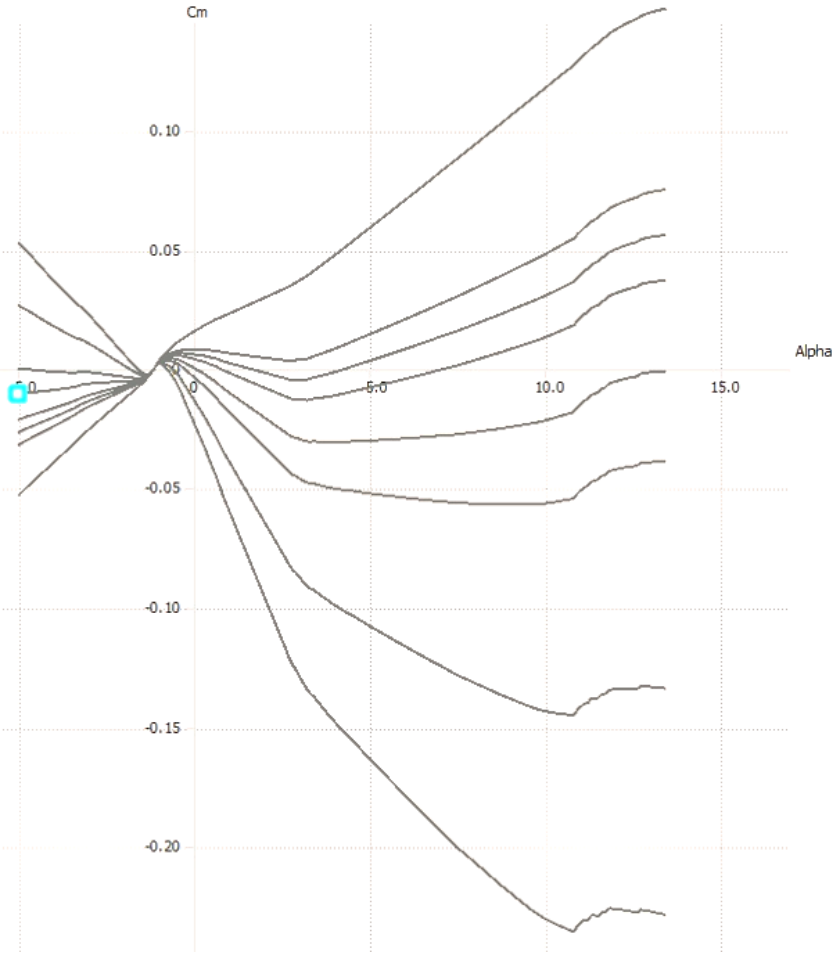

Figure 43: Cmα for the calculation of aerodynamic centre.

After determining the neutral point, it is essential to calculate the centre of gravity at different static margins, specifically 10%, 15%, and 20% [24]. These static margins indicate the distance from the C.G to the aerodynamic centre, expressed as a percentage of the MAC. The following values have been identified for the C.G:

- For a static margin of 10%, the C.G is at 44mm,
- For 15%, it is at 31mm, and
- For 20%, it is at 18mm.

The Cmα (pitching moment coefficient vs. angle of attack) graph for the Eppler 636 airfoil, with a reference C.G. position of $MAC_{c/4}$ = 89.35mm, is presented below, showing the behaviour from AoA of -4° to 4°.

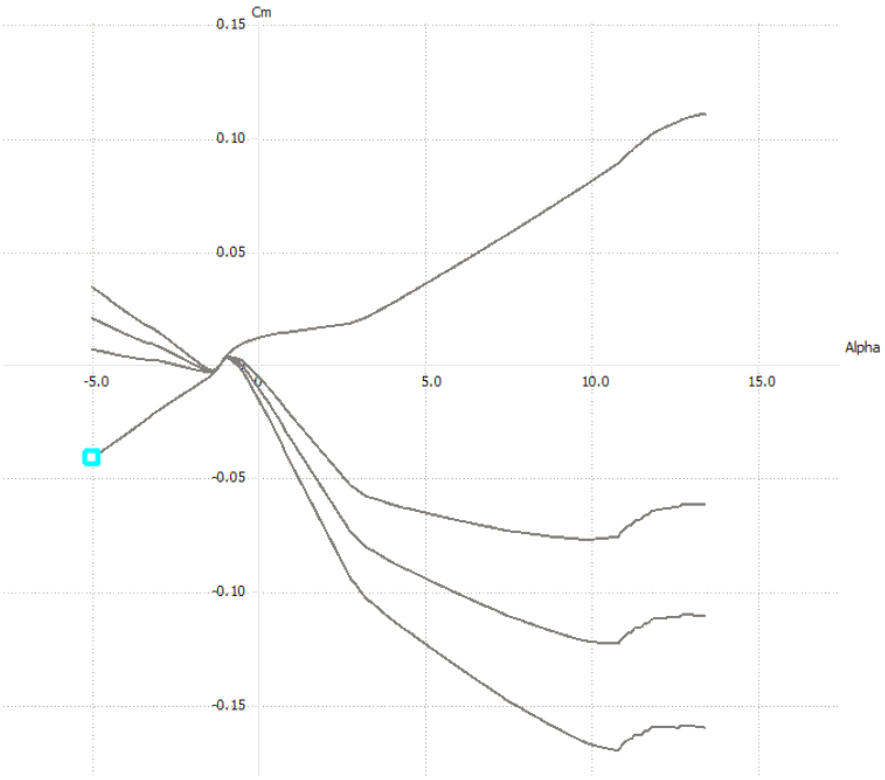

Figure 44: Cmα slope at different static margins.

- **Variation of C_{m_α} and C_{m_o} with C.G. location**

As observed in Figure 44, changing the C.G. location alters the $C_{m\alpha}$ curve. When the C.G is moved forward, the $C_{m\alpha}$ curve shifts upwards, indicating a higher nose-down pitching moment at any given angle of attack. Conversely, moving the C.G. aft shifts the $C_{m\alpha}$ curve downwards, indicating a lower nose-down pitching moment. The slope of $C_{m\alpha}$ curve also changes with C.G. position. A more positive slope indicates increased static stability, while a flatter slope suggests decreased stability. Generally, moving the C.G. forward (towards the nose) tends to increase the magnitude of C_{mo}, resulting in a more nose-down tendency. On the other hand, moving the C.G behind (towards the tail) decreases C_{mo}, resulting in a more nose-up tendency.

To further improve the stability characteristics at high AoAs, a flap with a 1° flap-up deflection is now being added at specific locations. The benefits of this addition are discussed below. It is also important to note that winglets have been added into the XFLR5 design to improve drag characteristics.

4.6.2. Addition of 1° flap-up deflection & winglets

The introduction of winglets and a 1-degree upward deflection of the flaps with carefully chosen ratios is a crucial step in optimizing the performance of the wing design. These modifications are essential for several reasons:

- Firstly, winglets play a pivotal role in reducing induced drag by mitigating wingtip vortices. Additionally, winglets positively influence the wing's vortex distribution, which has a direct impact on the wing's pitching moment characteristics. So, a dihedral of 65° is chosen as shown below.

- Secondly, the 1-degree upward deflection of the flaps strategically alters the local angle of attack, effectively increasing the airfoil's camber and lift-generation potential. The specific flap deflection angle, combined with the precise ratios of flap length to chord (33%) and flap length to span ratio (77.5%), ensures a balance between lift growth and longitudinal stability. These ratios for flaps were obtained from reference designs such as Marlyn [18] and Wingtra-one [17]. The added lift from the flaps significantly improves the Cmα curve, improving the wing's longitudinal stability, especially at higher AoAs.

Below is the table that specifies the geometry specifications of winglets and flaps.

Flaps/ Elevons	Winglets
Flap To Chord Percentage = 33% Flap To Spanwise Percentage = 77.5%	Span = 0.132 m Chord Length = 0.087 m Dihedral = 65°

Table 15: Geometry specifications of winglets and flaps.

4.6.3. Updated geometry analysis

Below are the results of the wing after adding the winglets and implementing the 1-degree elevon deflection.

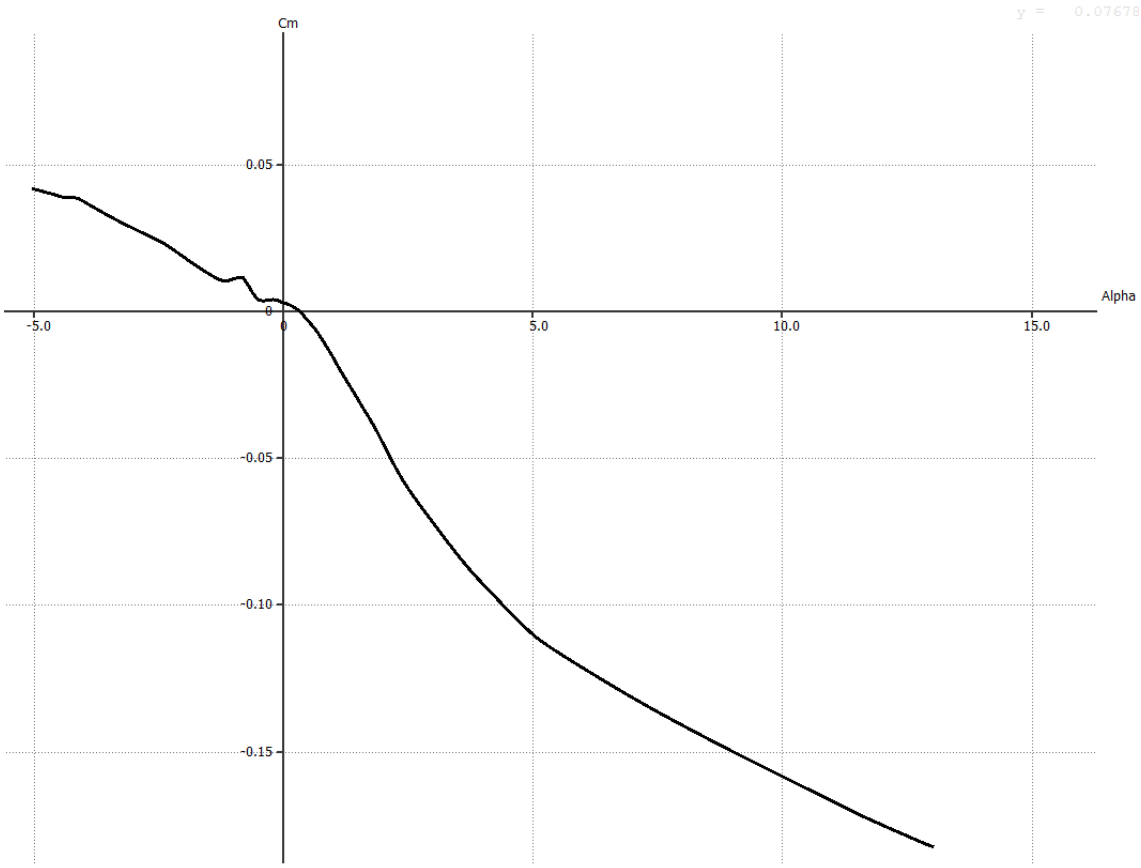

Figure 45: Cm vs. AoA of the updated wing.

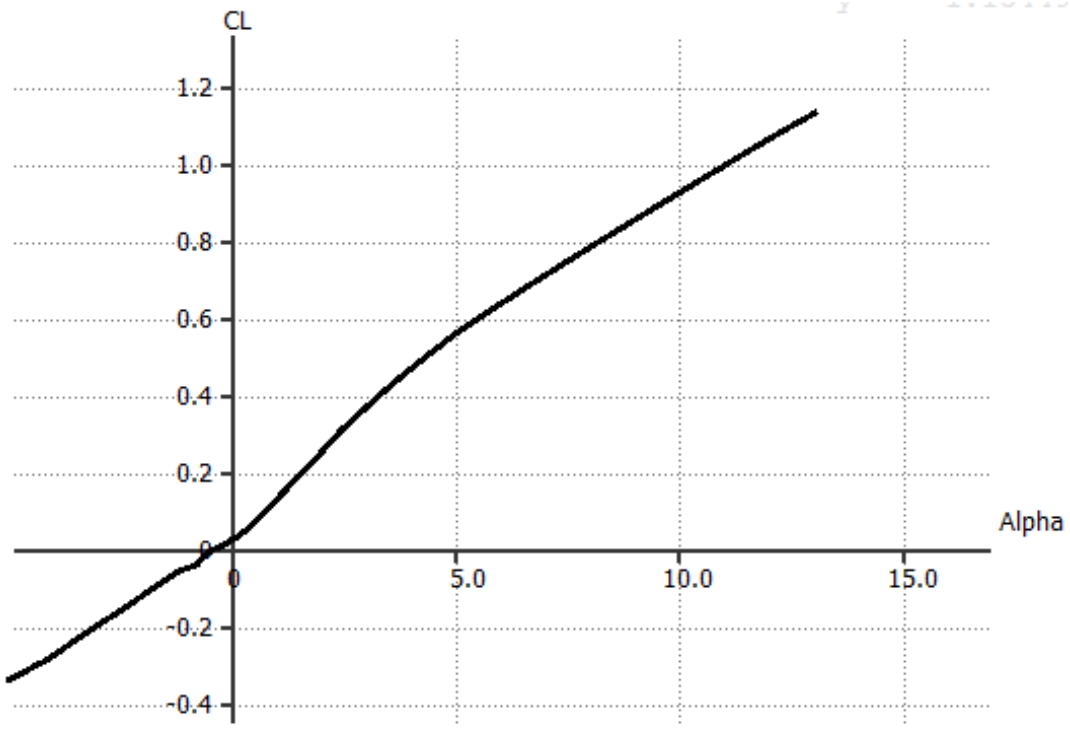

Figure 46: Lift coefficient vs. AoA of the updated wing.

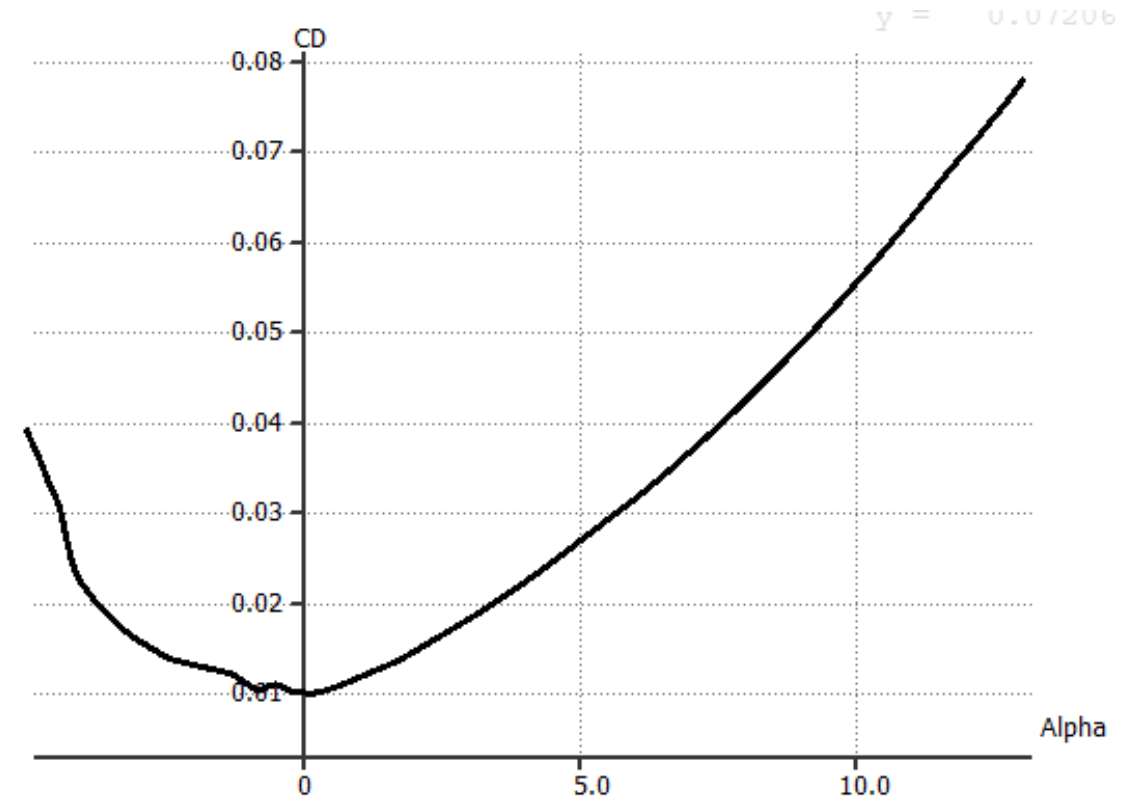

Figure 47: Drag coefficient vs. AoA of the updated wing.

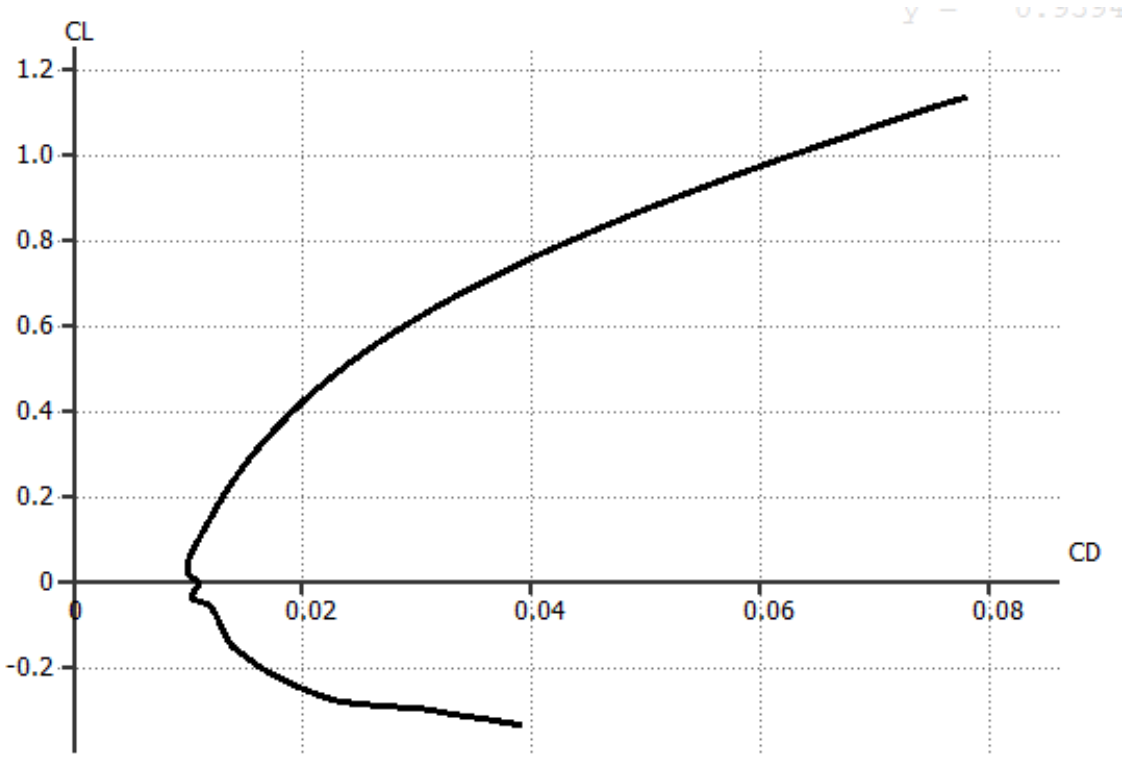

Figure 48: Lift coefficient vs. drag coefficient of the updated wing.

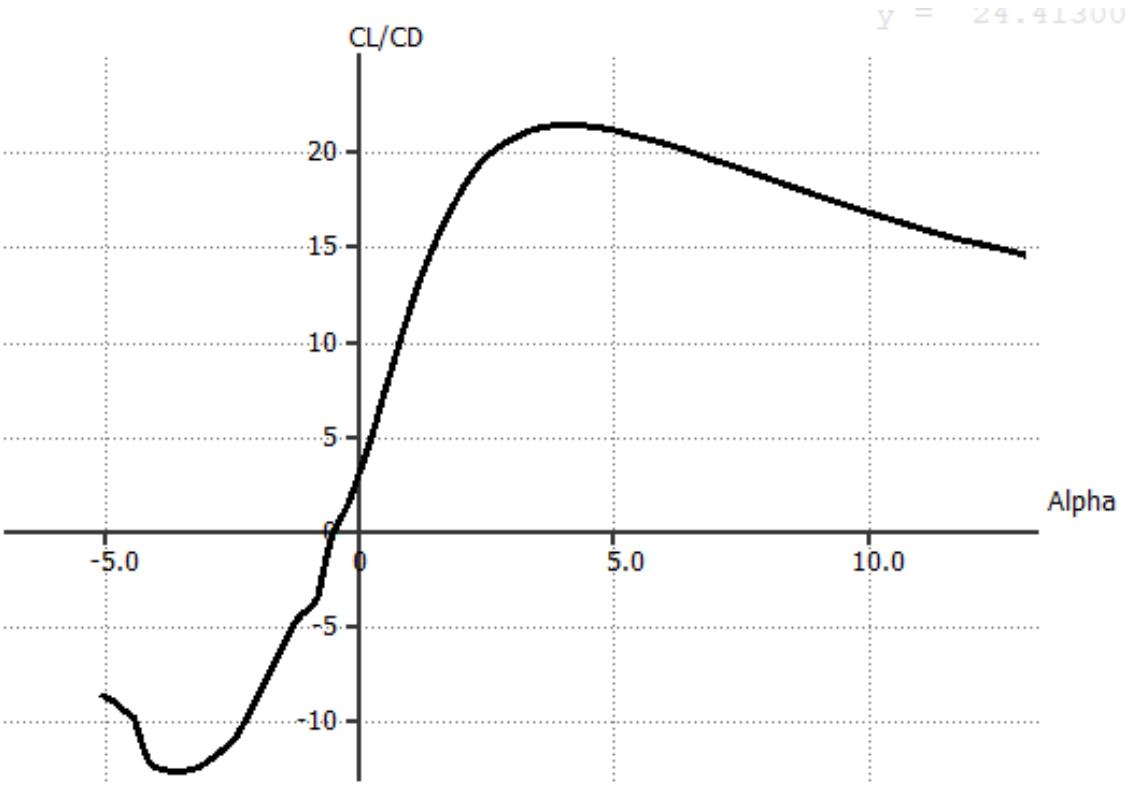

Figure 49: CL/CD vs. AoA of the updated wing.

As shown in the results above, the new implementations have significantly improved the wing's performance. The Cl now achieves a higher value around 1.1, compared to the previous maximum of 0.9. Additionally, the moment coefficient at 0º AoA is now positive, whereas it was negative before the modifications. The L/D ratio has also improved, surpassing 20, whereas it was previously around 19. Moreover, the minimum drag coefficient remains around 0.01 but, with increasing AoA, the value remains lower compared to the previous design. These enhancements indicate a substantial improvement in the wing's aerodynamic efficiency and stability, making it more capable of performing effectively across various flight conditions. The modifications have not only increased lift and stability but also minimised drag.

4.7. 3D aircraft design

For the 3D design of the aircraft, SolidWorks is used due to its user-friendly interface and robust capabilities. SolidWorks offers an intuitive design environment that allows for efficient modelling, making it ideal for complex aerodynamic shapes and intricate structural components. Its parametric design features enable quick adjustments and iterations, which are essential during the iterative design process.

4.7.1. First design

For the initial design, a simple fuselage with a constant diameter was created. This design included the elevons and incorporated the necessary electronics. During this step, it became apparent that there was insufficient space to accommodate all the components. Consequently, a second design was developed with an increased fuselage space to provide adequate room for all parts. Additionally, the nose of the fuselage was redesigned to reduce the abrupt transition, improving aerodynamics and enlightening the overall design.

Figure 50: Top view of the first VTOL design.

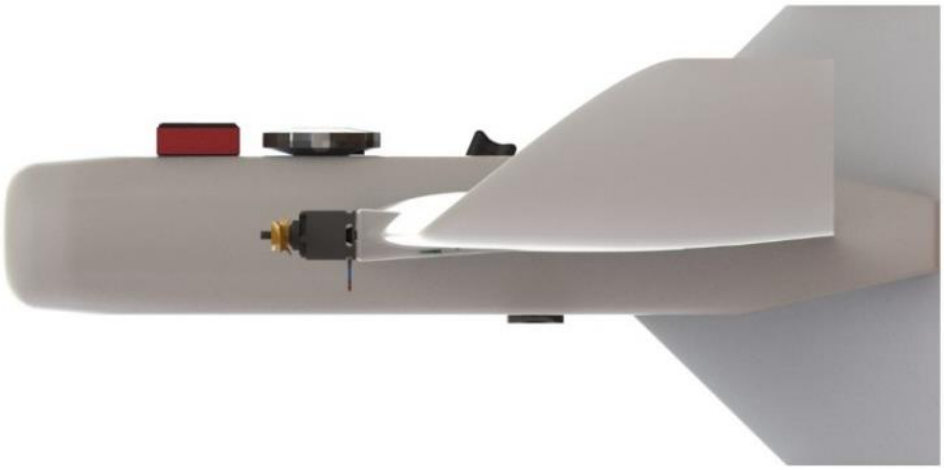

Figure 51: Side view of the first VTOL design.

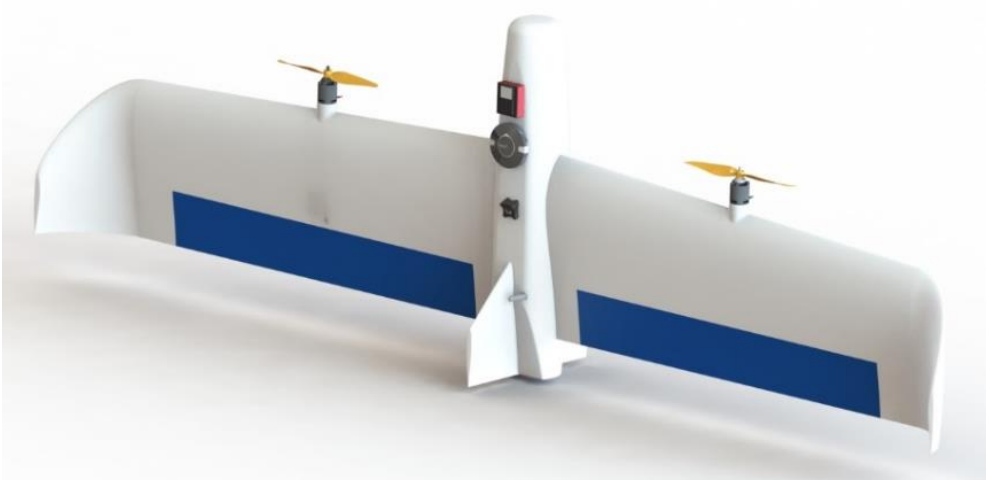

Figure 52: Isometric view of the first VTOL design.

4.7.2. Second design

Figure 53: Top view of the second VTOL design.

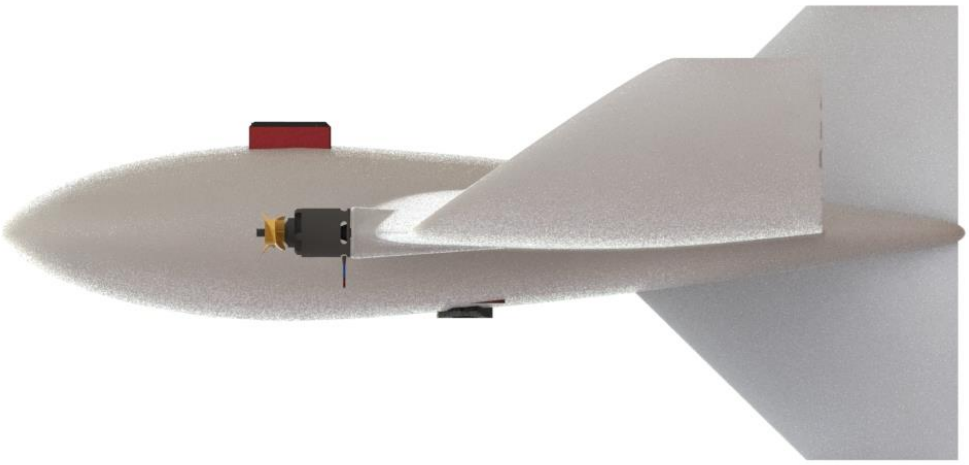

Figure 54: Side view of the second VTOL design.

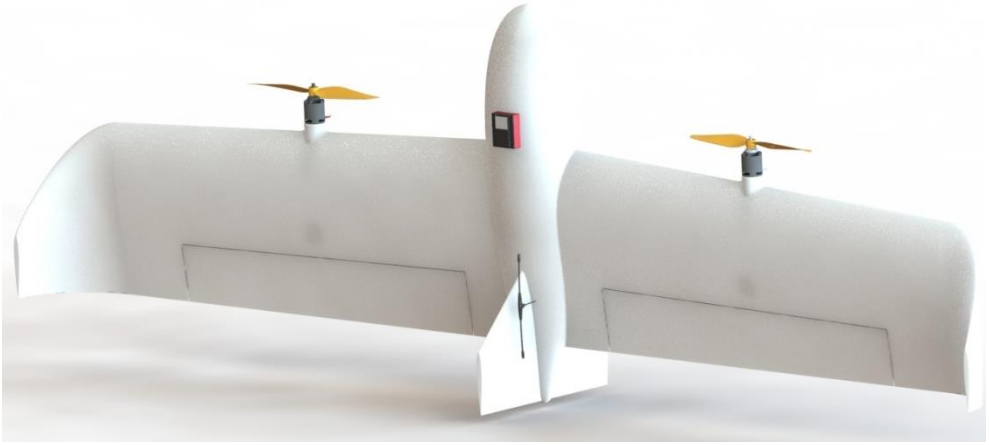

Figure 55: Isometric view of the second VTOL design.

For the second design, a more spacious and streamlined fuselage is created to accommodate all the electronics and payload. Additionally, adjustments were made to the location of the components (Figure 56 & 57) to strategically move the C.G. forward, improving the overall balance and stability of the aircraft.

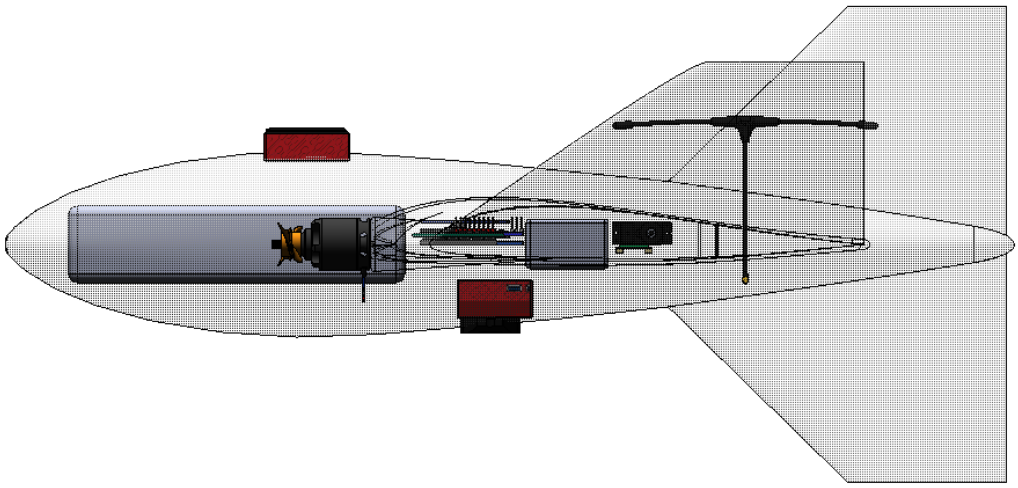

Figure 56: Translucent side view with component placement.

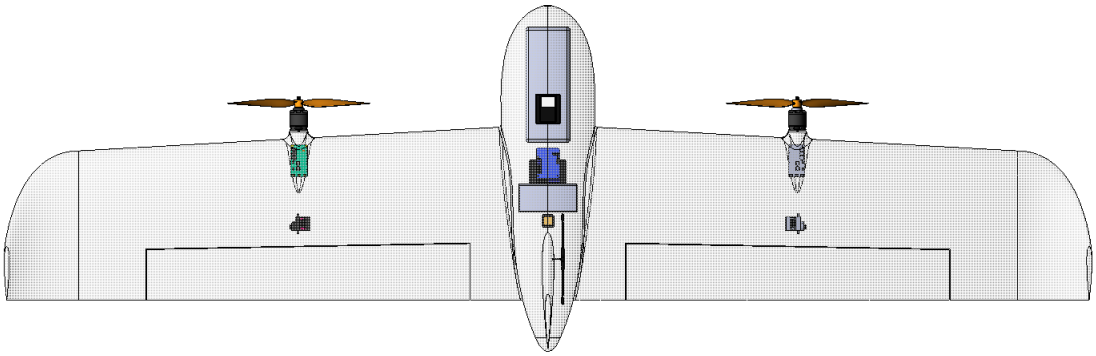

Figure 57: Translucent top view with component placement.

Chapter 5. Analysis and prototype

5.1. Stability analysis

The centre of gravity is located approximately 26 mm from the leading edge of the wing. All components within the fuselage are aligned along the x-axis, and due to the positioning requirements of the multispectral sensor, a z-value of 25 mm is also maintained. This placement ensures that the components function correctly, with the sunshine sensor positioned at the top to accurately capture sunlight and the sensor extending below to have an unobstructed view of the area beneath the UAV.

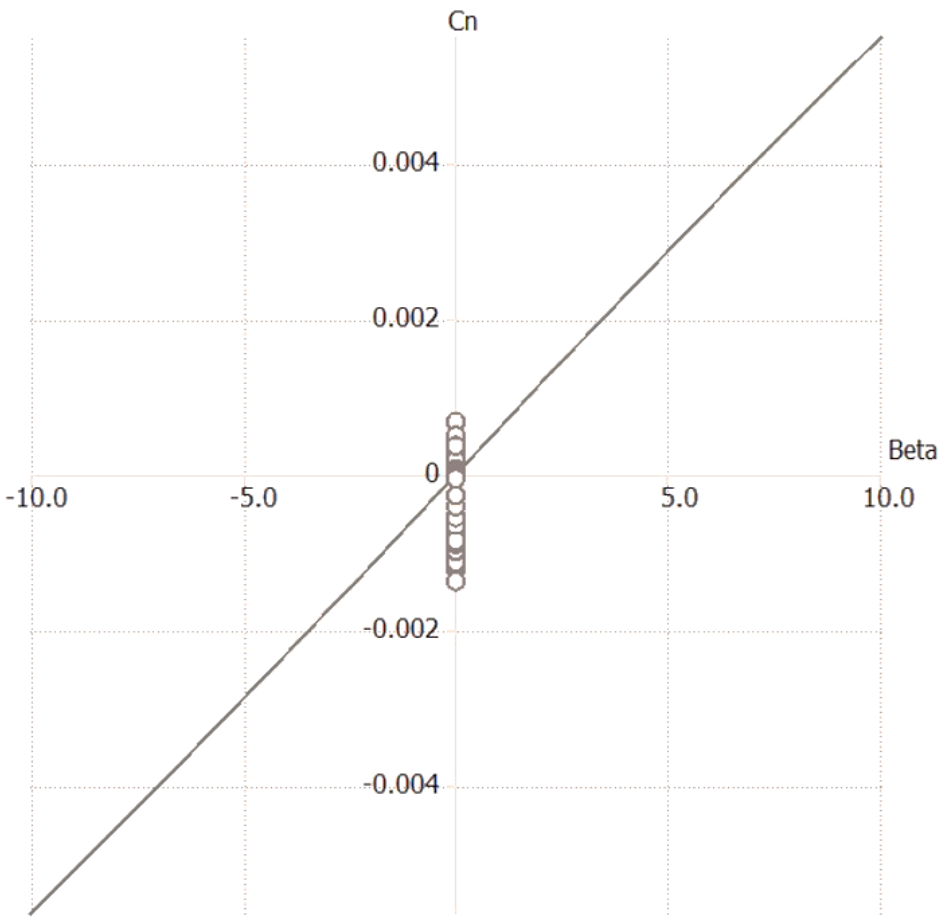

Figure 58: Yawing moment coefficient (Cn) vs. sideslip angle (Beta).

The slope of the curve $\frac{dCn}{d\beta}$ indicates the stability. A positive slope, as seen in this Figure 58, suggests that the aircraft has positive directional stability. This means that if the aircraft experiences a sideslip (angle β), it will generate a yawing moment that tends to restore the aircraft to its original flight path.

The symmetry of the curve about the origin implies that the response to positive and negative sideslip angles is similar, which is generally a desirable characteristic for stability.

The linear relationship shown by the straight line indicates that the yawing moment coefficient changes linearly with the sideslip angle within the tested range. This linear behaviour is crucial for predictable and stable handling characteristics.

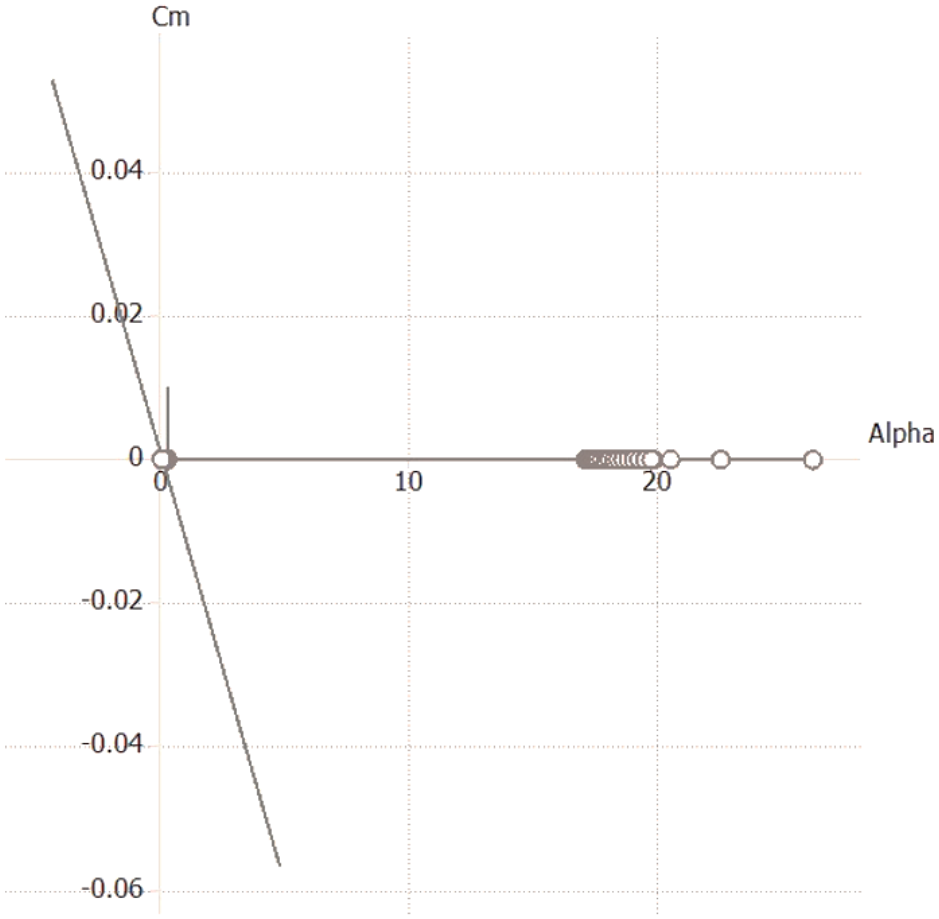

Figure 59: Pitching Moment coefficient (Cm) vs. AoA (Alpha).

The pitching moment coefficient (Cm) plotted against the angle of attack reveals insights into the aircraft's longitudinal stability. The curve's slope indicates how the pitching moment changes with the angle of attack. A negative slope, as seen here, suggests that the aircraft has positive longitudinal stability, meaning it tends to return to its original pitch angle after a disturbance. The linearity of the curve indicates predictable behaviour. Also, here the Cm curve's is symmetrical around the 0º, implying that the pitching moment's response is balanced for both positive and negative AoA, contributing to stable and controllable flight characteristics.

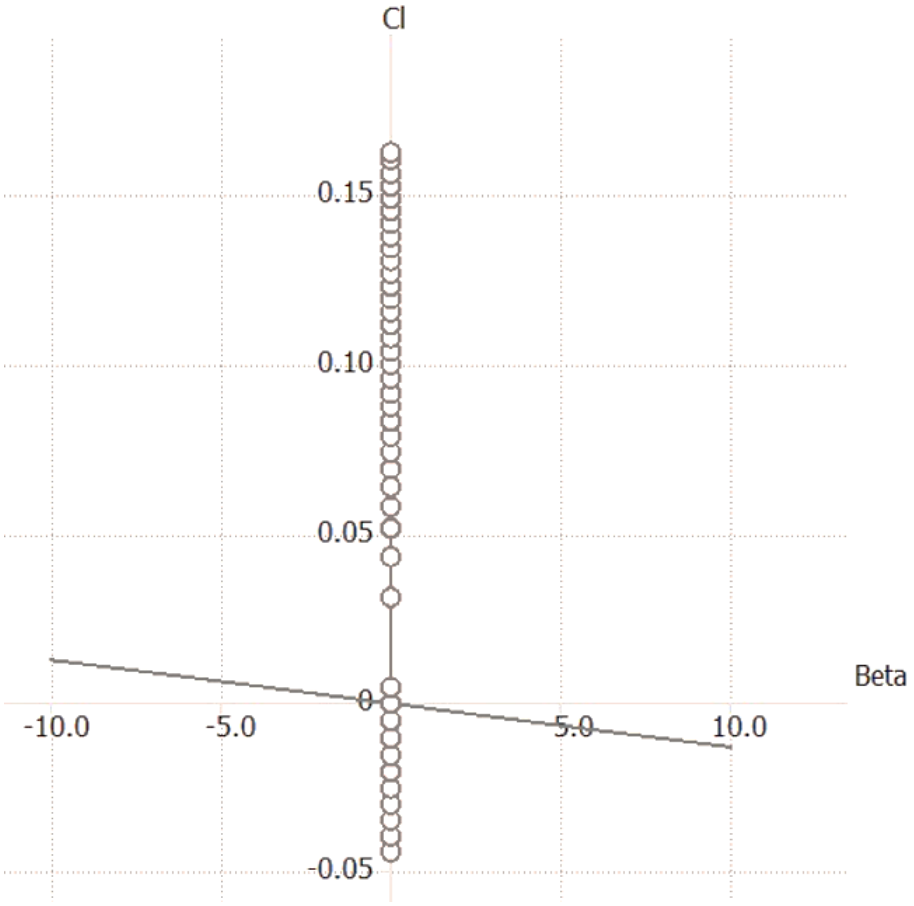

Figure 60: Rolling moment coefficient (Cl) vs. sideslip angle (Beta).

The rolling moment coefficient (Cl) in relation to the sideslip angle (Beta) provides information on the aircraft's lateral stability. The slope of the Cl curve is slightly negative, indicating negative dihedral effect, which is characteristic of lateral stability for some aircraft configurations. This means the aircraft will roll back towards a level attitude when a sideslip occurs, thereby maintaining balanced flight.

5.2. FEA analysis

For the finite element analysis (FEA) of the VTOL, an internal structure needs to be designed. To simplify calculations, the model has been streamlined to study only the fuselage, wing, and VTP. All components and winglets have been removed for this analysis. Figures 61 and 62 illustrate the internal structure, which includes a series of ribs within the wings and two hollow tubes positioned near both leading and trailing edges.

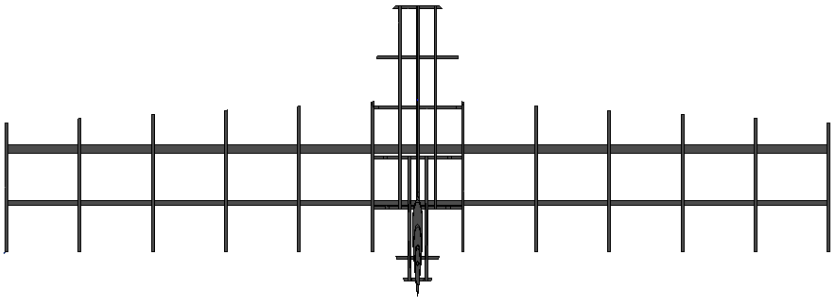

Figure 61: Top view of the internal structure of the VTOL.

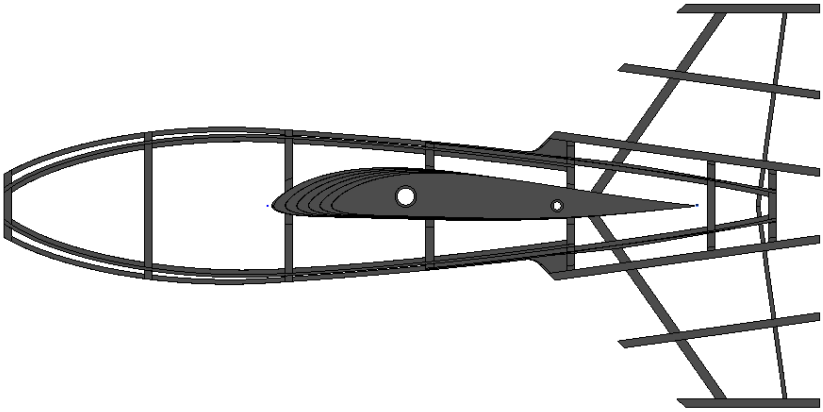

Figure 62: Side view of the internal structure of the VTOL.

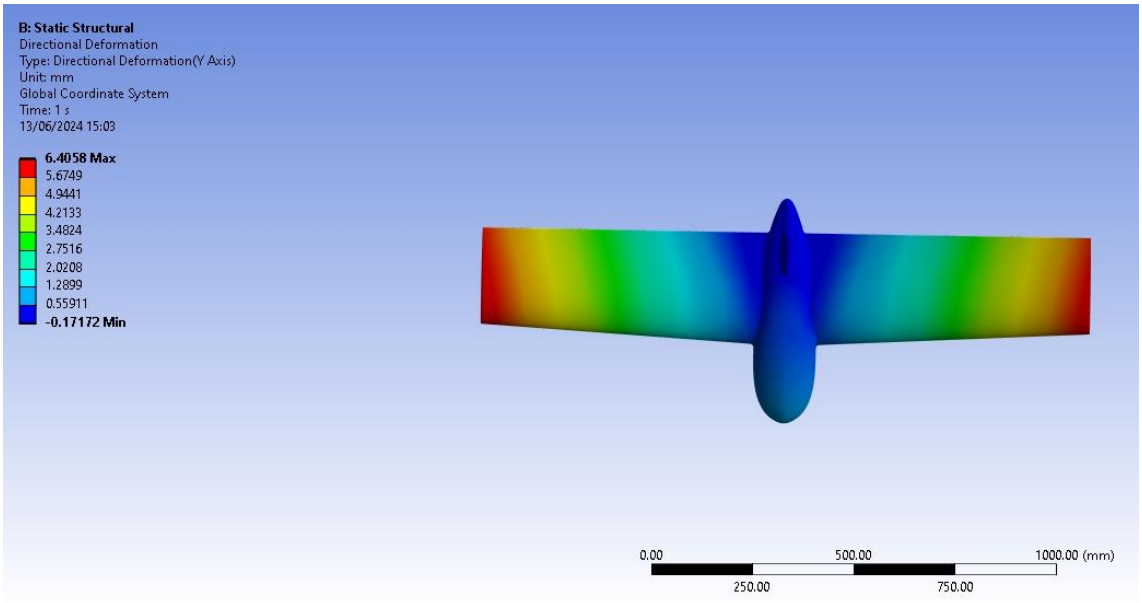

Figure 63: Static structural analysis: Y-axis direction deformation.

Figure 63 depicts the directional deformation (Y-axis) of the VTOL under load. The colour scale from red (6.0498 mm) to blue (-0.17112 mm) shows how much each part of the structure deforms. The wingtips exhibit the highest deformation, depicted in red, indicating significant flexing under load. In contrast, the central fuselage, shown in blue, experiences minimal deformation, indicating a rigid structure. This deformation analysis is crucial for ensuring that the design can withstand operational loads without excessive flexing that could impact aerodynamic performance.

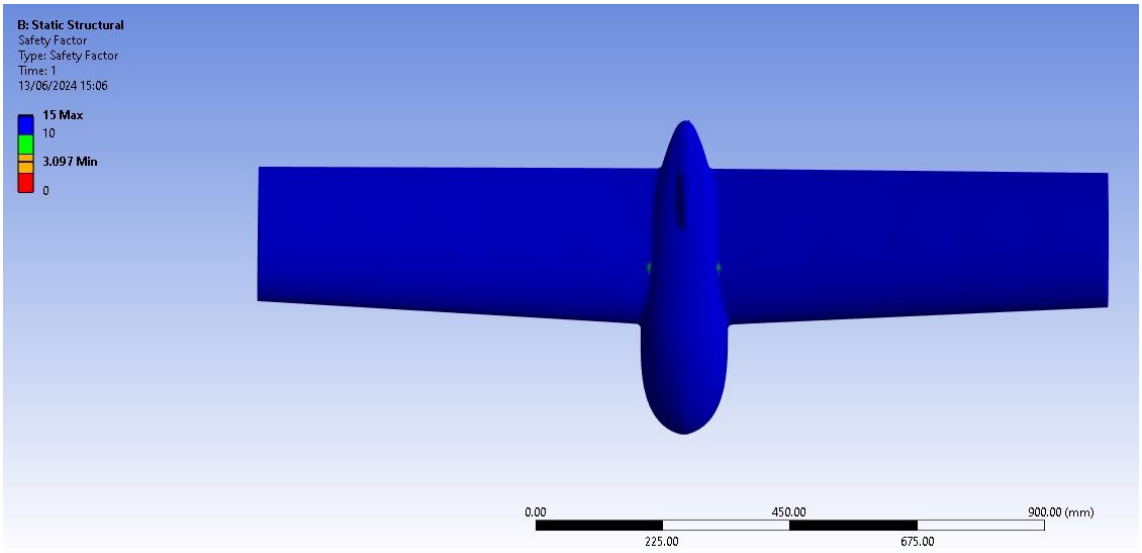

Figure 64: Static structural analysis: Safety factor.

Figure 64 illustrates the safety factor distribution across the aircraft structure under load. The colour gradient, ranging from blue to red, represents areas of varying safety margins. A high safety factor (15) indicates regions with a substantial margin before failure, primarily in blue, suggesting that most of the structure is within safe limits. However, there are small, localized regions shown in red with a safety factor closer to the minimum value (3.097), indicating potential stress concentration points that may require further reinforcement or redesign.

5.3. CFD analysis

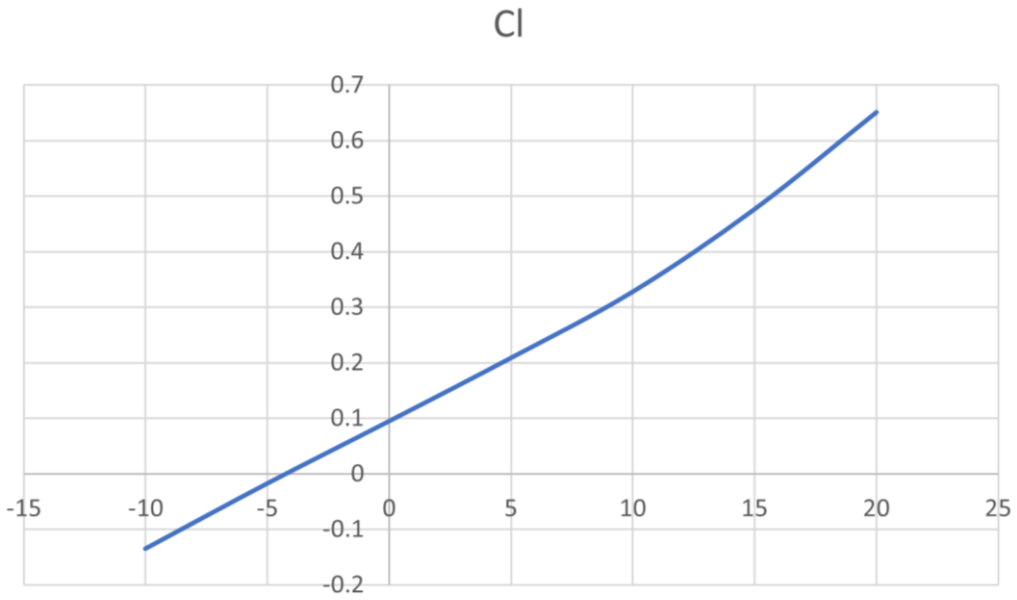

Figure 65: Lift coefficient vs. AoA given by the CFD analysis.

The C_L graph shows a steady increase with the angle of attack, starting from approximately -0.2 at AoA = -10º and reaching about 0.7 at AoA = 20º. The linear trend suggests that the wing design maintains effective lift production across a wide range of angles of attack, highlighting good aerodynamic performance, which is consistent with previous XFLR5 analysis.

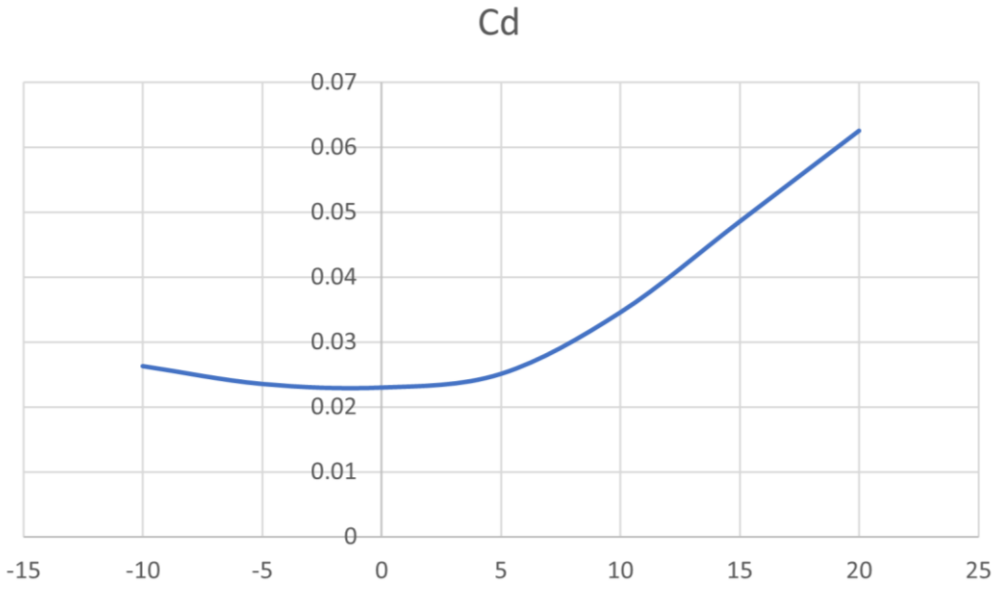

Figure 66: Drag coefficient vs. AoA given by the CFD analysis.

The C_D graph starts with a low value of around 0.028 at $\alpha = -10^o$ and shows a slight dip before gradually increasing as the angle of attack increases up to 20º. At higher AoA (α>10º), the drag coefficient rises more sharply, reaching about 0.062 at 20º.

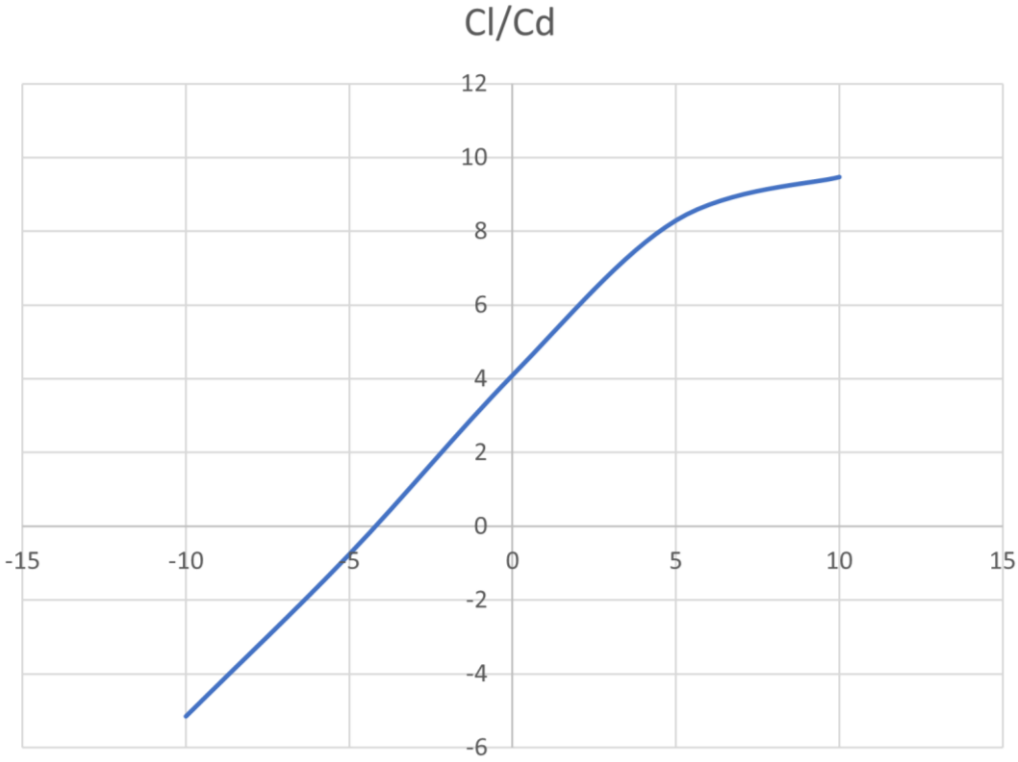

Figure 67: L/D ratio vs. AoA given by the CFD analysis.

Beyond approximately 5 degrees, the rate of increase in the C_L/C_D ratio slows down and eventually peaks around 10º. This suggests that while the wing continues to generate more lift, the associated increase in drag limits further improvements in aerodynamic efficiency.

After reaching the peak, the C_L/C_D ratio starts to level off, indicating diminishing returns in efficiency, possibly because of partial stall. This behaviour is typical as the wing approaches its critical angle of attack, where flow separation begins to occur, and induced drag increases.

5.4. 3D printed prototype

Since the prototype will be printed in LW-PLA, a material that has less resistance compared to carbon fibre or aluminium, the internal structure must be adapted to accommodate the limitations of 3D printing. A simple X-cross design with a 50º angle between lines is employed to avoid the need for supports during the printing process (Figures 68 & 69). This design modification ensures the structural integrity of the

prototype while considering the constraints and capabilities of the chosen material and manufacturing method.

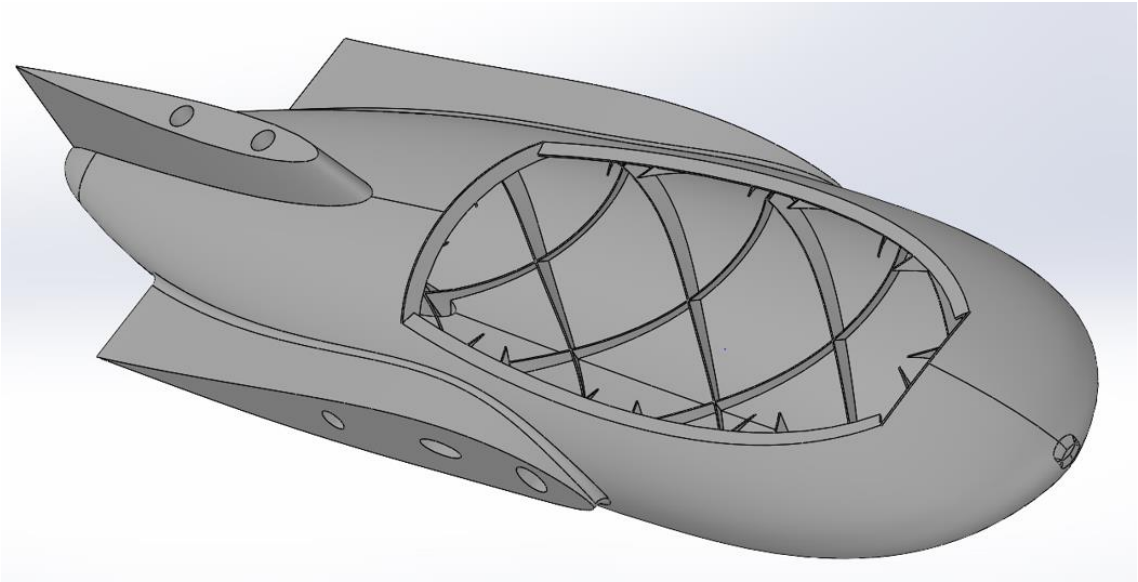

Figure 68: Fuselage inner structure for 3D printing.

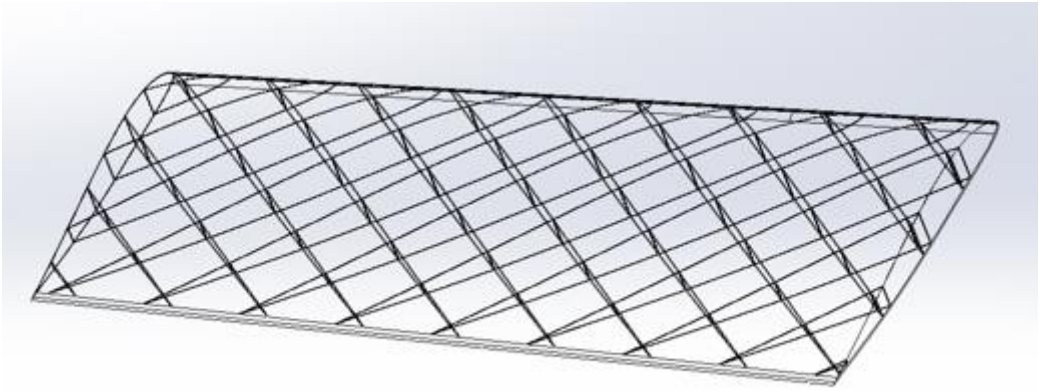

Figure 69: Left wing inner structure with its X-cross pattern.

Due to the limited printing volume of the 3D printer, the model had to be divided into 21 separate parts to fit. Moreover, the two hollow tubes indicated in the structural analysis are still employed in the prototype, as they help reduce deformation along the wings. Two carbon fiber tubes, one with a diameter of 14 mm and the other with a diameter of 10 mm, are used; the larger one is placed at the leading edge. Additionally, spaces for the servos, motor mounts, and functional ailerons have been incorporated, including hinges and mounts for the brushless motors.

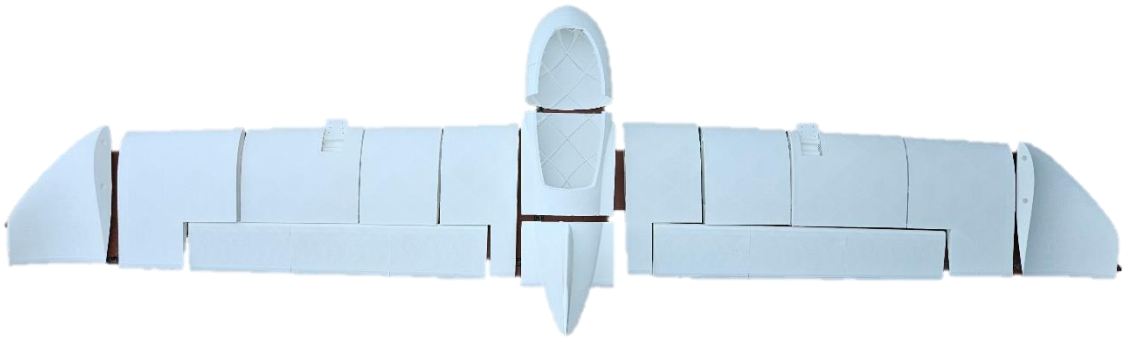

Figure 70: All 21 3D-parts of the VTOL UAV printed in white LW-PLA.

Chapter 6. Performance calculations

6.1. ECALC Calculations

Basic performance calculations are conducted using a simple, free software called ECALC [27]. This tool provides an accessible way to estimate key performance metrics of the UAV, including power requirements, flight time, and overall efficiency based on the input parameters of the aircraft's design and components. The results obtained from ECALC will serve as preliminary performance benchmarks, guiding further optimization and refinement of the UAV design.

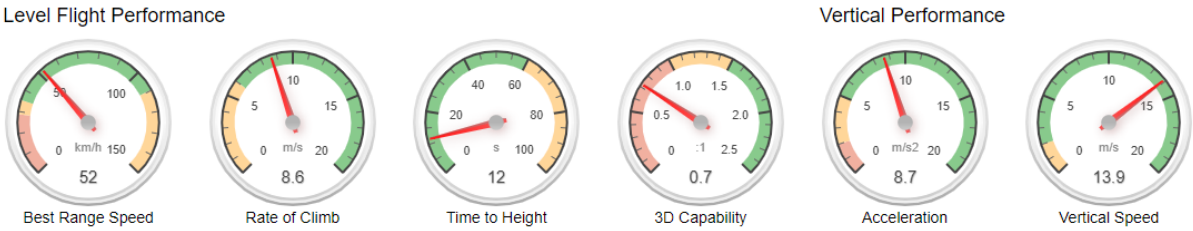

Figure 71: Data performance of VTOL given by ECALC software.

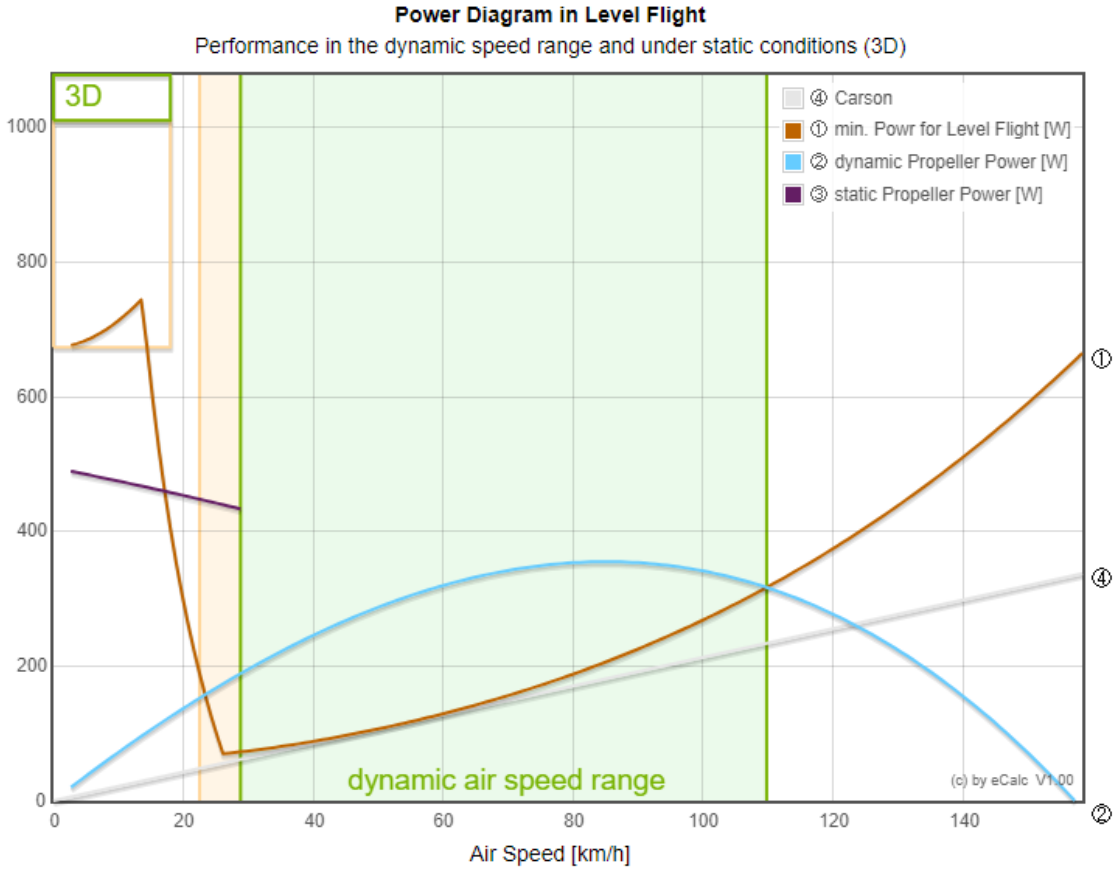

Figure 72: Power diagram vs. air speed.

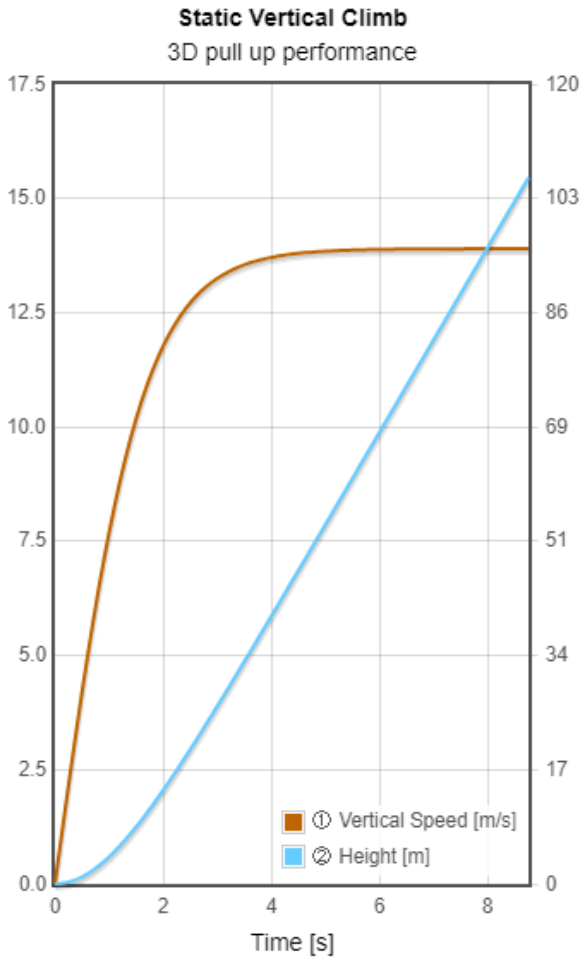

Figure 73: Static vertical climb vs. time graph.

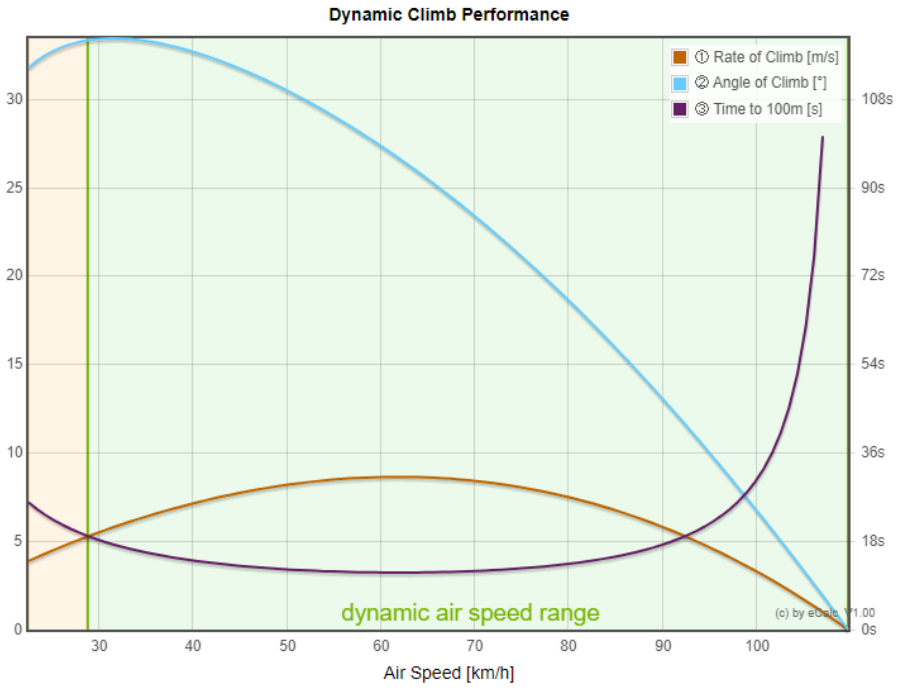

Figure 74: Dynamic climb performance graph.

Tabulated Results

Parameter	Value
Battery	4000 mAh (4S)
Motor	X2216-7 1,250Kv
Propeller	APC 8*6
Stall speed	8 - 10 m/s
Best range speed	14.5 m/s
Max speed	30 m/s
Pitch speed	34 m/s
Max propeller power	494 W
Electric Power	621 W
Max. vertical speed	13.9 m/s
Max. climb angle	33º
Max. climb rate	8.6 m/s
Time to height	12 sec.

Table 16: Results given by ECALC software.

6.2. MATLAB calculations

In the following section, MATLAB is utilized to generate crucial graphs, such as thrust required vs. velocity and aerodynamic ratios vs. velocity, among others. These visual representations are essential for understanding the UAV's performance characteristics and for making informed decisions during the design and optimization process. The graphs produced by MATLAB will provide insights into the aerodynamic efficiency, power requirements, and overall flight dynamics of the UAV.

Thrust required vs. velocity

The graph below shows that the minimum thrust required is 2.22 N at the velocity where the drag at 0º and the drag due to lift are equal.

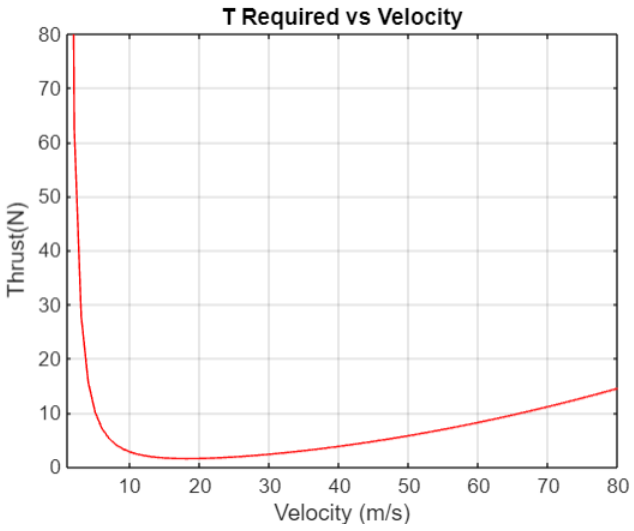

Figure 75: Thrust required vs. velocity graph.

Aerodynamic ratios vs. velocity

The provided ratios offer insights into the aircraft's flight regime. Specifically, $C_L^{3/2}/C_D$ is at its maximum, the zero-lift drag equals one-third of the drag due to lift. When C_L/C_D is at its maximum, the zero-lift drag equals the drag due to lift. Similarly, when $C_L^{1/2}/C_D$ is at its maximum, the zero-lift drag equals three times the drag due to lift.

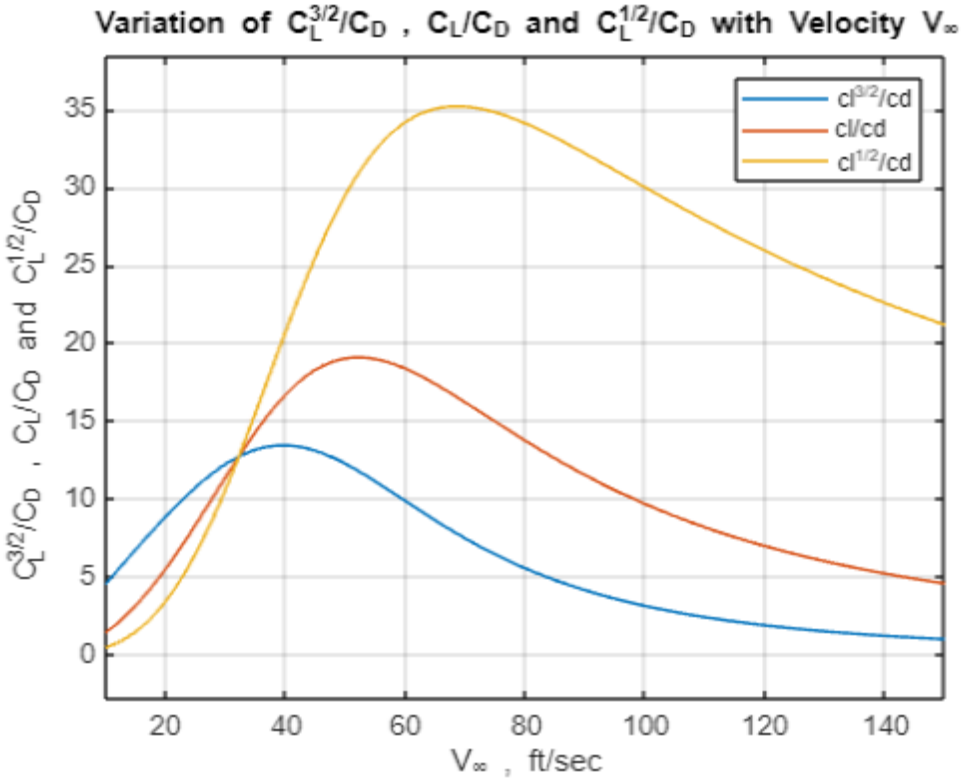

Figure 76: Variation of CL^3/2, CL/CD and CL^1/2/CD vs. velocity graph.

Power required and power available vs. velocity.

Power equals the thrust required times velocity, thus the power required is calculated and the power available obtained from electric motor data available online at 100% throttle for X2216-7 1250Kv (470 W, both motors).

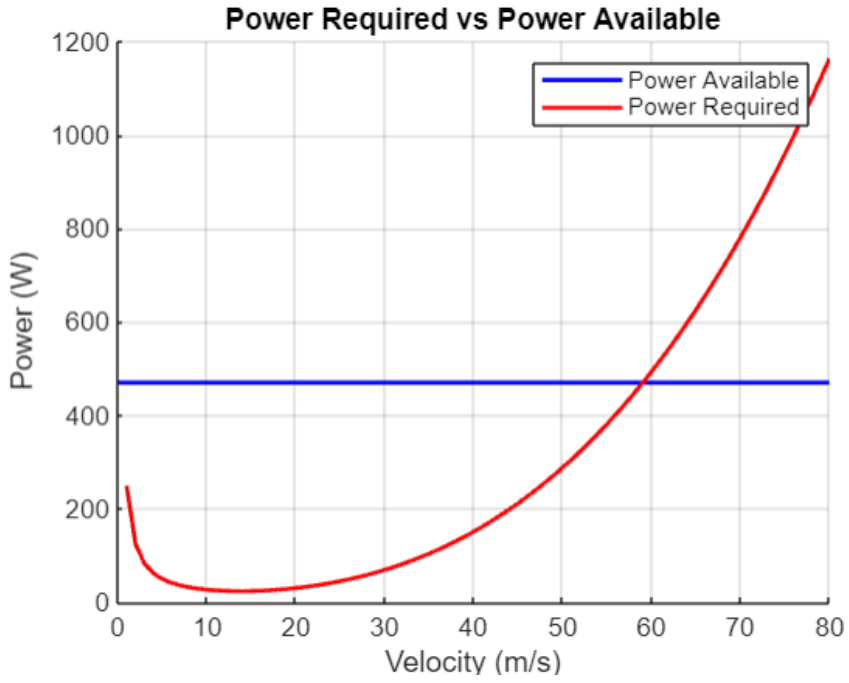

Figure 77: Power required vs. power available graph.

Rate of climb vs velocity

It is the speed at which an aircraft ascents or gains altitude per unit of time. Using the power available and power needed curves of our aircraft, we will first determine the maximum excess power. We can calculate the overall rate of ascent using this information by dividing it by W.

$$RoC = V_{\infty} sin\theta$$

$$RoC = \frac{P_A - P_R}{W} = \frac{T_A V - T_R V}{W}$$

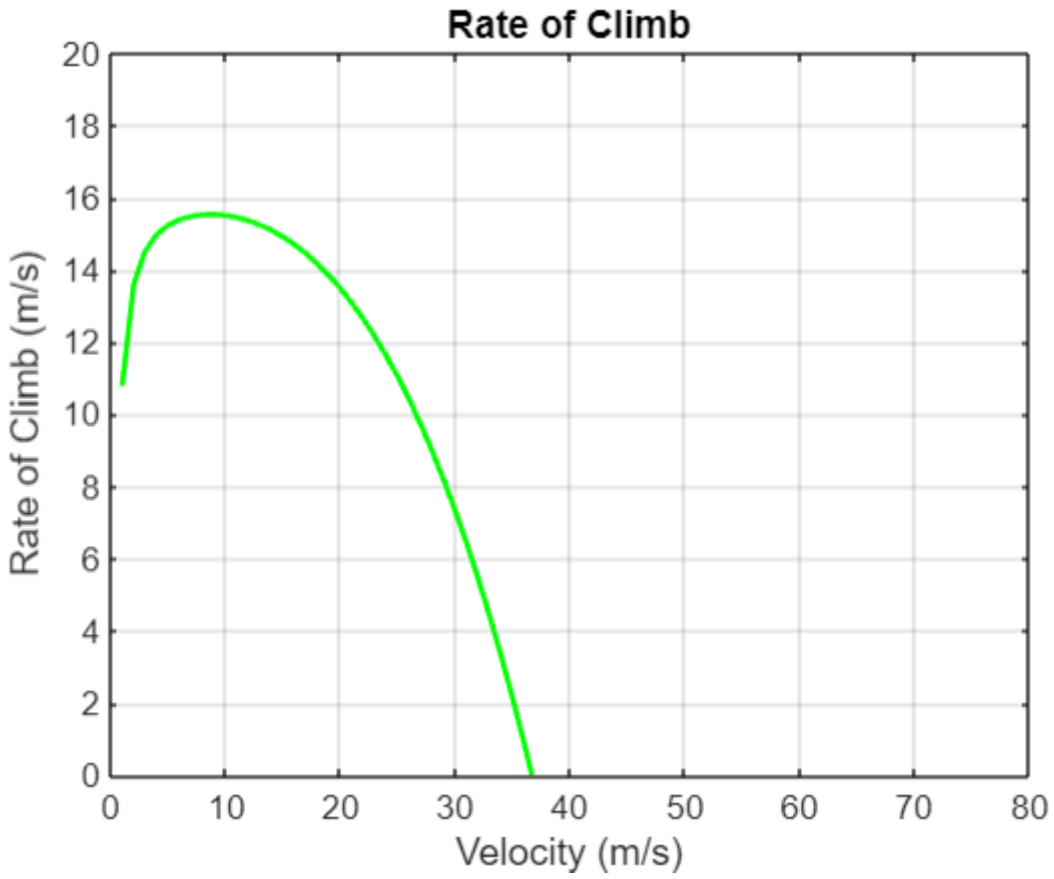

Figure 78: Rate of climb vs. velocity graph.

Hodograph

A hodograph is a diagram that shows the relationship between the horizontal and vertical components of the aircraft's airspeed. It is plotted by using the vertical component of airspeed which is the rate of climb and horizontal component of aircraft is simply calculated using the following formula,

$$V_H = \sqrt{V_\infty^2 - V_V^2}$$

The graph signifies that the aircraft has suitable glide qualities that it can achieve a minimum sink rate of 1.07 m/s at a glide velocity of 14.3 m/s without stalling.

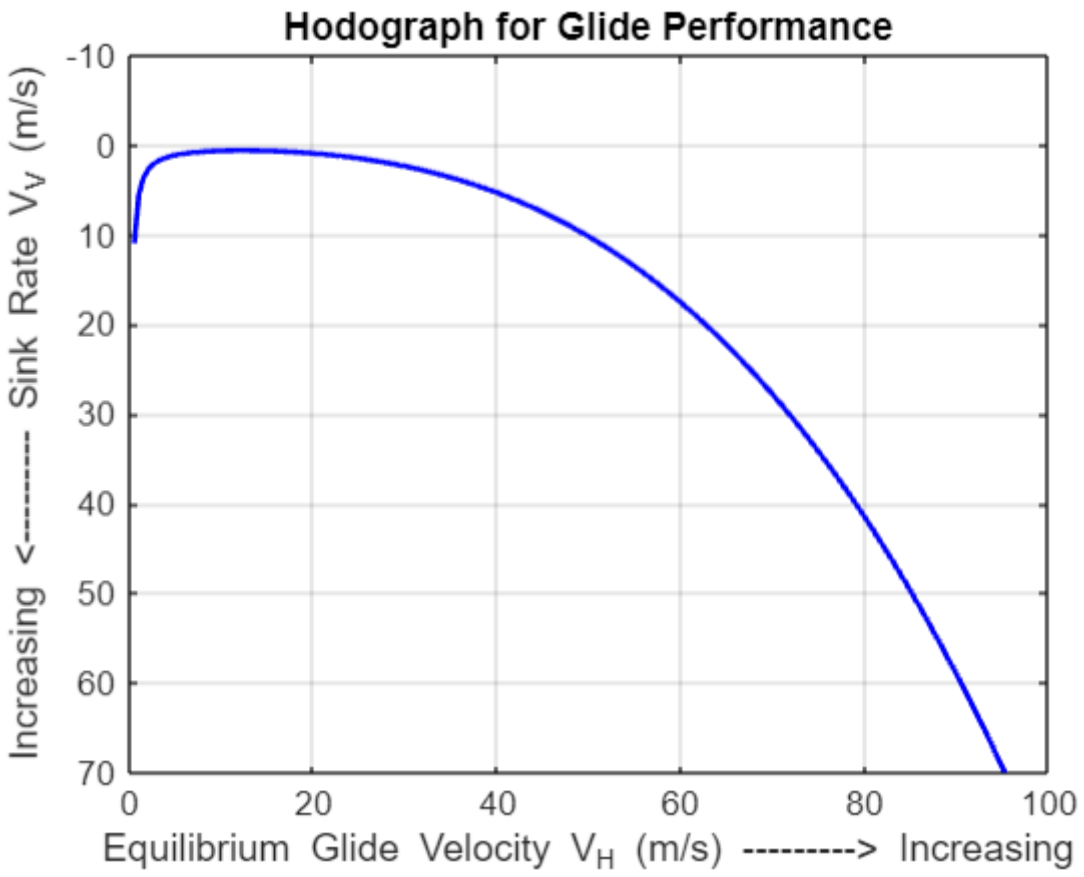

Figure 79: Sink rate vs. glide velocity.

Flight Envelope

From the graph, at the intersection of the stall and thrust constraints, which coincides with the maximum point on the curve, the load factor reaches its peak value. This peak value is referred to as the maximum positive limit load factor, or simply n_M.

$$n_M = 4.8$$

$$V_{nM} = 17.7 m/s$$

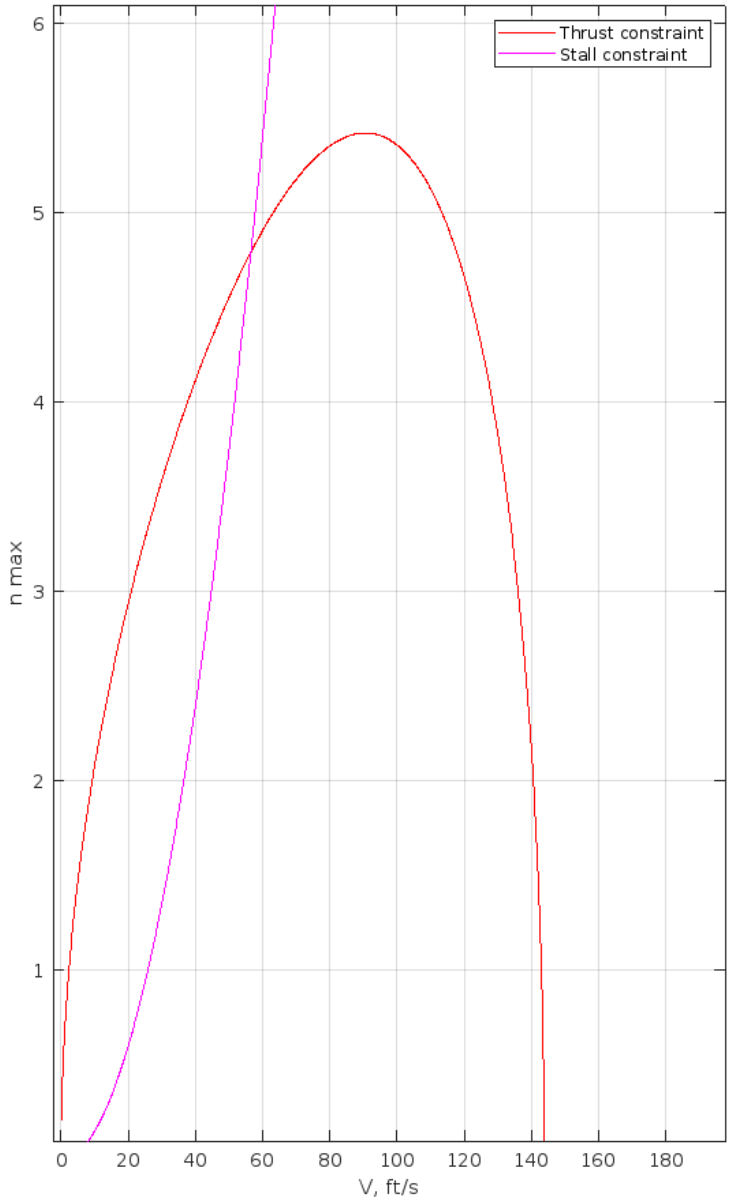

Figure 80: Flight envelope graph.

Chapter 7. Autonomous system

7.1. Flight software

ArduPilot is a complete open-source Autopilot Software Suite designed for a wide range of unmanned vehicles, including multirotor drones, fixed-wing and VTOL aircraft, helicopters, ROVs, ground rovers, boats, and submarines, among others [28].

Originally developed by hobbyists for model aircraft and rovers, ArduPilot has evolved into a robust and versatile autopilot system trusted by industries, research organizations, and enthusiasts alike. The suite encompasses navigation software running on the vehicle, such as Copter, Plane, Rover, or Sub, along with ground station controlling software like Mission Planner, APM Planner, QGroundControl, and Tower [28].

ArduPilot offers an extensive array of functionalities shared across all vehicle types, encompassing fully autonomous, semi-autonomous, and manual flight modes, along with programmable missions featuring 3D waypoints and optional geofencing. It includes stabilization options that obviate the need for external co-pilots, as well as simulation capabilities with various simulators such as ArduPilot SITL. Moreover, it supports a wide range of navigation sensors, including multiple models of RTK GPSs, traditional L1 GPSs, barometers, magnetometers, laser and sonar rangefinders, optical flow sensors, ADS-B transponders, infrared sensors, airspeed indicators, and computer vision/motion capture devices [28].

7.2. Updating the firmware

Given that the flight controller may have been manufactured some time ago, it is likely that newer firmware versions are available, and an update is necessary to access all capabilities. The firmware version should be the latest stable release, as early release firmware tends to have bugs and oversights.

All available firmware can be obtained directly from the ArduPilot website, which is organized into different subdivisions such as plane, copter, rover, and sub. For VTOL, the “Plane” section is selected. After choosing the "Stable" option, a list of all supported flight controllers appears. For the VTOL, the Matek F405 model is used, listed as MatekF405-TE. The required file, arduplane_with_bl.hex, is downloaded and saved on the computer.

To upload the .hex file into the FC, a control software is required. The INAV configurator will be used, although other software like *Betaflight* can also operate

effectively. Occasionally, updating the drivers of the FC may be necessary to enable proper communication between the flight controller and the computer. In such cases, *Zadig*, a straightforward software designed for installing generic USB drivers can be employed. In order to flash the driver, the FC needs to be connected to the computer using a data-transfer USB cable. Afterwards, the “STM32 BOOTLOADER” is selected as the device and “WinUSB” as the driver to upload. Finally, the “Replace Driver” button is clicked to start the flashing process.

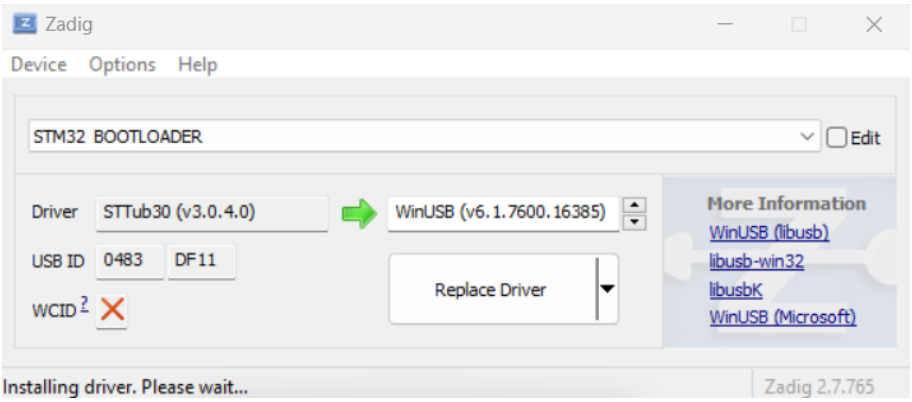

Figure 81: Zadig software main window.

Once the driver is updated, the INAV configurator is launched. Before connecting the FC to the computer, the DFU button on the flight controller must be pressed and held. If done correctly, the word "DFU" appears in the upper right corner of the configurator as shown in figure 82. Within the "FIRMWARE FLASHER" tab, the "LOAD FIRMWARE (LOCAL)" button is located and clicked, opening the document browser. The previously downloaded .hex file is selected. Subsequently, the "FLASH FIRMWARE" option lights up in blue, allowing the file to be incorporated into the FC.

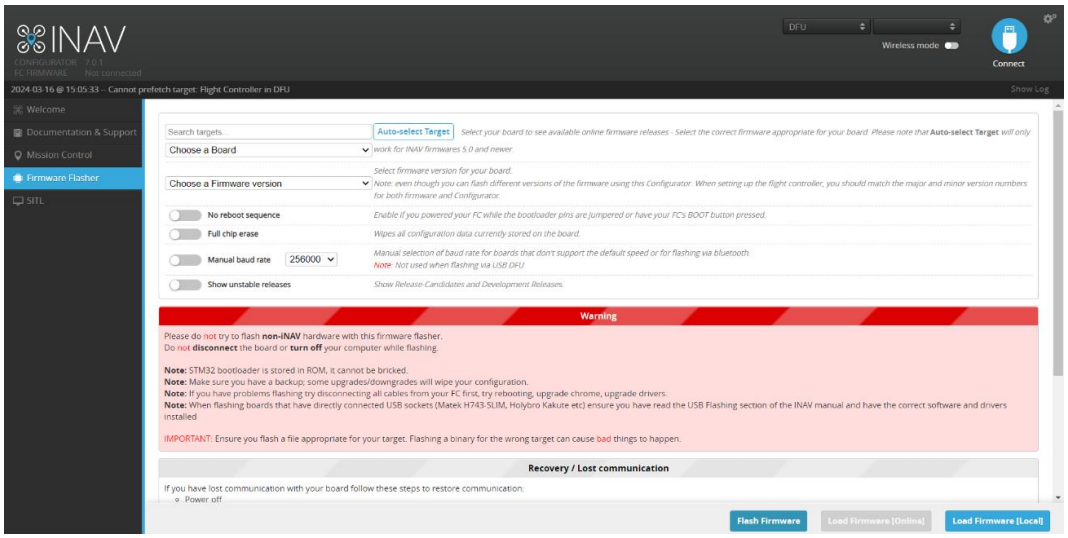

Figure 82: INAV main window.

7.3. Calibration of the FC

Before soldering any wires into the FC, it is recommended to connect it to Mission Planner to verify proper functionality. For this purpose, the FC is connected to the computer and the Mission Planner software is launched. Within the *SETUP* tab, the accel calibration option will be visible.

Figure 83: Mission Planner software: Accel Calibration tab.

Following the software instructions, which involve positioning the FC in various orientations (nose up, nose down, left, right, back, and level), will calibrate the sensor. After completing the calibration, it can be verified using the artificial horizon provided in the *DATA* tab. Moving the FC in different orientations should correspondingly move the horizon, indicating proper calibration.

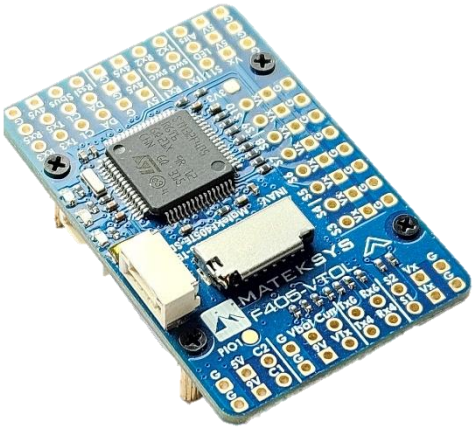

Figure 84: FC at level orientation (0º).

Figure 85: Artificial horizon showing level orientation.

Figure 86: FC tilted 90º to the left.

Figure 87: Artificial horizon showing 90º left tilt.

As seen in Figure 84, the orientation of the FC corresponds to the one shown in Figure 85, which is the artificial horizon displayed by the Mission Planner software. Similarly, for the FC tilted 90º to the left, Figure 87 illustrates the tilted orientation accurately. Once the flight controller is verified to run correctly, the process of soldering all the components can begin.

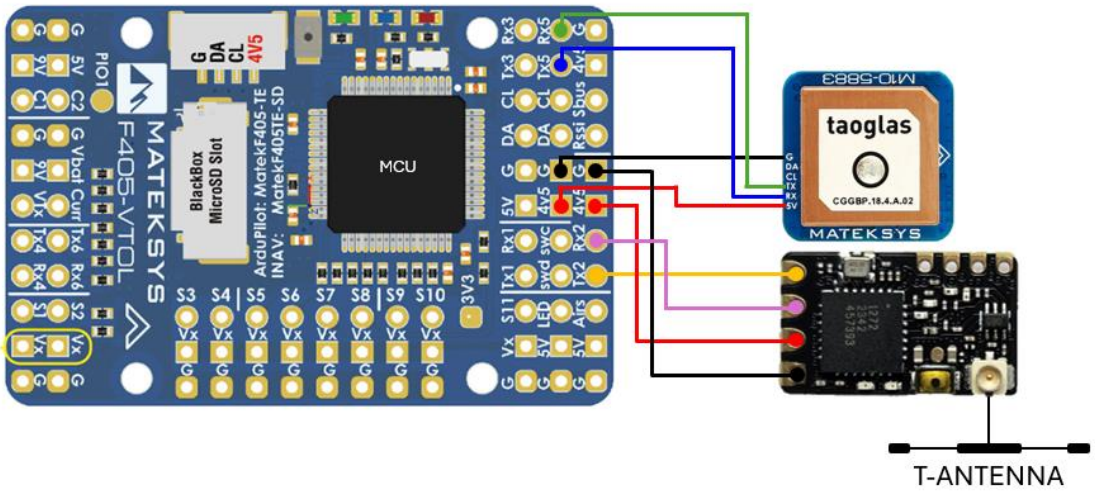

Figure 88: FC schematics, connection of GPS and RX.

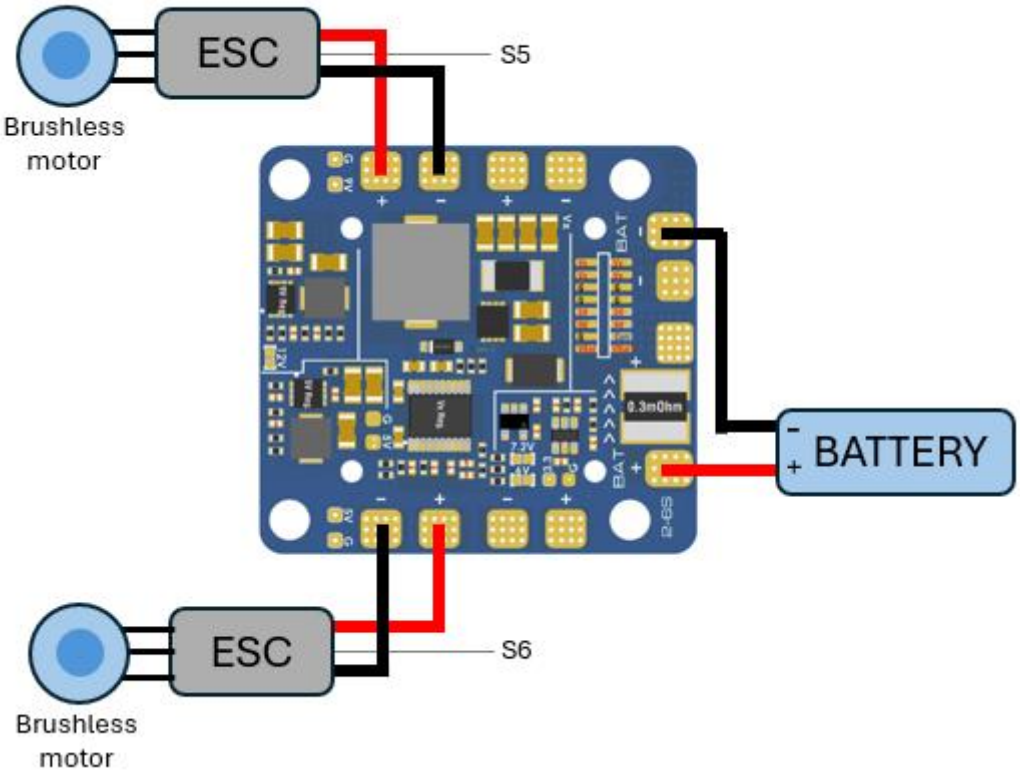

Figure 89:PDB schematics: connection of the battery and both motors.

7.4. Creating the autonomous system

- **Configuring flight modes:**

The “Flight Modes” tab is set to include “AUTO” mode for autonomous flight operations. This configuration allows the VTOL to switch to autonomous navigation once the flight plan is initiated.

- **Planning the Flight**

Afterwards, the tab is changed to the “Flight Plan” section at the top of Mission Planner. This section allows for detailed planning and visualization of the flight path over the plantation. First step in very plan is to set the home location by right clicking the location desired. This location will serve as take-off and landing for the VTOL. It is important to choose a safe and accessible area for this purpose.

To ensure thorough coverage of the plantation area, waypoints forming a grid pattern are added by right-clicking on the map. The altitude for each waypoint is adjusted to maintain a consistent flight height above the plantation, optimizing for data collection and safety.

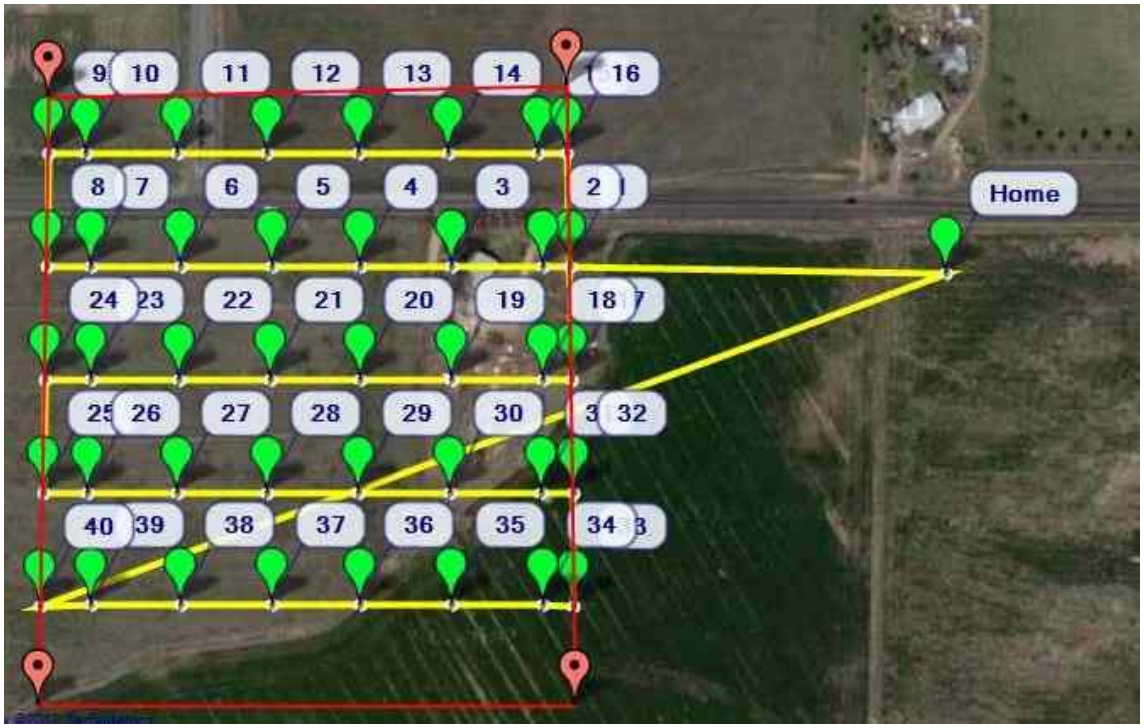

Figure 90: Flight plan grid with all the waypoints and home point.

Waypoints for VTOL transitions, such as switching from vertical to horizontal flight, are also included.

The last waypoint is set to return the VTOL to the home location or a designated landing area using the “RTL” command, ensuring a safe and controlled landing of the aircraft.

Uploading the flight plan

All waypoints and commands are carefully reviewed to ensure they are correctly configured and logical. This step is crucial for avoiding any in-flight errors or unexpected behaviours. Once checked, the “Write WPs” button is clicked to upload the flight plan to the VTOL’ FC. This transfers all the waypoints’ locations and actions to the onboard flight controller, preparing the VTOL for the mission.

Pre-flight checks

- Battery check (ensure it is fully charged and properly connected).
- GPS lock (GPS is verified to have a strong lock).
- Control surfaces check (control surfaces are tested to ensure they respond correctly).
- Failsafe settings (low battery return, signal loss return).

Executing the flight

The VTOL is armed using the transmitter switch provided for it. Once both motors spin and stay at constants rpm, the flight mode is switched to “AUTO” to start the autonomous mission. The VTOL will begin following the uploaded flight plan.

Post-flight analysis

After the flight, the data files from the sensor are downloaded for detailed analysis of the flight performance and data collection. These monochrome images are reviewed to assess the plantation health, identifying any issues or areas for improvement. This analysis will help the farmer to identify the unhealthy plants.

Chapter 8. Conclusions and future work

The design and development of the VTOL tail-sitter UAV for precision crop health monitoring has demonstrated significant potential in enhancing agricultural productivity and sustainability. Through meticulous design processes, including airfoil selection, aerodynamic analysis, and structural integrity assessments, the UAV has been optimized to meet specific mission requirements. The use of reflexed cambered airfoils like the Eppler 636 has been crucial in achieving the desired stability and performance characteristics without a horizontal stabilizer. Additionally, the integration of advanced multispectral imaging capabilities will enable detailed monitoring of crop health, providing farmers with actionable insights for better resource management.

The iterative design process, supported by tools like XFLR5 for aerodynamic analysis and SolidWorks for 3D modelling, has ensured that the UAV meets the necessary criteria for efficient and reliable operation. Initial flight simulations and performance calculations indicate that the UAV can achieve the targeted cruise speeds and flight durations, essential for covering large agricultural areas with high-resolution imaging. The stability and control characteristics, particularly in varying flight conditions, have been validated through extensive computational analyses.

Additionally, the LW-PLA prototype print has been successful. The initial prototype will undergo flight testing to validate the theoretical predictions and identify any discrepancies or areas for improvement. These flight tests will provide critical data on the UAV's performance in real-world conditions, allowing for fine-tuning of control algorithms and hardware adjustments to enhance stability and efficiency.

Additionally, the construction of the UAV using lightweight and durable materials such as carbon fibre will be prioritized. The current design utilizes LW-PLA, which is not ideally suited for high-stress environments and gusty conditions. Carbon fibre will not only reduce the overall weight of the UAV but also improve its structural integrity and resilience to external factors. This material transition will be accompanied by rigorous testing to ensure that the UAV maintains its aerodynamic properties and operational capabilities.

Moreover, the implementation of advanced features such as real-time data transmission will be explored. Enhancing the UAV's ability to process and transmit data during flight will provide immediate insights to farmers, further increasing the utility of the system. Integration with existing agricultural management systems will also be considered to streamline the workflow and maximize the benefits of precision agriculture technologies.

In summary, the future work will be centred around optimizing the UAV's design based on flight test feedback, improving its structural and operational robustness.

Chapter 9. Bibliography

[1] “United Nations,” [Online]. Available: https://www.un.org/en/global-issues/population. [Accessed 11 03 2024].

[2] J. Bruinsma, “FAO,” fao.org, [Online]. Available: https://www.fao.org/3/i2280e/i2280e06.pdf. [Accessed 11 03 2024].

[3] Food and Agriculture Organization of the United Nations, “fao.org,” 2017. [Online]. Available: https://www.fao.org/3/i7959e/i7959e.pdf. [Accessed 19 03 2024].

[4] Airelectronics, “Airelectronics: UAV AUTOPILOTS,” [Online]. Available: https://www.airelectronics.es/products/solutions/x8/. [Accessed 23 03 2024].

[5] Fly Dragon Drone Tech., “Fly Dragon: X drone,” [Online]. Available: https://www.dronefromchina.com/product/fixed-wing-hybrid-vtol-210-mins-endurance.html. [Accessed 23 03 2024].

[6] c. s. Tasupalli, “LinkedIn,” 22 12 2019. [Online]. Available: https://www.linkedin.com/pulse/how-make-drone-uav-lesson-2-frame-chandra-shekhar-tasupalli-/. [Accessed 16 06 2024].

[7] MATEKSYS, “Matek Systems,” [Online]. Available: https://www.mateksys.com/?portfolio=f405-vtol#tab-id-2. [Accessed 6 4 2024].

[8] K. Borade, “Medium,” 26 5 2023. [Online]. Available: https://medium.com/@kanchanborade/advanced-flight-controllers-used-in-drones-a18f957f9ce7. [Accessed 6 4 2024].

[9] AspenCore, Inc., “Electronics Tutorials,” [Online]. Available: https://www.electronics-tutorials.ws/electromagnetism/electromagnetic-induction.html. [Accessed 23 04 2024].

[10] P. N. V. S. S. S. N. &. S. J. K. Rajeevalochanam, “Comparative Study of Two and Three Blade Mini Propellers Aerodynamic Performance.,” [Online]. Available: https://doi.org/10.1115/GT2016-56174. [Accessed 24 04 2024].

[11] Dan-Tech Energy, “LinkedIn,” 22 11 2023. [Online]. Available: https://www.linkedin.com/pulse/5-benefits-lithium-ion-batteries-over-lithium-polymer-lpkec/. [Accessed 25 04 25].

[12] SparkFun Electronics, “sparkfun,” [Online]. Available: https://www.sparkfun.com/servos. [Accessed 16 06 2024].

[13] TBS, “Team Black Sheep,” [Online]. Available: https://www.team-blacksheep.com/products/prod:crossfire_tx. [Accessed 17 06 2024].

[14] MATEK SYSTEMS, “GNSS & COMPASS M10-5883,” [Online]. Available: https://www.mateksys.com/?portfolio=m10-5883. [Accessed 17 06 2024].

[15] Parrot, “Parrot Sequoia,” [Online]. Available: https://www.parrot.com/assets/s3fs-public/2021-09/sequoia-userguide-en-fr-es-de-it-pt-ar-zn-zh-jp-ko_0.pdf. [Accessed 17 06 2024].

[16] AeroVironment, Inc, “Usar Manual,” 2020. [Online]. Available: https://avdss.com/help/Content/Resources/Multimedia/87732_10-Quantix-Manual.pdf. [Accessed 17 06 2024].

[17] Wingtra AG, “Wingtra,” [Online]. Available: https://wingtra.com/mapping-drone-wingtraone/technical-specifications/. [Accessed 17 06 2024].

[18] ATMOS UAV, “Marlyn Specification Sheet,” [Online]. Available: https://bmprenta.cl/wp-content/uploads/2019/11/Brochure-VTOL-MARLYN-ATMOS-UAV-BMP-RENTA.pdf. [Accessed 18 06 2024].

[19] Parrot, “Parrot Sequoia: User guide,” 05 2017. [Online]. Available: https://www.parrot.com/assets/s3fs-public/2021-09/sequoia-userguide-en-fr-es-de-it-pt-ar-zn-zh-jp-ko_1.pdf. [Accessed 03 02 2024].

[20] EASA, “EASA PRO,” 25 04 2024. [Online]. Available: https://www.easa.europa.eu/en/document-library/easy-access-rules/easy-access-rules-unmanned-aircraft-systems-regulations-eu. [Accessed 25 04 2024].

[21] M. Walker, “Aircam,” [Online]. Available: https://aircamdrone.co.uk/optimising-overlap-in-drone-mapping-a-comprehensive-guide-for-operators-and-surveyors/. [Accessed 02 06 2024].

[22] M. Hepperle, “MH-Aerotools,” 21 05 2018. [Online]. Available: https://www.mh-aerotools.de/airfoils/nf_1.htm. [Accessed 01 05 2024].

[23] M. Hepperle, “Basic Design of Flying Wing Models,” 18 05 2018. [Online]. Available: https://www.mh-aerotools.de/airfoils/flywing1.htm. [Accessed 11 05 2024].

[24] D. P. Raymer, Aircraft Design: A Conceptual Approach, California: American Institute of Aeronautics and Astronautics, 2018.

[25] XFLR5, “XFLR5,” 16 04 2024. [Online]. Available: https://www.xflr5.tech/xflr5.htm. [Accessed 23 02 2024].

[26] J. F. D. M. M. A. a. A. M. A. Yousef Gharbia, “MDPI,” 29 12 2023. [Online]. Available: https://www.mdpi.com/2226-4310/11/1/36. [Accessed 15 03 2024].

[27] Solution for All Markus Müller, “eCalc,” 18 01 2024. [Online]. Available: https://www.ecalc.ch/perfcalc.php. [Accessed 15 06 2024].

[28] ArduPilot, “ArduPilot,” 2024. [Online]. Available: https://ardupilot.org/. [Accessed

] 13 05 2024].

[29] European Space Agency, “SENTINEL-2 MISSION GUIDE,” [Online]. Available: https://sentinels.copernicus.eu/web/sentinel/missions/sentinel-2. [Accessed 21 03 2024].

[30] Dejan, “HowToMechatronics.com,” [Online]. Available: https://howtomechatronics.com/how-it-works/how-brushless-motor-and-esc-work/#:~:text=An%20ESC%20or%20an%20Electronic,of%20the%20motor%20will%20be.. [Accessed 23 04 2024].

[31] D. P. Raymer, Aircraft Design: A Conceptual Approach, California: American Institute of Aeronautics and Astronautics (AIAA), 1992.

Chapter 10. Budget

Item	Manufacturer & model	Quantity	Price per u. [€]	Total [€]
3D Filament	colorFabb LW-PLA 1.75 mm Natural	2	32.05	64.10
FC + PDB	Matek Systems F405-VTOL FC	1	63.75	63.75
Brushless motor	SUNNYSKY X2216-7 1250KV	2	22.17	44.34
ESC	Hobbywing Skywalker 40A V2	2	12.01	24.02
Propeller	8060 H461-H469	10	0.529	5.29
Battery	BRUTEPOWER 4000 mAh 4s1p Li-Po	1	51.00	51.00
Servo	MG90S 9 grams	2	1.985	3.97
Transmitter	FrSky X9D+ SE 2019 ACCESS (EU)	1	269.00	269.00
Receiver + antenna	TBS Crossfire Nano SE + Inmortal-T V2 antenna	1	30.40	30.40
TX module + antenna	TBS Crossfire TX + TBS diamond antenna	1	241.90	241.90
GPS	MATEKSYS GPS module M10Q-5883, GNSS and Compass	1	32.21	32.21
Multispectral camera	Parrot Sequoia +	1	3,200.00	3,200.00
Others	Push rod, link plug, carbon fibre tube, cable extenders	-	15.00	15.00
				4,045.59